Extreme ultraviolet probing of laser ablation

by

Lauren M.R. Hobbs

A thesis submitted for the
degree of Doctor of Philosophy

University of York
Department of Physics

March 2011

Abstract

This thesis details the use of extreme ultraviolet (EUV) sources in probing laser ablation and material opacity.

The radiation hydrodynamic codes POLLUX and h2d are used to study the Rayleigh-Taylor instability in a regime relevant to inertial fusion energy and, in support of experimental effort, to test the feasibility of methods for measurement of iron opacity. Simulations of EUV radiography using the POLLUX code show how the presence of warm, dense material leads to strong absorption of the probe beam. Methods using both broad and narrowband EUV wavelength probes for benchmarking theoretical models of opacity are presented. An iron opacity experiment conducted at the Bhabha Atomic Research Centre is modelled, where K_α emission from an aluminium layer is used to probe an iron layer beneath. H2d simulations of laser heated iron, conducted to determine the suitability of experimental results obtained at the Rutherford Appleton Laboratory for iron opacity, show the difficulty in preventing large temperature and density gradients from forming.

Interferometry has been used to measure both transmission and phase information for a 21.2 nm zinc EUV laser beam probing longitudinally through laser ablated CH plastic at the Prague Asterix Laser System. By conducting interferometric probing with EUV laser light, the region of warm dense matter between the critical surface and ablation surface in a laser ablated plasma is diagnosed. Analysis of phase shifts reveals refractive indices below solid and plasma values arising in CH

plastic, due to bound-free absorption in C^+, a model for which is presented. The transmission of the EUV probe beam provides a measure of the rate of ablation, matching previous experimental scaling laws.

Contents

List of Figures

List of Tables

Acknowledgements

I would like to thank my supervisor Professor Greg Tallents for the opportunity to carry out this work and his continued patience and support over the years.

I thank EPSRC for the Next generation application of EUV lasers grant that enabled my studies.

I gratefully acknowledge the contribution of past and present members of the laser-plasma physics group at the University of York, namely Dr J. Pasley, Prof. G. Pert, Dr N. Woolsey, Dr E. Wagenaars, Dr D. Whittaker, Dr N. Booth, Dr I. Al'miev, Dr M. Edwards, Mr A. Rossall, Mr I. Bush, Miss L. Wilson and Miss S. Safraz. I also wish to thank the staff of the PALS facility and the CLF for all their hard work during the experiments I have attended.

I wish to thank Prof. S. Rose and Mr J. Gaffney, at Imperial College London, for provision of opacity data and related advice. I am most grateful for the support from Dr R. Trines relating to the use of a simulation code. Finally I wish to thank M. Kalal for assistance in the studies of interferometry.

Declaration of Authorship

I declare that the work presented in this thesis, except where otherwise stated, is based on my own research and has not been submitted previously for a degree at this or any other university.

Parts of the work presented in this thesis have been published in some of the papers listed in appendix C.

Lauren M. R. Hobbs

To my husband David and to my father Michael; out and proud 31.08.49 - 12.02.09

Chapter 1

Introduction to extreme ultraviolet (EUV) probing

This thesis details work on the use of extreme ultraviolet (EUV) sources in probing laser-produced plasmas. Radiation at x-ray to EUV wavelengths can be used to study high-density, high-temperature plasmas that are inaccessible to visible wavelength probing, because of refraction and free electron absorption [1]. Point and extended sources have been created at x-ray and EUV wavelengths using laser-plasmas, allowing probing of dense targets with high spatial resolution imaging [2, 3]. More recently EUV lasers have provided extended, coherent sources suitable for interferometry [4] and imaging of dense plasmas [5]. It will be shown in this thesis that the short wavelength and short pulse durations that can be achieved

with EUV lasers, allows characterisation of the high-electron-density, expanding plasmas produced by laser irradiation of solid targets.

In this chapter, the principles and methods of EUV backlighting developed over the past three decades are reviewed with an emphasis on the use of broadband sources and laser-plasma based EUV lasers for this work.

1.1 Traditional EUV and x-ray backlighters

1.1.1 EUV and x-ray sources

Early x-ray and EUV point sources were created by focussing a high power laser into a cylindrical or spot focus on targets such as carbon [6], gold [2] and samarium fibres [7], resulting in emission along the axis of the fibre. Inclusion of dispersing optics into the experimental arrangement, such as a Bragg crystal (commonly PET) [2, 7], allowed spectrally resolved measurements to be made. Equally, an aperiodically ruled grating, as used in this project, can provide spectral resolution. Absorption measurements over a range of wavelengths, enabled frequency-resolved plasma opacities to be experimentally recorded [7, 8, 9, 10]. The arrangement for a point source backlighting experiment is shown in figure 1.1. Spatial information is obtained from the projection of the source through the target and onto the crystal and recording device.

The development of EUV wavelength backlighting experiments has been achieved, in part, due to the manufacture of high quality EUV optics, the properties of which

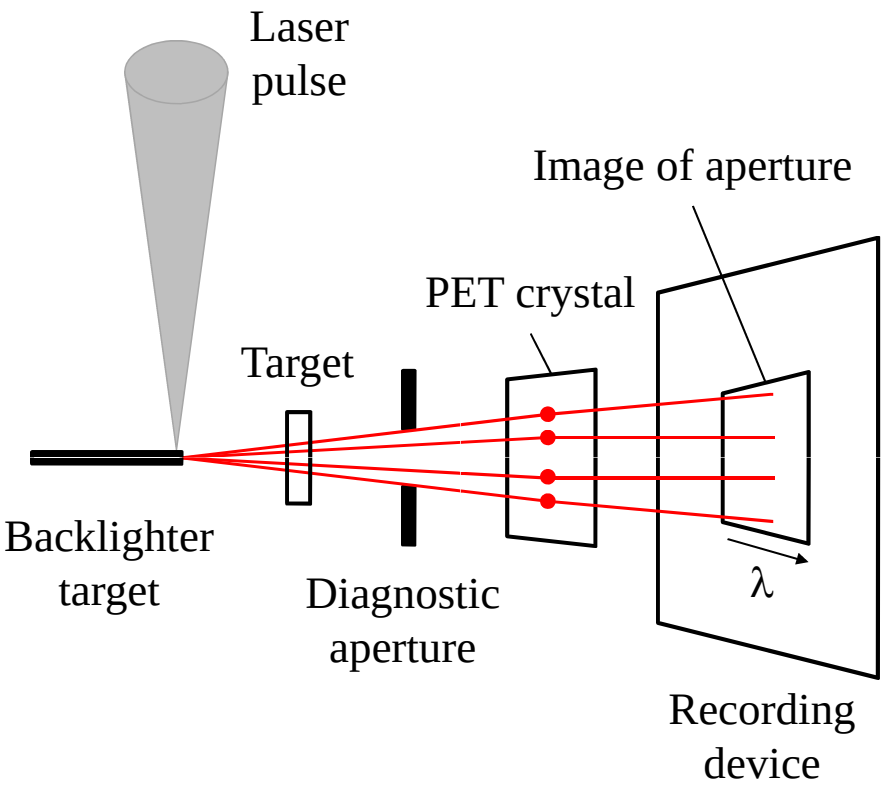

FIGURE 1.1: Experimental arrangement for point projection spectroscopy using EUV emission from a fibre target as the backlighting source. Adapted from [7].

are exploited in this thesis. Subsequent progress in the technology of multilayer optics, for use at EUV wavelengths, led to novel arrangements in backlighter experiments with spatial resolution enhancements to submicron levels made possible due to magnification by spherical mirrors [3]. The use of multilayer optics had the added advantage of filtering out radiation outside of a narrow band [3].

Transmission measurements from an extended EUV source are simulated in this work. Originally, extended x-ray and EUV sources were created by laser irradiation of planar targets [11, 12, 13]. However, these were surpassed by the use of

cavities, or hohlraums, for generating extended backlighters, enabling more uniform backlighting, both spatially and spectrally [14, 15]. Infrared or visible laser light is passed into one end of the hohlraum, typically gold cylinders of mm length, and absorbed by the walls which then emit EUV or x-ray photons. Absorption and reemission occurs within the hohlraum with a proportion of the radiation escaping for use as a backlighting source [16].

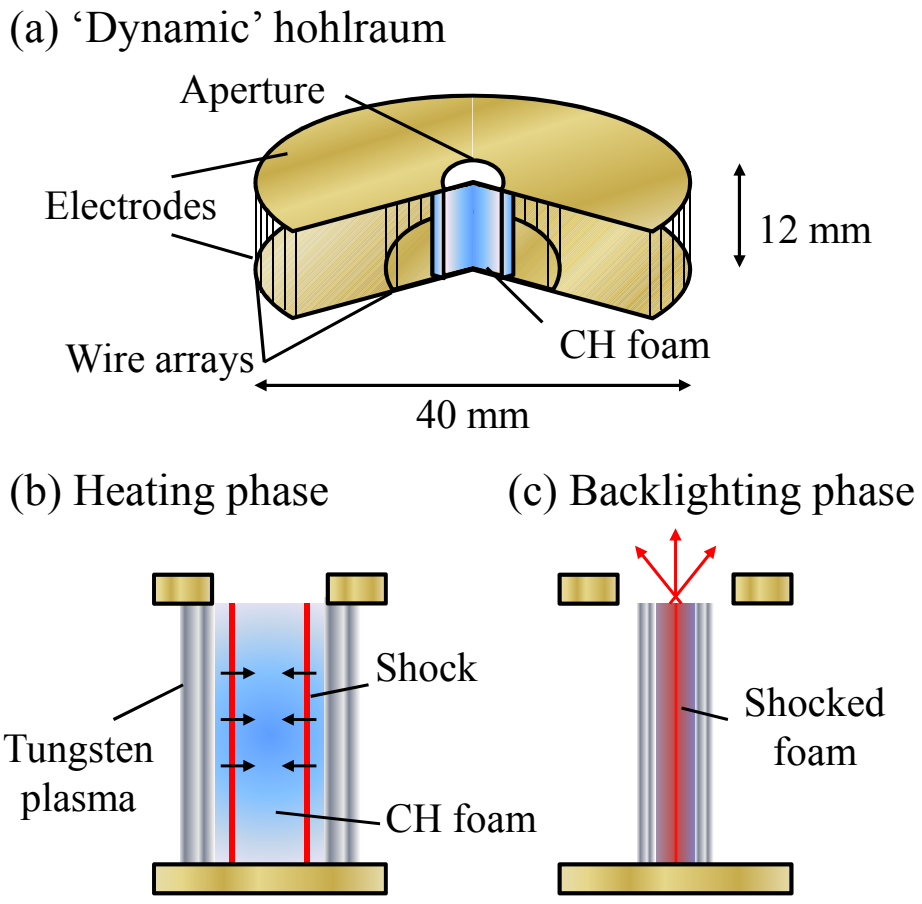

FIGURE 1.2: (a) 'Dynamic' hohlraum design based on a z-pinch. Voltage is applied across the top and bottom electrodes, causing a current to flow through the wire arrays, commonly made of tungsten. The magnetic pressure forms a z-pinch implosion, accelerating the wire plasma onto the CH foam, (b), and producing a bright backlighting source, (c), from the aperture. Adapted from [14, 15].

'Dynamic' hohlraums, developed at the Sandia National Laboratory [17], use an

annular array of high-Z wires which through application of large current form z-pinch implosions. The design and concept is illustrated in figure 1.2. The plasma, accelerating inwards, stagnates on an inner cylinder of low-density CH foam, launching a radiating shock towards the centre of the cylinder. The radiation is then contained by the outer, cooler regions of the high-Z imploding plasma [15, 17]. The imploding plasma effectively becomes the radiation container itself, thereby allowing for smaller cavities and increased containment [17]. Studies at the Sandia National Laboratory and Imperial College MAGPIE facility have found that the power of the emitted EUV or x-ray radiation can be optimised by changing the radius of the array and initial wire separation [17, 18].

1.1.2 X-ray and EUV backlighters for measuring iron opacity

Many experiments over the last two decades have sought to experimentally determine iron opacity [7, 8, 9, 10, 19, 20, 21]. The motivations behind iron opacity studies, as well as a comparison between theoretical opacity models, are outlined in section 2.2.

X-ray absorption spectroscopy has previously been carried out to study iron targets, tamped by CH plastic in order to maintain uniformity during heating [9, 10, 21]. An experiment by Winhart et al. [21] used a planar gold target backlighter to measure spectrally resolved opacities of iron in the 4 - 17 nm wavelength range.

The plasma was kept below 22 eV to prevent significant target self emission which would have overwhelmed the backlighter emission [10, 21].

It is possible to use target self emission as backlighting radiation, by irradiating multi-layer targets. Emission from the top-layer material, if well-characterised, can be used to probe the buried layer material. The simulation code h2d [22], described in section 4.2, has been used in conjunction with an experiment to study x-ray backlighting of a buried iron layer using the emission from an aluminium top-layer as the probe (see section 5.2).

The use of hohlraums in x-ray generation from the mid 1990s produced bright probes for opacity targets [16, 17]. For example, an experiment by Bailey et al. [15] used a 'dynamic' hohlraum to determine iron transmissions over the photon energy range 800 - 1800 eV (1.54 - 0.69 nm) with a spectral resolution $\nu/\Delta\nu \sim$ 700 [15] suitable for measuring broadband features. Conversly, EUV lasers provide monochromatic sources to probe at discrete wavelengths, allowing specific absorption features to be investigated. A narrow spectral bandwidth with $\nu/\Delta\nu \sim 50000$ as obtained [1].

1.1.3 High-order harmonics

Coherent beams of EUV and x-ray radiation can be produced through high-order harmonic generation from gas or solid targets [23, 24, 25, 26, 27, 28]. The oscillating electric field of an optical laser pulse accelerates electrons, tunnel-ionising them from their parent atoms, so that they oscillate, radiating electromagnetic

waves. Departures from sinusoidal electron oscillation induces higher harmonic Fourier components in the radiated electromagnetic radiation. In solid targets the electric field of a laser pulse can induce relativistic oscillations of electrons near the vacuum-target boundary. The laser pulse couples to the target surface, causing the electrons to oscillate in phase [24, 25]. Harmonics have been produced from laser interaction with gas jets, although at lower conversion efficiencies due to destructive interference along the path of the harmonics through the extended media [26, 27].

In gas targets, as the order increases the harmonics are produced with approximately equal efficiency up to the maximum harmonic photon energy $h\nu_{\max}$, determined by the atom ionisation energy E_{Z^*} plus 3.17 times the electron ponderomotive energy such that

$$h\nu_{\max} = E_{Z^*} + \left(3.17 \times 10^{-13} \frac{\text{eV}}{\text{W cm}^{-2}\ \mu\text{m}^2}\right) I\lambda^2 \tag{1.1}$$

where I is the optical laser intensity (in W cm^{-2}) and λ the wavelength (in microns) [29]. High harmonics have been proposed for use as backlighters for measuring iron opacity at multiple photon energies, encompassing a broad spectral range within a single laser shot [30].

1.2 EUV wavelengths lasers

1.2.1 Principles of lasing at EUV wavelengths with plasma based lasers

EUV lasers emit intense, coherent radiation in the region of 5 - 125 nm. Unlike in conventional lasing at optical wavelengths, a cavity is not included for amplification due to poor reflectivity at EUV wavelengths and, in particular, the difficulty of manufacturing an output mirror. It has, therefore, been necessary to achieve amplification during a single pass through the gain medium [31]. This is realised through amplified spontaneous emission (ASE), where a spontaneously emitted photon may give rise to stimulated emission from another excited atom [32]. For EUV lasing, excitation of ground state electrons to sufficiently energetic upper levels must occur. By heating materials to produce highly ionised ions, higher energy quantum states are produced, with specific levels being capable of EUV lasing at photon energies 10 - 250 eV [31]. The gain material consequently exists in a plasma state. In this work zinc has been used to produce lasing at wavelength 21.2 nm.

To produce lasing, a large population of excited quantum states must be available [1]. Also the material must be sufficiently ionised to have energy level separations in the EUV region ($\sim$ 5 - 125 nm). As the gain medium is heated and the plasma forms, one can expect a large fractional abundance of neon-like and nickel-like ions, having closed shells of principle quantum number $n = 2$ and $n = 3$ respectively. This will occur granted a sufficiently high atomic number, such as in zinc,

and temperatures in the range 100 eV - 1 keV. Figure 1.3 shows the energy level diagrams and lasing transitions for each species. Taking the silver EUV laser as

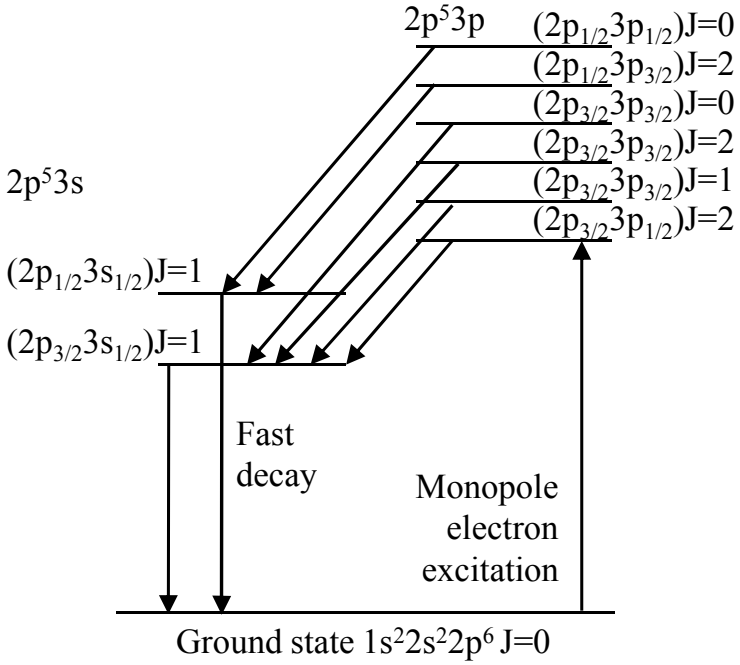

(a) Neon-like

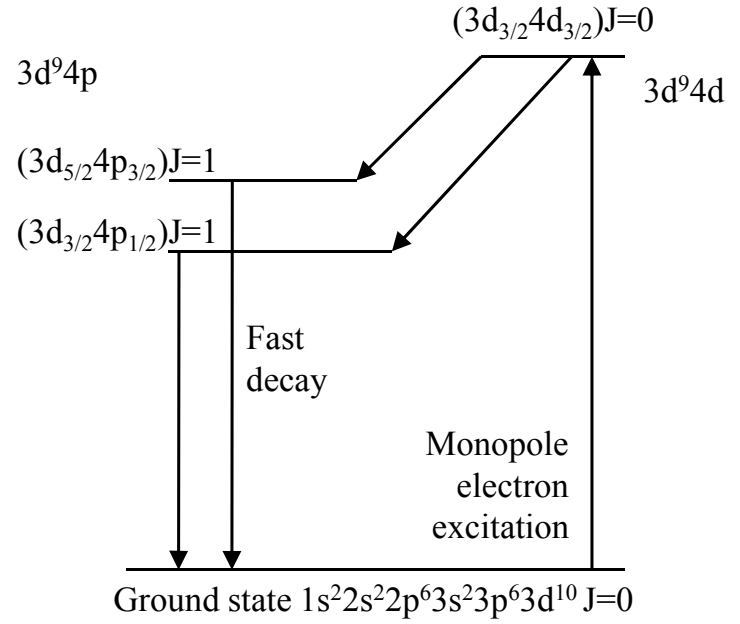

(b) Nickel-like

FIGURE 1.3: Energy level diagrams for neon-like (a) and nickel-like (b) species. Lasing occurs between excited sub-shells $2p^53p - 2p^53s$ (neon-like) or $3d^94d - 3d^94p$ (nickel-like) [1].

an example, the characteristic lasing line is at 13.9 nm and arises from a $4d - 4p$ transition, in nickel-like silver. As the ground state to $4d$ transition is electric dipole forbidden, excitation from the ground can only occur by monopole excitation, involving free electrons in the plasma. This also results in lower decay rates back to the ground state, facilitating population inversion [33]. Once in the $4d$ state, decay can occur to the $4p_{1/2}$ or $4p_{3/2}$ levels, with EUV emission, followed by fast decay to the ground state.

It was a combination of a lens and off-axis mirror producing a line focus on the centimeter scale in length and micron scale in width that led to the first EUV lasers [34]. The original EUV lasers used slab targets, where a single heating beam passed to a spherical mirror, creating a line focus [35, 36]. It was later discovered that by using a prepulse to create a preplasma, into which the main optical pumping pulse is incident, the refraction of the EUV laser beam out of the sample is reduced and absorption by inverse bremsstrahlung is improved [1, 37, 38]. Ionisation is a relatively slow process, making it advantageous to prepare the plasma to near the required nickel-like or neon-like ionisation before the main pulse is incident [39]. Taking again the example of silver, an optical pumping pulse first heats the sample, forming a plasma with nickel-like ions with a $n = 3$ closed shell remaining. The preplasma is then illuminated by a second, higher intensity pulse which excites an electron from the $n = 3$ closed shell to an upper excited level. The duration of the second pulse determines the duration of the EUV pulse, though very short (sub-picosecond) pulses are not possible because of the natural spectral bandwidth of the lasing output [1].

The intensity of the prepulse and main pulse, together with the timing delay between them, must be optimised to produce the best output. Shorter laser pulses (ps scale) incident onto a preformed plasma have been shown to reduce refraction, increase the volume of plasma exhibiting gain and enhance laser absorption [1]. A high-density plasma is required for high gain. However, too high a density can lead to a reduced population inversion through collisional mixing, enhanced line broadening and increased opacity, all of which reduce the gain [31].

As discussed, before application of the main optical pumping pulse for EUV laser action it is advantageous to form a preplasma at the sample surface. By having a solid slab or stripe target, multiple shots, of focal widths ≈ 100 μm typical [1], can be taken without requiring sample replacement.

For picosecond scale pumping the gain duration is short and it becomes advantageous to move the pumping excitation along the gain medium, in the desired direction of output. Only a localised region is pumped to inversion, which then moves along the line focus length in time with the amplifying EUV beam. By insertion of a diffraction grating to tilt the laser energy pulse front, a travelling wave is induced across the main pulse with a shear delay over the beam (see figure 1.4), thereby achieving directionality to the EUV laser [31].

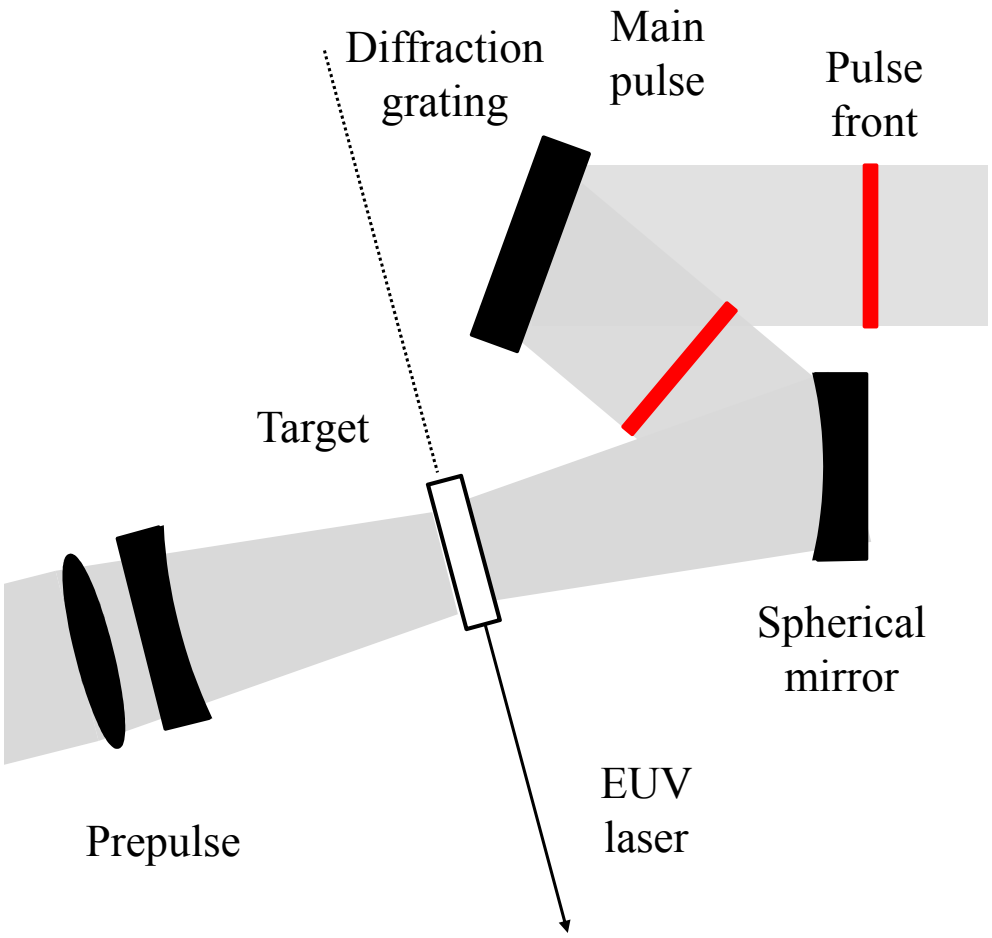

FIGURE 1.4: Scheme for EUV laser production using a diffraction grating to change the orientation of the pulse front, thereby creating a travelling wave along the line focus at the target. Adapted from [1].

An alternative method, of GRazing Incidence Pumping (GRIP), involves the application of the short duration (ps scale) main pulse at a grazing angle to the sample surface in a line focus (see figure 1.5). The beam is refracted into the plasma formed by the prepulse, leading to absorption. The required angle of incidence for this to occur can be calculated from a simplification of the refraction equation with

$$\theta = \sqrt{\frac{N_{e,max}}{N_{crit}}} \tag{1.2}$$

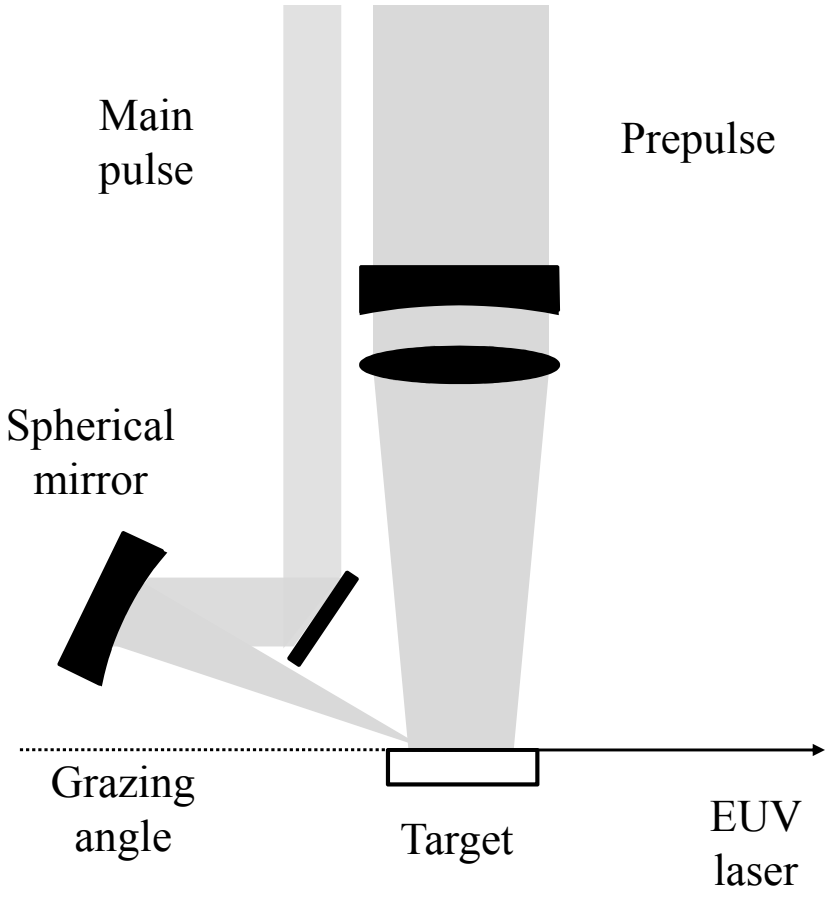

FIGURE 1.5: Scheme for GRIP showing main pulse and prepulse geometry for EUV laser production. Adapted from [40, 41]

given by $N_{e,max}$, the maximum electron density and N_{crit}, the critical electron density [41]. This method allows for an increased path length of the heating beam through the plasma, thereby increasing the opportunity for absorption and reducing the incident energy required for saturated lasing [42]. Experiments have shown the peak in EUV laser output energy occurring for prepulse to main pulse delays between 400 and 700 ps, with a dependence on grazing angle being noted [40, 42].

To achieve the high-intensity optical main pulse chirped pulse amplification (CPA) is used. CPA takes a high-power pulse and then stretches it in time. This reduces

the power to below the damage threshold for subsequent amplifiers. Once passed through the amplifying media the pulse is then compressed to a duration approximately equal to the original duration, but now with a higher peak power [43]. By such methods laser pulses required to produce short duration EUV lasers can be created.

A variety of materials have been shown to effectively lase at EUV wavelengths (see table 1.1). For nickel-like ions the ratio of laser photon energy to the energy of the upper lasing level, known as the quantum efficiency, is higher. Therefore nickel-like ions dominate the shorter wavelength EUV lasers [1].

TABLE 1.1: Common elements of atomic number Z for EUV laser production, together with the lasing wavelength and the responsible transition [42].

Element	**Symbol**	**Z**	**Lasing wavelength**	**Transition**
Germanium	Ge	32	23.21 nm or 23.6 nm	3p-3s in Ne-like Ge
Zinc	Zn	30	21.2 nm	3p-3s in Ne-like Zn
Molybdenum	Mo	42	18.9 nm	4d-4p in Ni-like Mo
Silver	Ag	47	13.9 nm	4d-4p in Ni-like Ag
Tin	Sn	50	12 nm	4d-4p in Ni-like Sn
Samarium	Sm	62	7.3nm	4d-4p in Ni-like Sm

The zinc EUV laser used in this work was created using the Prague Asterix Laser System (PALS) and the method depicted in figure 1.4. A separate prepulse and main pulse illuminate a solid zinc target, producing a narrowly collimated beam of

21.2 nm photons from the $(2p^5_{1/2}3p_{1/2})_{J=0} \rightarrow (2p^5_{1/2}3s_{1/2})_{J=1}$ transition in neon-like zinc [44].

1.2.2 Using EUV lasers as backlighters

Lasing at EUV wavelengths was first demonstrated at the Lawrence Livermore National Laboratory (LLNL) in the mid 1980s by Matthews et al. [33]. Optical laser illumination of thin foils of selenium at intensities of 5×10^{13} W cm^{-2}, was observed to produce a directed beam of 21 nm photons. Earlier attempts to produce an intense EUV source had been hampered by difficulty in producing the uniform long line focus required for high gain [34]. Yttrium foil targets were then employed, producing 15.5 nm photons and confirming the method for production of a bright EUV source [33].

In the early 1990s an experiment conducted by Carillon et al. [36], at the Central Laser Facility (CLF), Rutherford Appleton Laboratory (RAL) demonstrated a saturated EUV laser with an approximate brightness of 10^{14} W cm^{-2} sr^{-1} [36] at 23.6 nm from a germanium plasma. EUV lasers were soon applied to study high-density, high-temperature plasmas that are inaccessible to optical probing.

A key application has been the use of EUV lasers in imaging plasmas. In the mid to late 1990s side-on (transverse) and face-on (longitudinal) plasma imaging was conducted to study numerous sample targets. An experiment carried out by Cauble et al. [45], used laser heating and probing at EUV wavelengths to study laser-acceleration of metal foils. By creating a high-brightness EUV laser they

were able to overcome the emission of the target and obtain few-micron resolution images. They cited the advantages of EUV lasers over traditional backlighters as being the small bandwidth and short pulse duration achievable [45].

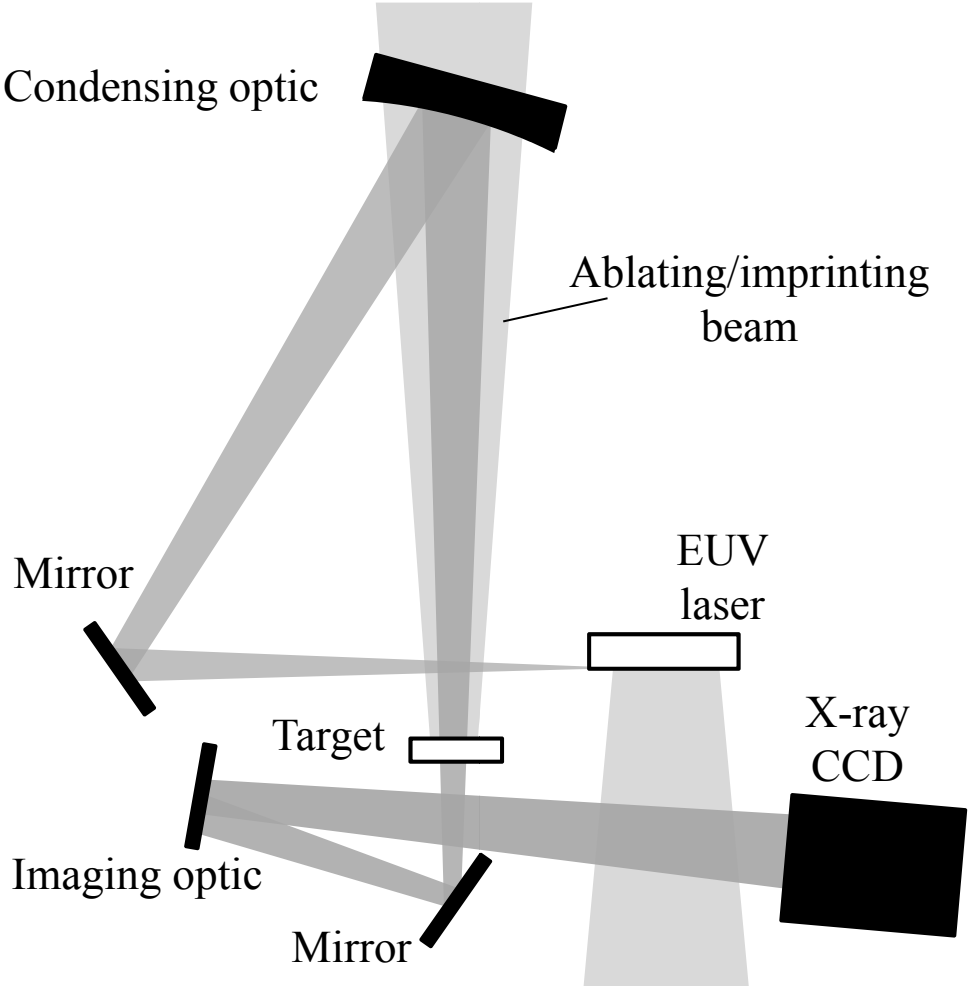

FIGURE 1.6: Typical experimental arrangement for conducting EUV laser backlighting of foil targets. Indicated are the multilayer optics, capable of imaging the EUV wavelength beams. Adapted from [46].

Experiments by Key et al. [5] and Kalantar et al. [46, 47] have used EUV lasers to measure the imprint of early-time non-uniformities in irradiating lasers and the resulting instability formation, extensions to which are carried out in this work. A typical experimental arrangement for these studies is shown in figure 1.6. Varying laser patterns and target modulations have been applied to seed

instabilities and discover their effect on target break-up. EUV lasers have allowed probing of silicon and aluminium targets. However, limited knowledge of opacity of these materials, which will change during shock compression, hampered early experiments [5, 46, 47, 48]. For this project the 2D simulation code POLLUX [49], described in chapter 4, has been used to provide a more rigorous approach to the study of the Rayleigh-Taylor Instability (RTI), the results of which are presented in section 5.1.

As part of the work of this thesis an EUV laser has been used to probe laser ablation and in doing so demonstrate a novel diagnostic technique (chapter 3). This builds upon a study by Edwards et al. [50] in 2007, where temporally resolved measurements of laser ablation were made, using the transmission of an EUV laser through a heated iron target.

An established method of determining the rate of laser ablation is to construct a target of the sample material with buried layers, intended to produce signature emission when the ablation front has reached the layer depth [51, 52]. Multiple layer depths are constructed and tested to find the ablation rate at different times, with the onset of emission from the buried layer signalling ablation [51]. However, for higher intensity laser experiments, the production of hot electrons can lead to preheating of the buried layer, potentially inducing emission ahead of the ablation front [53]. In addition to this, the emission from the buried layer can often be overwhelmed by emission from lower density, hotter material that forms the expanding plasma. The EUV probing experiments of this project have been constructed to limit detection of target self emission. By probing the sample material

itself, rather than detecting buried layer signals, hot electron preheat becomes a measurable quantity rather than a limitation.

Mass ablation rates *can* be characterised via particle detection methods, where arrays of ion Faraday cups and calorimeters are used to measure the mass of the ion flow, which is then summed. However, this produces time averaged measurements and places caveats on target design in order to avoid errors in two dimensional angular integration of the signal [54, 55].

The use of EUV wavelength probes enables measurements to be taken that are unaffected by collective processes in the plasma, e.g. interaction with self-generated electric and magnetic fields, plasma oscillations. For example, the critical density N_{crit} for the Zn 21.2 nm EUV laser (considered in chapter 6) is 2.5×10^{24} cm^{-3}, while the electron density N_e of an ionised CH plastic target at solid density is an order of magnitude smaller (up to 2.5×10^{23} cm^{-3}[56] assuming complete ionisation). Plasmas at this density are inaccessible to an optical probe, due to the much lower critical density [57].

Probing constraints

The approximate densities N_e and material lengths L accessible to probing with the Zn 21.2 nm EUV laser can be estimated by considering constraints based on the degree of absorption of the probe beam. Taking the limiting case of complete ionisation, only free electrons in the plasma contribute to the absorption coefficient κ [4, 32]. For example, considering a fully ionised CH plasma; $Z^* = 7$ at electron

temperature $T_e \sim 250$ eV (see section 4.2 for details of the ionisation model used in this work).

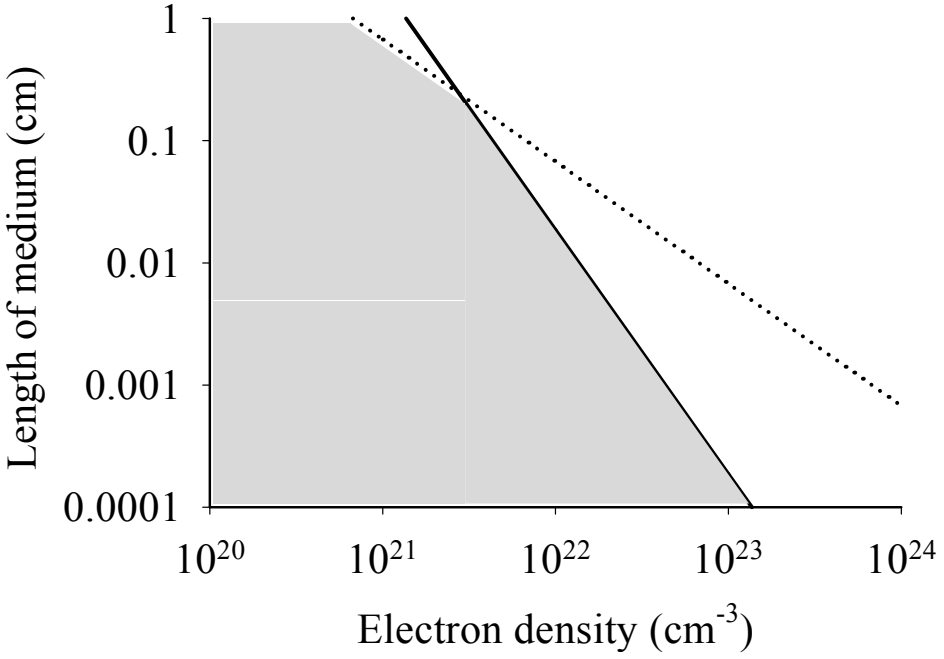

FIGURE 1.7: Limits of electron density and length of plasma accessible for a Zn 21.2 nm EUV laser probing a fully ionised CH plasma (at 250 eV). The solid line represents the boundary due to absorption within the plasma (assuming free-electron absorption dominates and a maximum optical depth of unity). Also shown are the limits for practicable detection of interferogram fringes (dotted line) based on a 2048 pixel width CCD detector. Adapted for parameters relevant to this work from [4, 32].

From a simple model of free electron absorption [58] the absorption coefficient for laser absorption at frequency ω is given by

$$\kappa_{\text{free}} = 8.5 \times 10^8 \frac{Z^* N_e^2}{T_e^{1/2} \omega^3} = 5.4 \times 10^{-43} N_e^2 \text{ cm}^{-1}. \tag{1.3}$$

Allowing for one optical depth of absorption (i.e. $\kappa L = 1$), N_e and L must satisfy the condition [4, 32]

$$N_e^2 L \leq 1/(5.4 \times 10^{-43}). \tag{1.4}$$

The shaded area of figure 1.7 shows the accessible parameter space, based on this condition. In reality contributions from bound electrons will lead to higher absorption, therefore this approximation gives an estimate of the maximum possible density-length product $N_e L$ that can be probed.

In 1995 Da Silva et al. [4], used a yttrium EUV laser to carry out interferometry of expanding CH plastic plasmas. A set of beam splitters and a Mach Zehnder interferometer were employed to probe plasma plumes of densities up to 10^{21} cm^{-3} [4]. Smith et al. [59], carried out EUV interferometry with picosecond time resolution to image expanding plasmas of density 3×10^{20} cm^{-3} with minimal motion blurring. The experimental arrangement for EUV interferometry in these experiments is shown in figure 1.8. In chapter 6 the use of a wavefront splitting interferometer is demonstrated to allow longitudinal probing of plasmas (in approximately the same direction as optical heating) of densities two orders of magnitude higher than achieved here.

For successful interferometry at EUV wavelengths, the fringe spacing must be considered. Superimposed on figure 1.7 is the boundary assuming a minimum 16 pixel fringe spacing for practicable measurements across a 2048 pixel width CCD detector (common to the work carried out for this thesis). The number of fringe shifts n_{fringe} detected when carrying out interferometric probing on, for example,

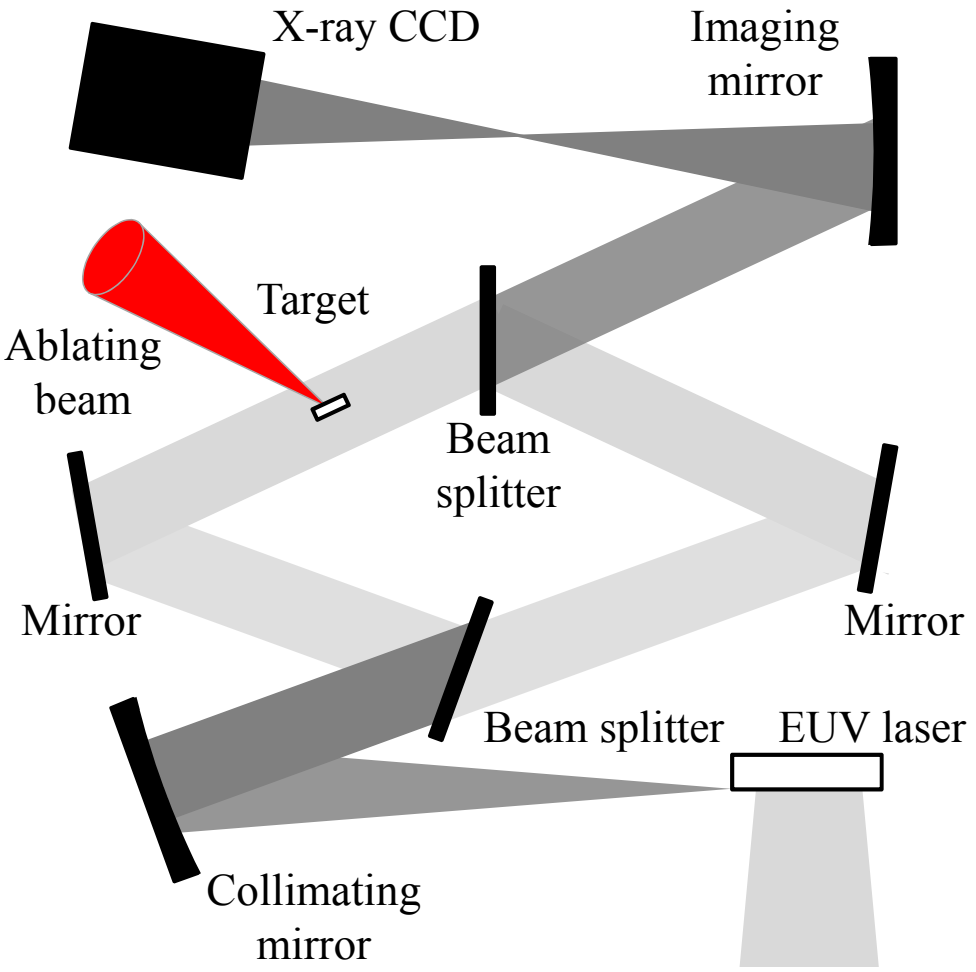

FIGURE 1.8: Experimental arrangement for conducting EUV interferometry of a target plasma. Use of a Mach-Zehnder interferometer is shown, in a skewed geometry to avoid the polarising propeties of the multilayer mirrors when operating at 45°. Adapted from [4].

a uniform plasma relative to vacuum is given by

$$n_{\text{fringe}} = \frac{1}{\lambda}\int_0^L (\eta_{\text{plasma}} - 1)dz \approx \frac{N_e L}{2N_{\text{crit}}\lambda} \tag{1.5}$$

for wavelength λ in the direction of probing z and plasma refractive index $\eta_{\text{plasma}} = (1-N_e/N_{\text{crit}})^{1/2} \approx 1-N_e/(2N_{\text{crit}})$ [32]. This bounds the parameter space accessible for EUV interferometry (see shaded area on figure 1.7).

1.2.3 EUV and x-ray free electron lasers

There is a limit to the minimum pulse duration that can be achieved from EUV lasing, set by the inherent bandwidth of the lasing output. Having a broad bandwidth, free electron lasers (FELs) have been used to generate very short duration ($<$ 100 fs), high-brightness pulses of EUV and x-ray photons, with pulse energies of 1 mJ and focussed intensities of up to 10^{18} W cm^{-2} now achievable [60], with proposals for generating attosecond pulses also emerging [61].

In an FEL relativistic electrons are injected into an undulator, consisting of magnets of alternating polarity, thereby inducing sinusoidal motion of the electrons [62]. Within the FEL the electrons undergo self-organisation in a process known as microbunching. This leads to the electrons radiating coherently to produce a high-brightness pulse as electromagnetic energy is extracted from the kinetic energy of the relativistic electron beam [61, 62]. A consequence of the poor reflectivity of mirrors at EUV wavelengths, mentioned previously with respect to EUV lasers, is that amplification must occur within a single system pass. Most FELs rely on self-amplified spontaneous emission within long undulators to achieve this. The electrons are first accelerated in resonators to relativistic speeds and are then passed to an undulator where the periodic arrangement of magnets forces the electrons to adopt a sinusoidal trajectory, emitting EUV radiation along the undulator axis. The emitted photons then travel ahead of the electron bunch so that over the length of a single wavelength part of the bunch will be slowed down and part accelerated. As microbunches of electrons form, the electric fields of emitted radiation from all the electrons in a microbunch add coherently [61, 62].

The short duration pulses that can be achieved with FELs may be used to provide high temporal resolution measurements of expanding laser-plasmas and to examine the plasmas formed by the FELs themselves. Table 1.2 lists the current x-ray FELs that are operational, under construction or in the advance design stage, taken from a 2010 review by McNeil and Thompson [61]. As the access to these facilities increases EUV probing experiments discussed in this work can be repeated with reduced temporal error.

TABLE 1.2: Current x-ray FELs, taken from [61].

Facility	**Location**	**Status**	**Minimum wavelength (nm)**
LCLS	USA	Operational	0.12
FLASH	Germany	Operational	4.45
XFEL	Germany	Construction	0.1
XFEL/SPring-8	Japan	Construction	0.1
Fermi@Elettra	Italy	Construction	4
SwissFEL	Switzerland	Design	0.1
PAL XFEL	Korea	Design	0.1
LCLS-II	USA	Design	0.6
SPARX	Italy	Design	0.6
FLASH-II	Germany	Design	4

1.3 Introduction to the thesis

This chapter has introduced how backlighting radiation sources have been used to study laser ablated plasmas and material properties, with the ability to spatially and spectrally resolve being paramount. Chapter 2 details the motivations behind the study of laser ablation and introduces a theoretical model for the phase shifts measured by interferometry. Complex interferometry (see chapter 3) has allowed transmission and phase shift data to be extracted simultaneously, with the results given in chapter 6 together with those from two-dimensional simulation using the radiation hydrodynamic code h2d [22], which is described in chapter 4. A post processor has been developed to calculate transmissions from simulation code data (see section 4.3). Experimental backlighting methods for determining iron opacity and probing Rayleigh-Taylor instability are described in chapter 5

The conclusions of the work detailed in this thesis are summarised in chapter 7, together with suggested directions of future work.

Chapter 2

Background to EUV probe experiments

Within this chapter, laser ablation of solid targets and its relevance to inertial confinement fusion (ICF) is introduced, including the impact of the Rayleigh-Taylor instability (RTI). EUV probing, described in this thesis, elucidates knowledge of plasma opacity and refractive index. These quantities are introduced, together with the Kramers-Kronig relation, which links them.

2.1 Laser ablation

Laser ablation refers to the removal of material from the surface of a solid target after irradiation by high-power laser light ($> 10^9$ Wcm^{-2}) [63] as it responds to its own pressure by flowing away from the solid [64]. Ablation begins as laser energy is absorbed by bound electrons through multi-photon processes, forming a plasma. Free electrons dominate the absorption through inverse bremsstrahlung and then non-linear absorption processes, such as resonance absorption, at the critical density [65]. Energy deposited by the laser via free electron absorption is conducted through the plasma to the solid target material, leading to hydrodynamic flow and ablation. A coronal plasma expands along the target normal [66]. The rate at which mass is ablated and the ablation are therefore interrelated and will scale with laser intensity, laser wavelength and target atomic number [64]. At relatively low intensity, the energy of the accelerated electrons is transferred to the bulk plasma by electron-ion collisions [67]. A necessary condition for collisional absorption to be effective is that the electron-electron collisions keep the electron distribution function nearly Maxwellian. A widely used condition to ensure this states that

$$I\lambda^2 < 1 \tag{2.1}$$

for laser intensity I in units of 10^{14} W cm^{-2} and wavelength λ in units of μm [67]. When this value exceeds unity the laser absorption becomes less efficient and many hot electrons will be generated, preheating the target ahead of the ablation front [67].

Since the conception and demonstration of lasers in the late 1950s to early 1960s, their use in plasma creation has been explored [68, 69, 70, 71]. In the earliest experiments, laser induced emission of photons and charged particles from varying samples under focussed ruby lasers was observed [70, 71]. A key application of interest in modern laser ablation studies is to determine ablation rates relevant to direct drive ICF. This project considers laser ablation studies in relevant regimes.

2.1.1 Laser ablation and shock compression of ICF targets

In ICF, laser ablation drives the compression of fuel pellets leading to ignition and burn of DT fuel material and release of energy. Accurate modelling of laser ablation in direct drive ICF requires knowledge of how the mass ablation rates of plastic shell material relates to the heating laser conditions at relevant irradiances. Figure 2.1 depicts the stages for compression, ignition and burn in direct drive ICF. Proposed targets consist of a DT vapour encapsulated in a shell of DT ice within a thin (~ 5 μm) plastic shell [72, 73]. The aspect ratio (shell radius to thickness ratio) is in the range 10 - 100 [74].

This target is irradiated by multiple beams symmetrically, with nanosecond pulses at intensity $I\lambda^2 < 10^{14}$ W cm^{-2} μm^2, ablating the outer shell as it heats up and expands [75]. The remaining shell material is accelerated inwards, conserving momentum. Laser energy is imparted to the electrons by inverse bremsstrahlung, up to the critical density, and resonance absorption, a collisionless process, in the region of the critical density [76]. Due to momentum flux from laser driven ablation, work is done. In a strong compression the work done is the product

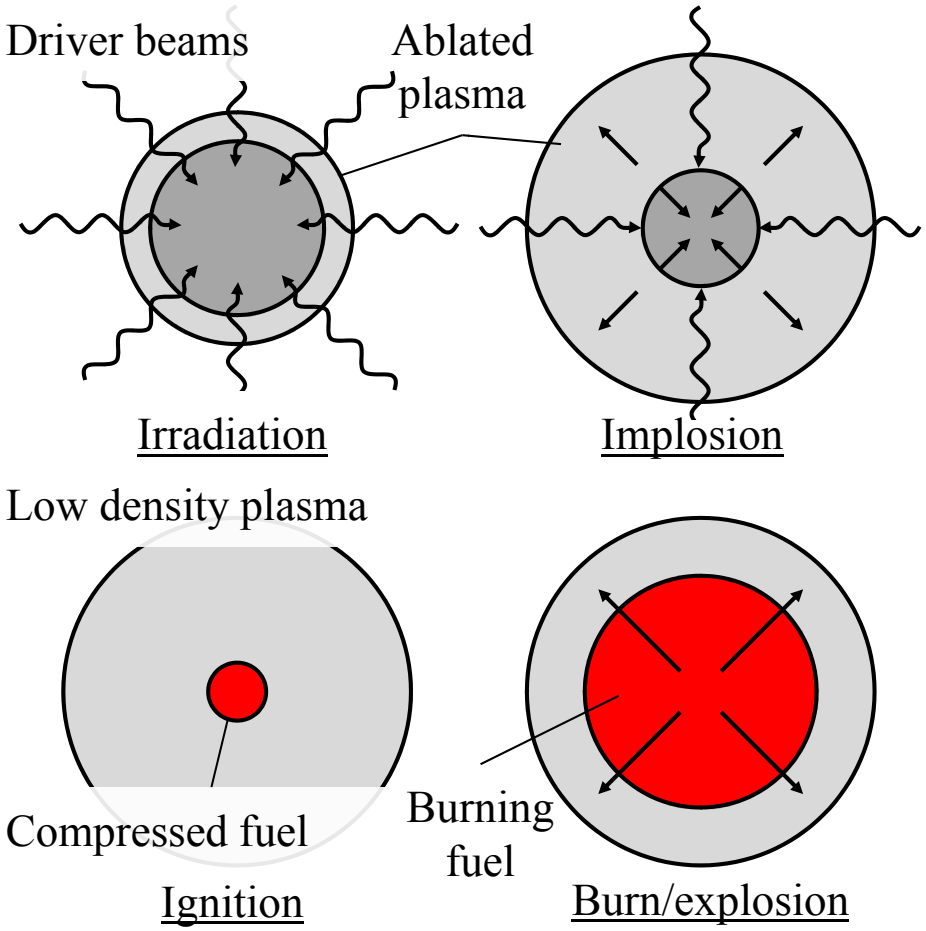

FIGURE 2.1: Scheme for direct drive ICF. Adapted from [75].

of the pressure p_a generated by the ablation process times the volume enclosed by the shell [76]. For strong compression the temperature of the compressed material must be kept low, as increases in temperature require more pressure for compression. According to the first law of thermodynamics the change in fuel energy dE within a pellet upon compression is given by $dE = T_e ds - p_a dV$, where T_e is the fuel temperature, ds is the change in entropy and dV is the change in fuel volume. The internal energy of the fuel can increase due to a transfer of heat $dE = T_e ds$, implying an entropy increase ds, or by a volume change with $dE = -p_a dV$ [74]. Isentropic compression with $ds = 0$ minimises the invested

energy. However, with, say, very fast compression a single pulse of pressure leads to a single strong shock wave, which produces large amounts of entropy [74]. Fortunately nearly isentropic compression can be achieved by superimposing a sequence of shocks. The temporal increase of the pressure creating the shock sequence has to be shaped carefully such that shocks coalesce at the same time [74].

As the fuel of an ICF target has to be imploded to high velocity at low entropy, the implosion of hollow spherical shells works much more efficiently than the implosion of a uniform solid sphere [74]. The fuel can be accelerated over larger distances and so a lower driving pressure is required to reach the required implosion velocity. The pressure required to accelerate a shell of constant mass to ablation velocity v_a scales as $p_a \propto v_a^2/A_R$ where $A_R = R_0/\Delta R_0$ is the initial aspect ratio of the shell of radius R_0 and thickness ΔR_0 [74]. Reducing the required driving pressure is useful because, as will be discussed shortly, plasma instabilities limit the pressure that can be generated by ablation [74]. Hollow spheres are easier to compress isentropically as the shocks do not undergo convergence enhancement as they pass through the thin shell. With shell compression, spherical convergence occurs more or less adiabatically [74].

The use of a thin shell is essential to allow delivery of the required energy. Neglecting mass variation due to ablation of the target, this is simply seen by equating the fuel energy density per unit mass E to the work ($p_a dV$):

$$E \approx \frac{v_a^2}{2} \propto p_a R_0^2 \frac{R_0}{\Delta R_0}. \tag{2.2}$$

The final collapse amplifies the ablation pressure [67]. Hence, for a given pressure, a larger, thinner shell that encloses more volume can be accelerated to a higher velocity than can a thicker shell of the same mass. The peak achievable implosion velocity determines the minimum energy (and mass) required for ignition of the fusion fuel in the shell [76].

Referring back to equation (2.1), the intensity if too high will lead to hot electron preheat, making the target harder to compress [74]. However, the resulting maximum achievable ablation pressure at lower intensities is too low for ICF. Hence the need for pressure amplification [67]. At first a shock with ~ 1 Mbar pressure is driven into the shell. This shock is seen to break through the inner surface of the fuel layer and at about this time the power of the tailored driving pulse is strongly increased and this causes stronger ablation and hence higher ablation pressure [67]. Subsequent shocks now lead to smooth acceleration of the whole solid shell. At peak laser intensity the ablation pressure is about 130 Mbar [67]. When the driving pulse is switched off almost 90% of the plastic layer has been ablated. The shell has now imploded to half the initial radius and is coasting inwards at velocities $\sim 3.75 \times 10^7$ cm s^{-1} [67]. The shell coalesces in the centre and comes to rest. At this time the fuel pressure reaches 250 Gbar [67]. For optimised efficiency only a small mass of fuel will be heated up to ignition temperatures ($\approx 5 - 10$keV [75]). Power is released by alpha particles, created from initial reactions, forming a hot spot and then triggering a burn wave to ignite the remainder of the fuel [51, 75, 77, 78, 79]. The colder fuel surrounding the hot spot has been compressed to ≈ 400 g cm^{-3}[74].

Compression of the DT fuel mass makes it feasible in the lab to achieve the $\rho R = 3$ g cm^{-2} needed for the desired burn efficiency of at least 1/3 [76]. For a sphere we have mass

$$m = \frac{4\pi}{3}\frac{(\rho R)^3}{\rho^2}. \tag{2.3}$$

Hence the mass (and also driver energy at fixed efficiency) required for $\rho R = 3$ g cm^{-2} scales as $1/\rho^2$. Assuming a burn fraction of 0.33, at a normal liquid density of 0.21 g cm^{-3}, more than 2.5 kg of DT would be required for ignition [76]. If this much mass were ignited it would yield about 3×10^{14} J (equivalent to 75 kTonnes of TNT explosive). But, for example, at a density of 400 g cm^{-3} a spherical shell with a thickness $R/2$ and radius R would have $\rho R = 3$ g cm^{-2} and a mass of 5 mg [76]. This mass would have a yield of about 6×10^8 J (equivalent to 0.15 Tonnes of TNT) and could be contained in the laboratory [76].

2.1.1.1 Rayleigh-Taylor instability in ICF compression

During irradiation it is important to have uniformity between the driver beams, as perturbations will be amplified in the compression process, forming instabilities such as the Rayleigh-Taylor instability (explored in this work, see section 5.1). The RTI arises when a more dense fluid is pushed by a less dense fluid (figure 2.2). Small spatial perturbations on the surface between the fluids grow exponentially in size. RTI growth can occur under gravity and, equivalently, from acceleration of a lighter fluid into a denser fluid, as in laser ablation [80].

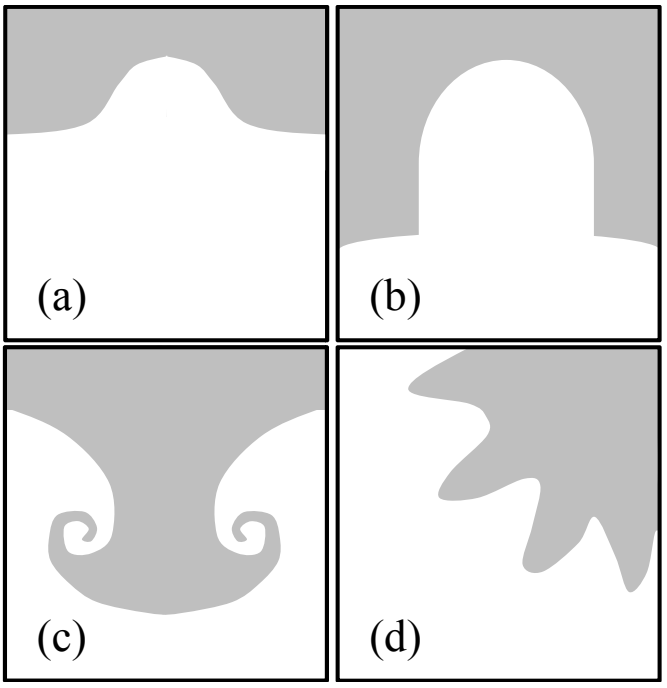

FIGURE 2.2: Flow patterns of Rayleigh-Taylor unstable flows, with a light fluid (light) penetrating a dense fluid (dark) under the influence of an acceleration. (a) normal perturbation, (b) surface bubble formation, (c) vortex formation between fluids of near equal density and (d) RTI for a spherical shell. Adapted from [80].

Two stages of the implosion of an ICF capsule are unstable. The first of these is at the outer surface of the shell, where the ablation of low-density plasma accelerates the dense material inwards. This may even lead to rupture of the shell [74]. The second unstable stage occurs towards the end of the implosion where rising pressure in the low-density fuel preceding ignition decelerates the incoming denser fuel shell.

Following the modified Takabe relation [67, 81] the growth rate of a laser driven instability γ in terms of fluid acceleration g, density gradient scale length L and ablation velocity v_a for surface perturbation wavenumber k is given by

$$\gamma = \sqrt{\frac{kg}{1+kL}} - \beta_a k v_a, \tag{2.4}$$

indicating that shorter wavelength perturbations (higher k) are dampened by material flow and establishing the relation between RTI growth and velocity (= mass ablation rate divided by the density at the ablation front) [81]. The quantity β_a is a numerical coefficient equal to 1.7 - 4 for laser driven ablation. The linear growth of ablative RTI modes is smaller than classical due to the negative $\beta k v_a$ term and the shortest wavelength perturbations are stable [67].

The need to mitigate plasma instabilities and RTI has led to the use of moderately thin shells in ICF pellet design. A thicker shell requires a higher intensity to achieve an equivalent shell compression (see section 2.1.1) but the shell needs to remain intact during compression. RTI growth can also potentially limit the densities achieved in ICF by inducing mixing of hot and cold fuel and destroying the spherical symmetry.

In the regime of direct drive ICF the mass ablation rate $\dot{m} \propto I^{1/3}$ and the pressure $p_a \propto I^{2/3}$, for intensity of the driver beams I and constants of proportionality set by the absorption. The velocity $v_a \propto p_a/\dot{m}$ [51]. For a given pressure, a larger, thinner shell that encloses more volume can be accelerated to a higher velocity than can a thicker shell of the same mass, where the peak implosion velocity determines the minimum energy required for ignition [76]. From this it would be beneficial to have a large pellet aspect ratio $R/\Delta R$, for shell radius and thickness R and ΔR [76]. However, to control RTI, which is most prevalent when the shell thickness is approximately equal to the perturbation wavelength, this aspect ratio is limited to $\approx 25 - 35$, with corresponding pressures in the order of 100 Mbar [76]. Classical RTI growth (without the negative term in equation (2.4)) would be

incompatible with ICF because it would limit the in-flight aspect ratio $R/\Delta R$ to less than 10 and so ultimately requires an unfeasible size of explosion [67].

The RTI is reduced by choosing operating conditions where stabilising effects are enhanced and by limiting initial seeds and designing targets with a not too large in-flight aspect ratio [67]. This last requirement limits the achievable implosion velocities and sets an upper bound to the specific energy dE deliverable to the fuel and hence the achievable density and pressure of the compressed fuel [67].

In an experiment conducted by Key et al. [5], using the Nova laser, LLNL, the short wavelength and high-brightness of EUV lasers were exploited in the study of high-electron-density plasmas, undergoing shock compression and during instability formation. From modelling they had established that early imprinting of laser intensity non-uniformities onto fusion targets (time $<$ 1 ns) would be responsible for the subsequent instabilities. Results showed that 5% changes in EUV intensity could be attributed to 0.4% changes in sample thickness, demonstrating the accuracy of the EUV probe [5]. Subsequent work explored the use of different target materials and speckle patterns, in order to better determine the effect of RTI [45, 46, 47, 48, 83, 84].

EUV sources have allowed RTI probing for thinner targets, compared to studies conducted with x-ray backlighters. The lower transmission found at EUV wavelengths also allows for detection of finer details in the instability. The transmission T through the target is

$$\frac{I}{I_0} = T = exp(-\sigma_s \ \rho \ z) \tag{2.5}$$

where I and I_0 are the transmitted and incident probe intensities, σ_s is the specific absorption coefficient (opacity), ρ is the mass density and z is the target thickness in the direction of probing. Therefore a small change in transmission, given by $\Delta T = -\sigma_s\ \rho\ T\Delta z$, allows detection of small perturbations in the expanding plasma.

Work described by Taylor et al. [83], 1996, and Kalantar et al. [47], 1997, concerned using longitudinal radiography with an EUV probe to study RTI on thin foils (2 - 3 μm). In both cases 2D or 3D modelling was used to simulate the effect of seeded modulations on the development of RTI. The work by Taylor et al. [83], concluded that hydrodynamic flow dominates the imprint, which makes RTI suitable for study by radiation-hydrodynamic codes.

In determining growth rates from radiographic measurements an accurate knowledge of opacity is required. Experiments conducted at the time often incorrectly assumed that opacity remains near constant. This led to inaccuracies in the determination of instability growth [5, 46, 47]. In this project the modelling of RTI has been expanded upon, using the most recent proposals for direct-drive ICF as a starting point and including the results from modern opacity codes (see section 2.2.2).

2.1.1.2 Progressions in inertial fusion energy

Fast ignition (FI) was proposed, where a short pulse laser is used to produce fast electrons or protons to further heat and ignite the fuel, reducing the driver energy and the stringent symmetry requirement for the driver beams [78] (see figure 2.3).

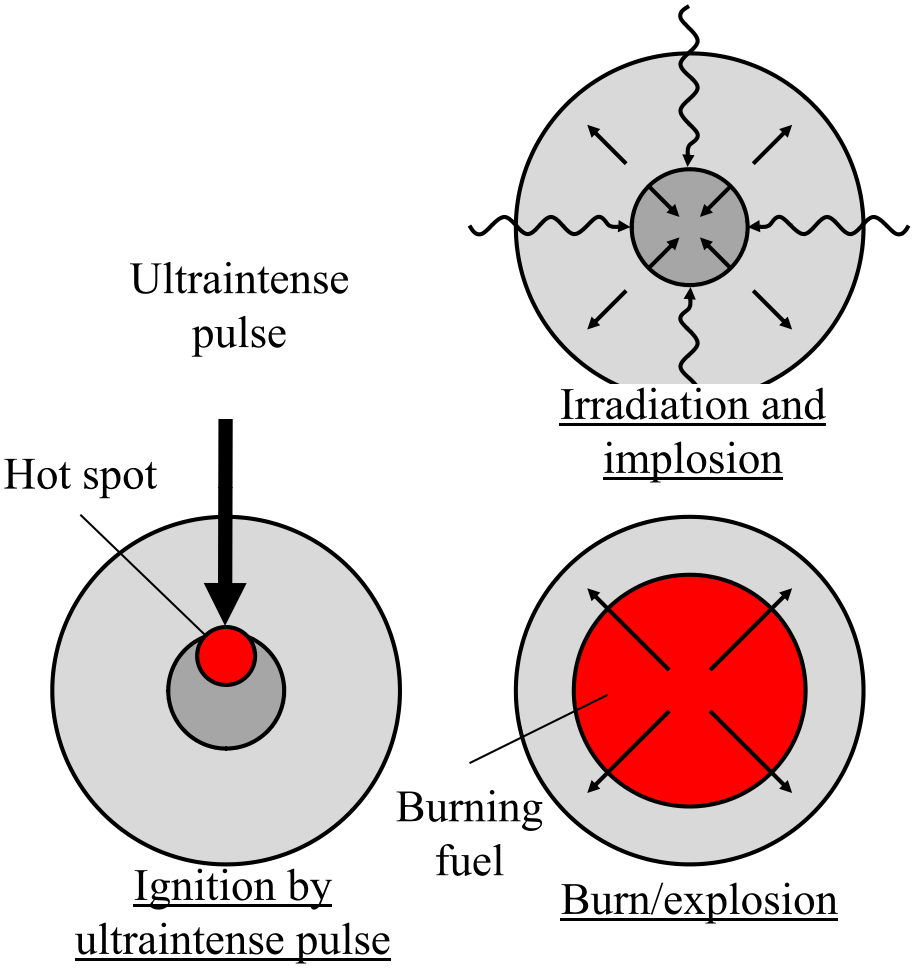

FIGURE 2.3: Scheme for fast ignition by an ultraintense beam. Adapted from [75].

FI explored boring holes into the pellet using another laser pulse, through which an ultrahigh-intensity ignition pulse can pass to create hot electrons. The method works in three stages. First, the pellet undergoes laser driven implosion to create a dense core. A corona of ablated material forms around the pellet, through which a high-intensity ignition pulse bores. The corona can be hundreds of microns in depth and pulse intensities of up to $\sim 10^{20}$ W cm^{-2} are required to push the critical density closer to the pellet core, thereby creating a path for a subsequent ultrahigh-intensity beam ($< 10^{20}$ W cm^{-2}). Hot electrons are created and propagate from

the critical density towards the core. Energy is imparted to local electrons and then to the fuel ions [78].

Later, use of a gold cone embedded into the pellet has been considered to mitigate instability formation in the channel for the ignition pulse [85]. With the cone inserted deep into the pellet, the ignition pulse will deposit its energy closer to the core reducing the total energy required.

When the ultrahigh-intensity ignition pulses are generated a prepulse also forms, borne from ASE within the laser system and nonlinear chirp in CPA. A large scale-length plasma has been seen to form inside the cone, preventing the ultrahigh-intensity pulse from reaching the cone tip and reducing the energy carried by the hot electrons to the core [86]. In some recent experiments the use of plasma mirrors has been explored, to enhance the intensity contrast between main and prepulse [87]. Frequency doubling further increases the laser contrast, due to the poorer conversion of the ASE pulse [88].

An alternative approach under consideration for ICF is shock ignition [75]. First the fuel pellet is symmetrically irradiated, to create a central hot spot, as in conventional ICF, but with acceleration to slightly lower velocities. At this point the temperature of the fuel core is too low for ignition. Arrays of laser sources at higher intensities then drive a strong shock wave converging on the centre of the pellet, raising the temperature and causing ignition. The scheme of shock ignition is depicted in figure 2.4. Compared to cone-guided FI, the target designs are much simpler and, unlike the FI scheme, an ultraintense pulse for ignition is no longer needed. However, the problems of instability formation are not removed.

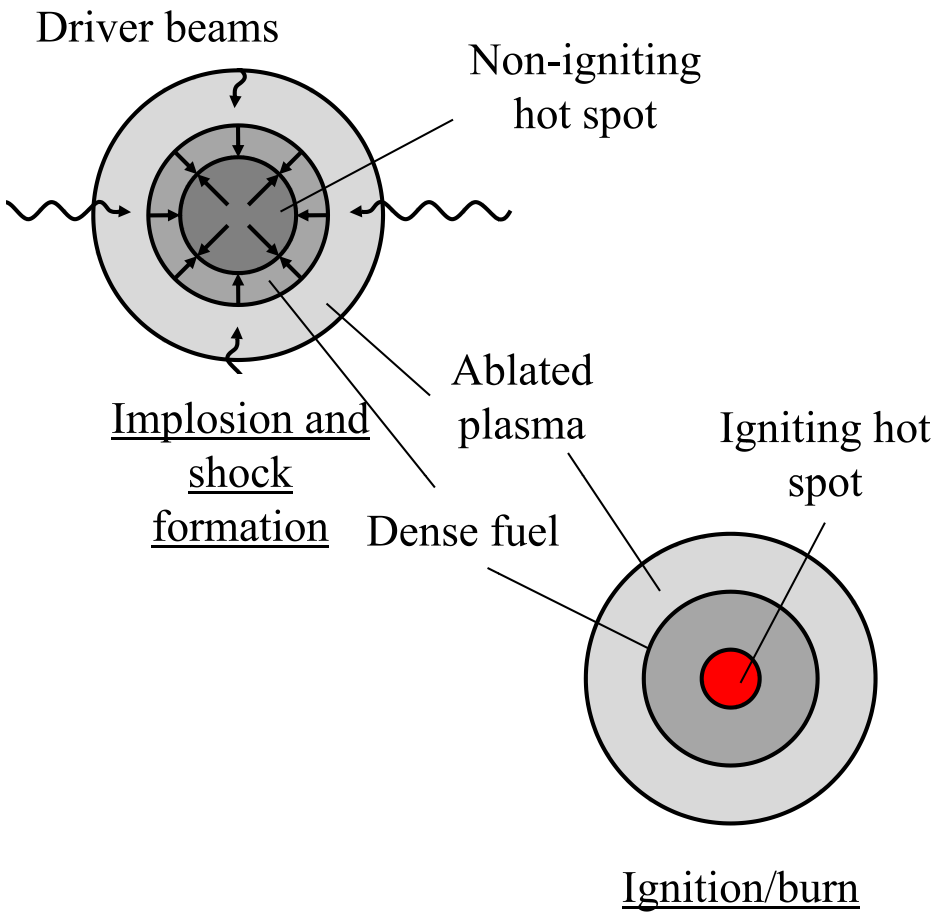

FIGURE 2.4: Scheme for shock ignition. An intense laser pulse drives a strong shock inwards, igniting the fuel. Adapted from [75].

For indirect drive laser fusion an array of laser beams irradiate the inner walls of a high-Z hohlraum, creating a plasma which will generate thermal radiation in the x-ray region (see figure 2.5). The radiation is confined within the hohlraum, and works to drive the implosion of a D-T fuel pellet [75]. Modelling requires knowledge of opacity of high-Z materials, which will determine the fraction of energy lost to the hohlraum wall [75]. Instability formation should be reduced by employing thermal radiation for ignition, compared to laser driven direct-drive ICF [75].

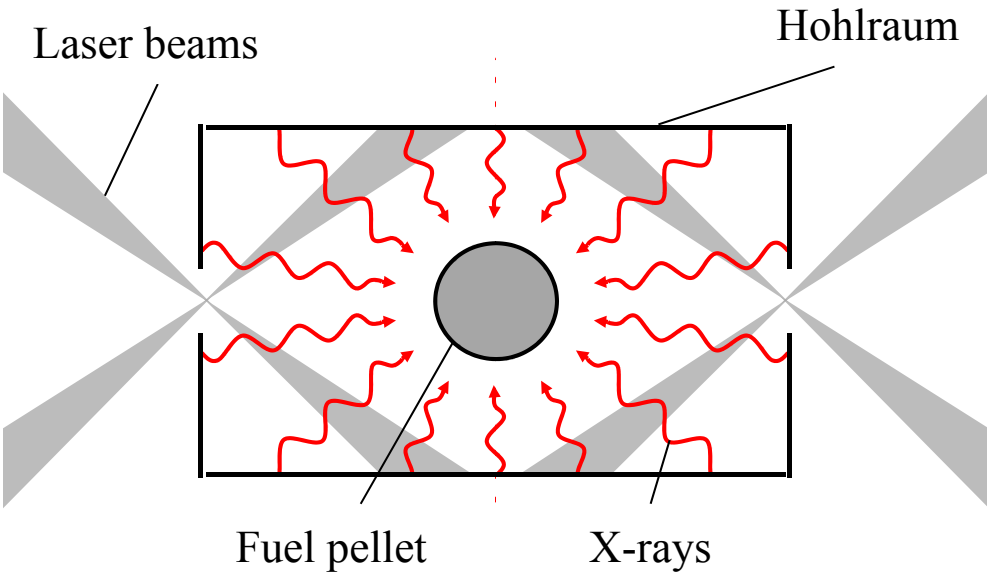

FIGURE 2.5: Scheme for indirect drive ICF. Adapted from [75].

2.2 The opacity of iron

Accurate opacity data is needed for the above laser ablation studies, for ICF and in the study of astrophysical plasmas. Uncertainties in opacity data lead to uncertainties in the models of ICF, as errors in the opacity will alter calculations of x-ray penetration in indirect drive [89]. Once established, knowledge of opacity can be used to tailor ablation of the fuel pellet, by adding dopants of different opacity to the shell material [72].

An application of iron opacity studies to astrophysics lies in increasing the accuracy of the solar abundances, by relating laboratory data of iron opacity to solar observations. Helioseismology involves the study of solar oscillation modes, with

determined frequencies providing information on the structure and rotation of the interior of the Sun. In a paper by Bahcall et al. [90] in 2005, discrepancies between modern solar model predictions and helioseismological observations were outlined. Sound speed data, obtained using the Michelson Doppler Imager on board the Solar and Heliospheric Observatory, gave the depth of the convective zone. This was then compared with calculations from a selection of the most recent solar models. This study revealed a difference between observation and the predictions, with recent improvements in solar abundance data [91] exacerbating the problem.

A match was found when the radiative opacity was increased by 11% and it was concluded that a myriad of corrections to the radiative opacity data would be necessary to improve the model and allow accurate study of other stars [90]. The standard solar abundance of iron in the Sun gives a mass fraction of 0.00123 [91]. As a heavy element it has a notable contribution to the radiative absorption [92]. Recent studies have looked at the iron opacity under conditions close to that of the solar interior, with temperatures between 30 and 350 eV and densities near solid [53]. Experimental methods for determining iron opacity are discussed in chapter 3.

2.2.1 Definitions in opacity

For studies in plasma physics the optical depth (a dimensionless measure of opacity), τ represents the amount of absorption/extinction in a sample material, such that the ratio of remaining intensity to original intensity of the probe beam,

$I/I_0 = exp(-\tau)$ [31]. For a uniform medium it is related to the absorption coefficient κ and sample thickness L_0 as $\tau = \kappa L_0$, and to the total absorption cross section σ and number of absorbers N_{atoms} as $\tau = \sigma N_{\text{atoms}} L_0$ [31]. A number of mechanisms contribute to the opacity of a material. These are described below (see figure 2.6).

Bound-bound transitions - resonant photoabsorption

Excitation of a bound electron to a higher bound state by an incoming photon can result in a myriad of potential transitions. Each will have an associated probability for photon absorption. The levels will be effected by line broadening, such as Doppler broadening due to the atom's thermal motion [93, 94].

Bound-free transitions - photoionisation

Above a threshold, the photon energy results in ionisation of the atom, freeing a bound electron. This processes results in sharp edges on atomic spectra as the threshold is exceeded. Due to the presence of nearby electrons and ions the ionisation energy of a plasma is lower than that for solid material or an isolated atom. This effect, known as continuum lowering, limits the number of high-lying levels and decreases the ionisation energy [94, 95].

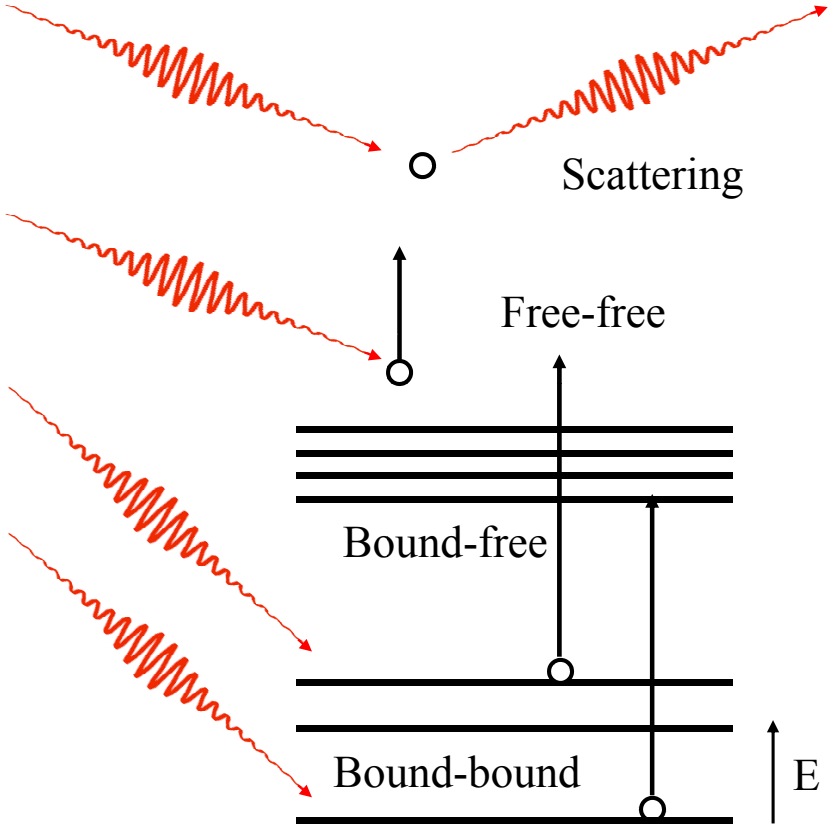

FIGURE 2.6: Atomic processes that contribute to the opacity of a material. Adapted from [95].

Free-free transitions - inverse bremsstrahlung

Inverse bremsstrahlung absorption results from free-free transitions. The presence of an ion is required for momentum and energy conservation [93, 94].

Electron scattering

Electron Thomson scattering occurs when a photon interacts with a free electron not in the vicinity of an ion. The electron can be said to accelerate due to the electric field of the radiation and this acceleration causes radiation emission. As the

cross section of this interaction is small, it will only dominate at high-temperatures where significant ionisation has decreased the rate of the bound-bound, bound-free and free-free interactions [95].

Opacity is frequency dependent. It is useful to define the average opacity, calculated using a weighting scheme. The Planck opacity uses a normalised Planck black body radiation energy density distribution as the weighting function

$$B_\omega(\omega, T_e) = \frac{15}{(\pi^4 T_e)} \frac{[\hbar\omega/(T_e)]^3}{e^{\hbar\omega/(T_e)} - 1}, \tag{2.6}$$

which is frequency (energy) $\hbar\omega$ and temperature T_e dependent [96]. Considering the absorption coefficient κ [96]

$$\kappa_{\text{Planck}} = \int_0^\infty d\omega B_\omega(\omega, T_e)[\kappa_{\text{total}} - \kappa_{\text{scattering}}]. \tag{2.7}$$

The Planck weighting scheme is applicable to radiation interaction with plasmas of low-optical-depth.

The Rosseland mean opacity uses a temperature derivative of the Planck distribution. It is often used in models of radiative transport for plasmas of high-optical-depth. The propagation of radiation in optically thick plasmas occurs through successive emissions and photoabsorptions of photons by the plasma material, akin to the diffusion of heat [94]. The model is called the diffusion approximation, and is valid whenever the radiation field is isotropic over distances $\leq$ the photon

mean free path [97]. We can write that [96]

$$\frac{1}{\kappa_{\text{Rosseland}}} = \int_0^\infty \frac{d\omega[\partial B_\omega(\omega, T_e)/\partial T_e]}{\kappa_{\text{total}}}. \tag{2.8}$$

The frequency resolved opacity κ_{total} includes the bound-bound, bound-free, free-free and scattering contributions [96].

Differences between the Planck and Rosseland mean opacities result from the variations in κ_{total} over temperature, density and frequency, where the scattering contribution $\kappa_{\text{scattering}}$ is usually negligible [96].

2.2.2 Theoretical codes for iron opacity

A variety of codes have been developed to produce tabulated opacity data for ranges of temperature and density. For a truly comprehensive opacity calculation code all absorption lines and edges within a material should be included. Methods exist for dealing with the complex level structures, particularly for moderate to high Z materials where the large number of lines make comprehensive calculations overly time consuming. This is illustrated in figure 2.7 where the contributions to a $2s - 3p$ transition are shown. The codes are generally categorised by the detail of atomic data included. Methods may be combined to allow calculations across a wide range of elements.

Detailed term accounting (DTA) calculates opacities based on vast numbers of spectral lines arising due to LS coupling within an atom (e.g. all levels depicted in figure 2.7). Energies and transition probabilities are calculated for each line

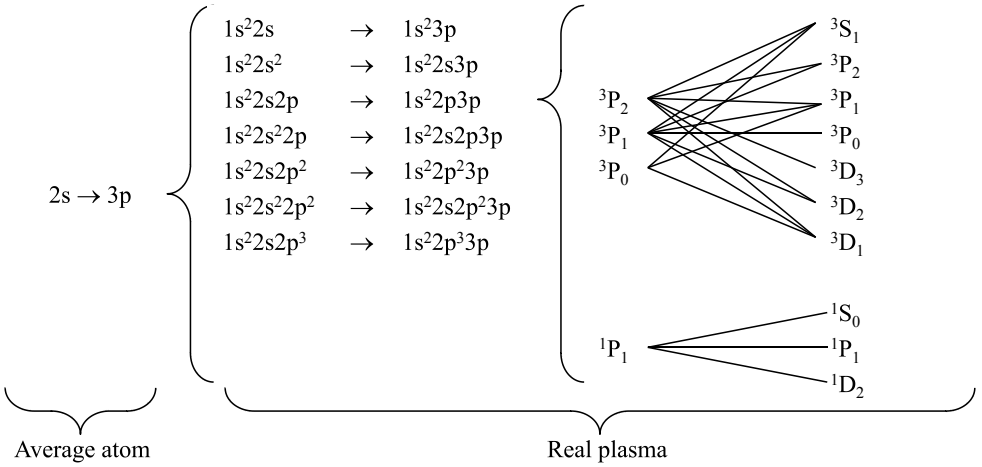

FIGURE 2.7: Contributions to a $2s-3p$ transition comparing the 'average atom' to more detailed representations where term splitting is included [98]. For the example given all the allowed electric dipole transitions between the $2s$ and $3p$ levels are displayed, indicating the complexity of many theoretical codes.

by an atomic physics model [9, 99, 100]. In the close coupling approximation (CCA) a complete wavefunction for all the contributing electrons is calculated. CCA assumes a specified number of electrons in a tightly bound state with an added extra electron being in either an excited state or the continuum following photoionisation [101]. The calculation of the wavefunction for this approximation is known as the r-matrix method. The electron-ion separation r_{e-i} is divided into two regions to describe collisional processes. For $r_{e-i} < r_{\min}$ the colliding electron is indistinguishable from atomic electrons and for $r_{e-i} > r_{\min}$, the colliding electrons sees a long range potential. From this the wavefunctions are calculated for the two regions and matched at the interface $r_{e-i} = r_{\min}$ to get the complete solutions for the energies of atomic states and transition probabilities [102].

Statistical models of plasma opacity include the average atom (AA) approach, which accounts for all relevant transitions, but in a simplified fashion that ignores detailed spectral structure. The AA model assumes a single kind of fictitious

(most probable) atom that represents the average charge/excitation/occupancy of all the multitude of species that are present in a real distribution of ionisations in a plasma. From this the transition probabilities of different electronic configurations are obtained with energy levels scaled for different ionisations [94]. Detailed configuration accounting (DCA) groups neighbouring lines, describing the different occupancies and excitation states of an ion in the plasma in terms of electronic configurations. In DCA models term splitting arising from LS coupling is ignored, however, jj-coupling is often included in the treatment of heavier elements where this will dominate. Energies and probabilities are averaged for each electron configuration to obtain the necessary atomic data [103]. Finally for methods based on unresolved transition arrays (UTA) broadened lines are assumed, weighted by the relevant Boltzmann population. Configuration term structure in atomic data generation is neglected [9, 104].

Table 2.1 gives a number of codes developed for opacity calculation together with the basis model. Comparisons of these codes can be found in the literature where, in general, high-density-low-temperature systems, known as the warm dense matter region, show the greatest disagreement [96, 104].

TABLE 2.1: Selection of codes developed for opacity calculation.

Code	**Author**	**Model**
CASSANDRA	Crowley [105]	AA and UTA
IMP	Rose [106]	DCA
LEDCOP	Magee et al. [99, 107]	DTA
OPAL	Rogers and Iglesias [108]	DCA
OP	Opacity Project Team [101]	CCA

The output of two widely available opacity codes, IMP and LEDCOP have been

compared. Both codes have been used in computational experiments carried out in this project (see chapters 5 and 6).

Ionised Materials Package (IMP) [106], developed by S. Rose, assumes a plasma in local thermodynamic equilibrium (LTE). In complete thermodynamic equilibrium all three types of particles within the plasma, namely electrons, ions and photons, are in equilibrium with each other. The ion and electron velocities are described well by a Maxwell-Boltzmann distribution [94]. In LTE electrons and ions are in equilibrium among themselves, whereas the photons are not [94]. For such plasmas, rates of collisional excitation and de-excitation dominate radiative ones. Typically the dimensions of the plasma are much smaller than the mean free path of the photons emitted within it [94]. IMP falls into the category of a DCA model, where many jj-configurations are included in the calculation of opacity. The Fermi function is used to set the principal quantum number n of the last open shell. All shells of lower n are assumed full. A statistical method is employed to deal with any satellite lines. Once the configuration is selected the Thomas-Fermi potential is evaluated and the one-electron Dirac orbitals calculated. Energies and probabilities are calculated and the Saha equation is used to obtain the probabilities of occupancy of the orbitals. The effects of Doppler broadening are then added. A combination of multiple Gaussian profiles is used for the line profiles, as it was found that with a smooth profile the opacity was overestimated for low-density plasmas. The total opacity is obtained by summing the bound-bound, bound-free, free-free and scattering contributions [106].

The Light Element Detailed Configuration Opacity (LEDCOP) code [99, 107] was

developed by the T-4 group at Los Alamos National Laboratory. It was designed for analysis of laboratory plasmas that exist in LTE with atomic numbers ≤ 30. With its roots in DTA each contributing transition is considered in detail. The model for equation of state comes from a modification of the Saha equation, with each ion stage having detailed energy levels. A relativistic, self-consistent Hartree-Fock code is used to calculate atomic physics data, including LS term energies. The Saha equation is iteratively solved to obtain a consistent set of ion abundances, occupancies of the orbitals and free electrons [107]. The occupancies are combined with the appropriate cross sections (bound-free photoionisation, free-free absorption, scattering and bound-bound line absorption), which are modified by the plasma conditions to obtain energy dependent absorption coefficients. These are then integrated over the appropriate weighting functions to provide Planck or Rosseland mean opacities [99, 107].

Figure 2.8 compares the total specific absorption cross section from the IMP and LEDCOP codes at selected frequencies in the EUV range. Iron is shown together with CH plastic, this being a common material used for pellet coating in ICF.

For CH (see figure 2.8 (a) and (b)) the agreement between IMP and LEDCOP is reasonable. From both the IMP and LEDCOP codes the increase in CH opacity for higher densities can be seen at 21.2 nm, making CH a suitable target material for studying shocks, wherein an increase in density from solid will lead to a clear increase in opacity. Finer contours appear to be missing from the LEDCOP output indicating a slower changing model.

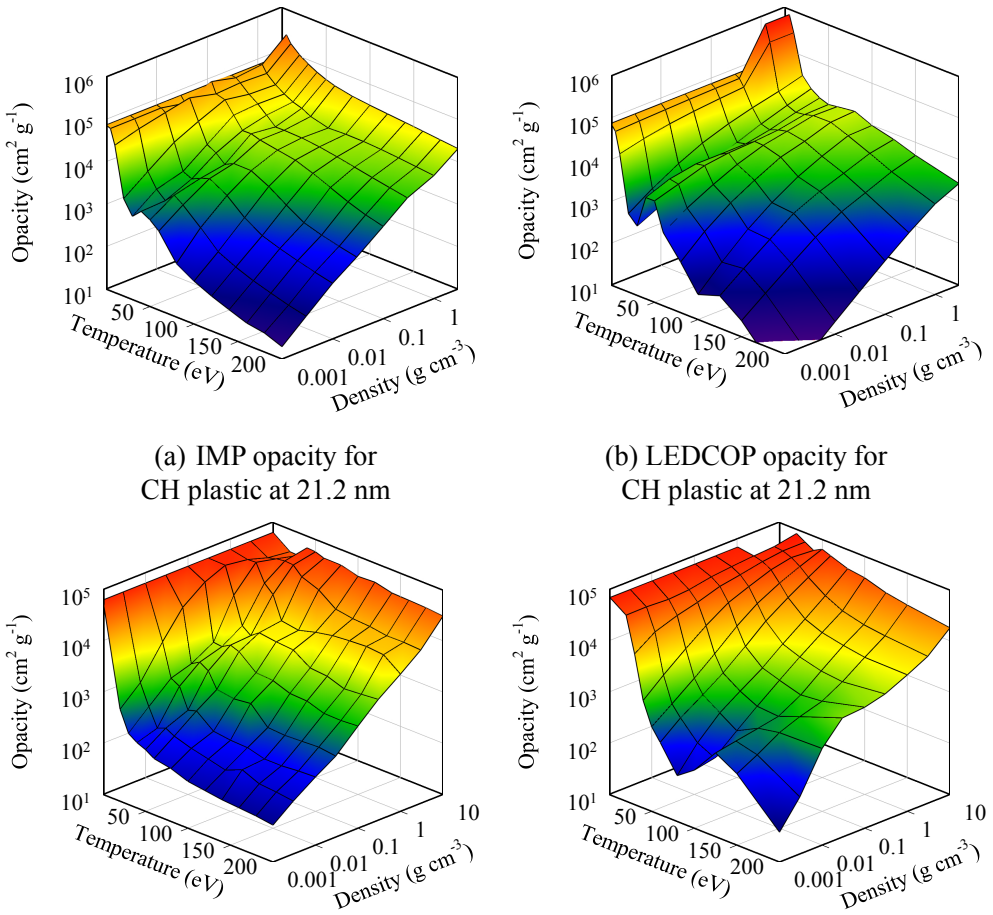

FIGURE 2.8: A comparison of IMP [106] and LEDCOP [99, 107] Planck opacities for CH plastic at 21.2 nm ((a) and (b)) and iron at 13.9 nm ((c) and (d)) for temperatures between 1 and 200 eV and densities between 0.001 and 10 g cm^{-3}.

The agreement for iron, at densities below $\sim$ 0.1 g cm^{-3} and across the temperature range shown, is poorer (see figure 2.8 (c) and (d)). The low-temperature and high-density values are reasonable, but for moderate to high-temperatures and moderate to low-densities the opacity values deviate. For the case of a 13.9 nm probe and iron, structure present in the LEDCOP opacity code at 150 eV and 0.001 g cm^{-3} gives a value for Planck opacity that is approximately 4 times higher than that given by IMP. The agreement at high-density suggests that both codes have equal inclusions of continuum lowering effects. For lower densities and higher

temperatures, the opacity of iron is dominated by spectral lines, rather than continuum effects. It is therefore the treatment of the line profiles from which the differences arise [109].

Previous comparisons of the Planck opacity for iron, carried out at the 1997 international LTE opacity workshop and code comparison study, studied temperatures between 15 and 100 eV and densities between 10^{-5} and 50 g cm^{-3}. This study highlighted the differences that arise from using DTA, as is used in LEDCOP, as opposed to those using the statistical, UTA, approach, as done in other codes such as CASSANDRA [96]. Statistical theories assume that all lines belonging to the same transition overlap due to broadening and can be represented by a Gaussian profile. At lower densities this assumption breaks down, and individual line shapes must be included [104]. This may result in an underestimation of the opacity. These differences highlight the necessity for improvements to the iron opacity model. Disagreements exist between the codes, due to differing calculations and the lack of comprehensive experimental data.

Also in wide use is data from the Opacity Project (OP), borne from international collaboration, and the OPAL code, developed at LLNL. The function of OP is in calculating atomic data required for stellar opacities and Rosseland mean opacities, which it achieves by a CCA method [101]. OPAL makes use of DCA, as IMP, but with atomic data calculated from parametric potentials rather than with Thomas-Fermi potentials [108]. Comparison between these codes indicated the need for addition of large numbers of inner shell transition lines. The inclusion of these lines in OPAL revealed a feature of iron opacity, the 'z-bump', at $\sim$ 20 eV, which

was not given by the OP data [95]. The basis of many more codes and rigidity to testing is covered in the literature. The reader is referred to a summary paper covering these issues by F.J.D. Serduke et al. [96], in 2000. Here it was concluded that, although agreement to the data could be found for some regions, additional experimental data is needed to establish a widely applicable code, which could be confidently used in modelling the opacity of iron at densities 10^{-5} g cm^{-3} to solid state density and temperatures up to a few hundred eV [96].

2.3 Refractive index of plasmas

In this thesis interferometry at EUV wavelengths has been used to study plasmas, at densities inaccessible to longer wavelength radiation. Electron densities above an order of magnitude lower than the probe critical density N_{crit}, with

$$N_{\mathrm{crit}} = \pi/(r_0\lambda^2)\mathrm{cm}^{-3} \tag{2.9}$$

for classical electron radius r_0 and laser wavelength λ, lead to non-penetration in optical probing. EUV probing transverse to the density gradient is limited due to refraction effects which scale with density [110], as noted in equation (1.2) (section 1.2) and x-ray probing is hampered by increased scattering from unablated material. On the other hand, EUV interferometry arranged for longitudinal probing through an ablated target (parallel to the target normal), provides data on the dense region between the ablation and critical surfaces, which would otherwise be inaccessible.

During ablation the laser radiation is absorbed up to the critical density, at which point absorption or reflection may occur. Therefore, in order to diagnose the plasma, probing must be carried out at wavelengths much less than that of the ablating beam. For example, taking N_{crit} for a fully ionised CH plasma at solid density ($\rho = 1.11$ g cm^{-3}) the maximum wavelength for probing, without absorption associated with the critical density, is ≈ 55 nm. Understanding this region of warm dense matter between the ablation and critical density is crucial for ICF and solar models where solid state and plasma descriptions both fail to properly describe it [111, 112].

A measurable quantity for EUV interferometry of plasmas is the phase shift, relative to vacuum or a solid target of equal path length L. The phase shift $\Delta\varphi$ in radians arises from the path difference between the portion of the probe beam passing through the sample (ablated target, plasma plume) $k\eta_{\text{sample}}$ and that portion passing through the reference (vacuum or solid target) $k\eta_{\text{reference}}$ for wavenumber k and refractive index η. The total phase shift comes from integrating over the entire sample in the direction of probing z. As introduced by equation (1.5) in section 1.2.2, the number of fringe shifts n_{fringe} detected when carrying out interferometric probing of a plasma relative to vacuum is given by

$$n_{\text{fringe}} = \frac{\Delta\varphi}{2\pi} = \frac{1}{\lambda}\int_0^L (\eta_{\text{sample}} - \eta_{\text{reference}})dz$$

with the refractive index of a vacuum $\eta_{\text{reference}}$ being equal to 1 for equation (1.5). Figure 2.9 depicts the situation when the reference beam passes through a solid target. The total path length L for each portion of the EUV probe beam must

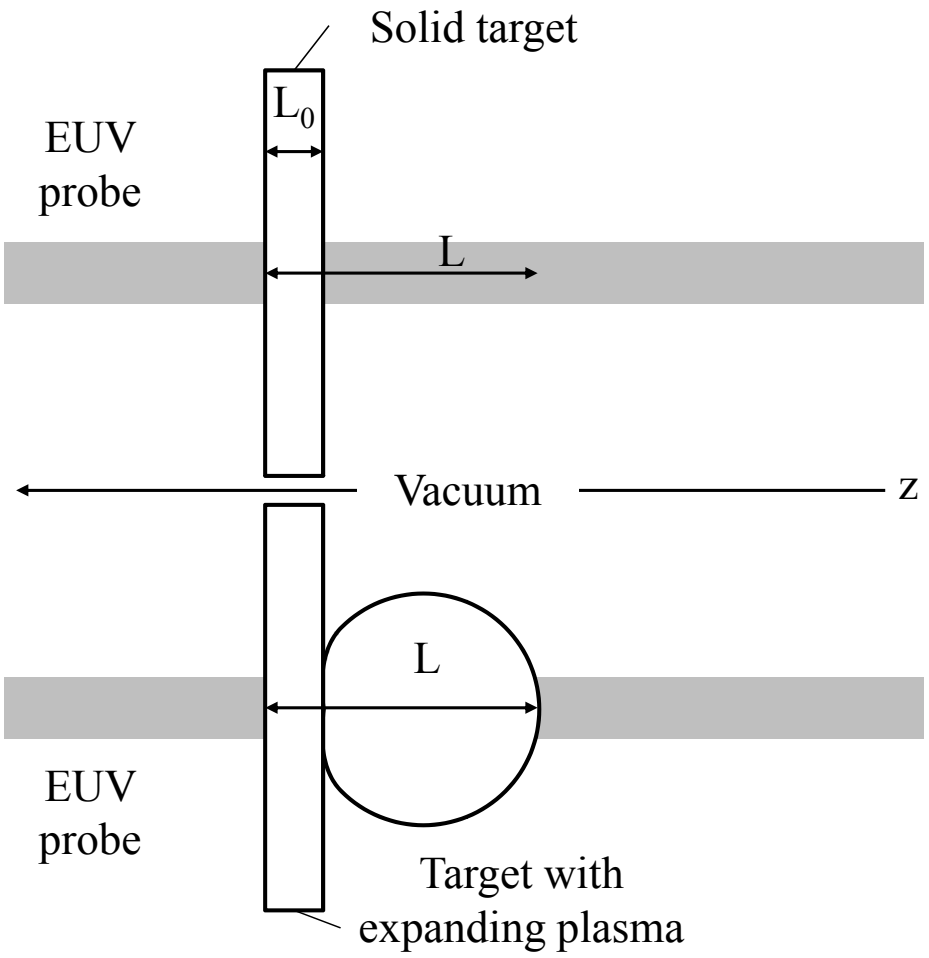

FIGURE 2.9: Depiction of the path length to be used when conducting longitudinal interferometry, where one portion of the EUV probe beam passes through the sample target and the other through the solid target.

be equal, therefore $k\eta_{\text{reference}}$ must account for the solid target and vacuum. The resulting number of fringe shifts is now

$$\begin{aligned} n_{\text{fringe}} &= \frac{\Delta\varphi}{2\pi} \\ &= \frac{1}{\lambda}\left[\int_0^L \eta_{\text{sample}} dz - \eta_{\text{reference}} L\right] \\ &= \frac{1}{\lambda}\left[\int_0^L \eta_{\text{sample}} dz - (\eta_{\text{solid}} L_0 + L - L_0)\right] \end{aligned} \tag{2.10}$$

for original target thickness L_0. So, for example, for interferometry of a hole in a solid target $\eta_{\text{sample}} = 1$, $L = L_0$ and, as $\eta_{\text{solid}} < 1$ at EUV wavelengths

$\Delta\varphi > 0$, defining a 'positive' phase shift for this work. A diagnostic for creating EUV interferograms, and the subsequent image processing required to extract the phase shift, is described in section 3.3.

2.3.1 The role of the refractive index in plasma studies

Through studies using EUV interferometry, it is possible to determine the electron density and ionisation of plasmas. However, a model of refractive index at EUV wavelengths is needed. For low-density, high-temperature plasmas, the refractive index is well described by considering only the contribution from free electrons η_{plasma}. Here

$$\eta_{\text{plasma}} = \left(1 - \frac{N_e}{N_{\text{crit}}}\right)^{\frac{1}{2}} \approx 1 - \frac{N_e}{2N_{\text{crit}}} \tag{2.11}$$

for $N_e \ll N_{\text{crit}}$. However, for cooler, denser plasmas (i.e. warm dense matter) the effect of absorption due to bound electrons must be included. Bound-bound and bound-free absorption features contribute to the refractive index leading to complex variations with wavelength. The same benchmarking and code development necessary in opacity studies can be used to provide a model for refractive index, where the two are linked through the Kramers-Kronig relations.

2.3.2 Kramers-Kronig relations

The refractive index η can be regarded as a complex quantity $\eta^* = 1 - \delta - i\beta$, with the real and imaginary parts of the refractive index given by $1 - \delta$ and $-\beta$ respectively. The Kramers-Kronig relations describe the connections between the

real part of this expression (determining the phase of the beam) and the imaginary part (determining the beam attenuation or absorption). These relations can be derived using the principal of causality where, in the most basic terms, "no output can occur before the input" (Toll, 1956 [113]). In other words no information carried by the beam can travel faster than the speed of light in a vacuum c (despite conditions arising where $\eta = c/v < 1$). Within a dispersive medium it is only the phase velocity v_p that can be greater than c. In such situations dispersive relations apply and the beam propagates through space at the group velocity. As a consequence of this limitation, the absorption and dispersion processes are linked and one can be derived from the other. For a rigorous proof of the equivalence of causality and the dispersion relations the reader is referred to [113].

With the Kramers-Kronig relations it is possible to link the real and imaginary parts of the frequency dependent complex refractive index η^* with

$$\delta(\omega) = \frac{2}{\pi}\int_0^\infty \frac{\Omega\beta(\Omega)d\Omega}{\omega^2 - \Omega^2}[114]. \tag{2.12}$$

The dimensionless quantities of refractive index η and optical depth (opacity) τ describe the change in phase and decay in amplitude of a wave as it enters a new medium. They are linked by the complex propagating wavevector $\mathbf{k}^*$ ($k = 2\pi/\lambda$) with $\eta = c/v_p = (c/\omega)\Re(k)$ and $\tau = (c/\omega)\Im(k)$ for angular frequency ω [115]. Therefore, as it is possible through the Kramers-Kronig relations to link the real and imaginary parts of the complex wavevector $\mathbf{k}^*$, the real refractive index can be derived knowing the opacity.

It is useful to consider the relation between real and imaginary components of the complex refractive index η^* in terms of atomic scattering factors f_1 and f_2, which are defined by $\delta = f_1 N_i/(2N_{\text{crit}})$ and $\beta = f_2 N_i/(2N_{\text{crit}})$ with ion density N_i. f_2 can be calculated from the opacity. By combining equations (2.11) and (2.12) with the new expressions for δ and β and taking the number of free electrons per ion $\bar{Z}^* = N_e/N_i$ a more complete expression for the real refractive index η can be derived. In terms of energy E

$$f_1(E) = \bar{Z}^* + \frac{2}{\pi} P.V. \int_0^\infty \frac{\varepsilon f_2(E) d\varepsilon}{E^2 - \varepsilon^2}, \tag{2.13}$$

with refractive index $\eta = 1 - f_1 N_i/(2N_{\text{crit}})$ [116] and where the solution is obtained by taking the principle value (P.V) of the integral. This represents a more complete expression for the refractive index, where experimental or theoretically derived opacities can be used to calculate the contribution of bound electrons. In chapter 6 a model for refractive index, and from this phase shift, for EUV interferometry measurements of an ablated CH plasma is presented.

Summary

Within this chapter the motivations behind studies of laser ablation, opacity and refractive index have been given, together with difficulties that have arisen. The application of EUV lasers to these studies has been suggested and justified, in order to probe high-density plasma; inaccessible to alternate wavelength radiation.

The following two chapters detail the experimental diagnostics and simulation codes used in this work.

Chapter 3

Diagnostics and their interpretation

This chapter contains introductory descriptions of experimental tools used to undertake the work of this thesis. A simple diagnostic utilised for imaging a line plasma is presented. A double Lloyd's mirror has been used to carry out interferometry at EUV wavelengths and is described followed by an outline of the method of complex interferometry, which allows simultaneous extraction of phase shift and transmission data. The use of a flat field spectrometer, capable of recording EUV transmissions for both broad and narrowband sources, is then discussed.

3.1 Diagnostic for spatial resolution of a plasma

3.1.1 Crossed slit camera

A crossed slit camera has been employed in monitoring the line focus in a plasma used to create a germanium emission source. For the work covered in this thesis a germanium broadband EUV source was created to probe iron opacity targets, and is discussed in section 3.2 and section 5.3 (see figure 3.1).

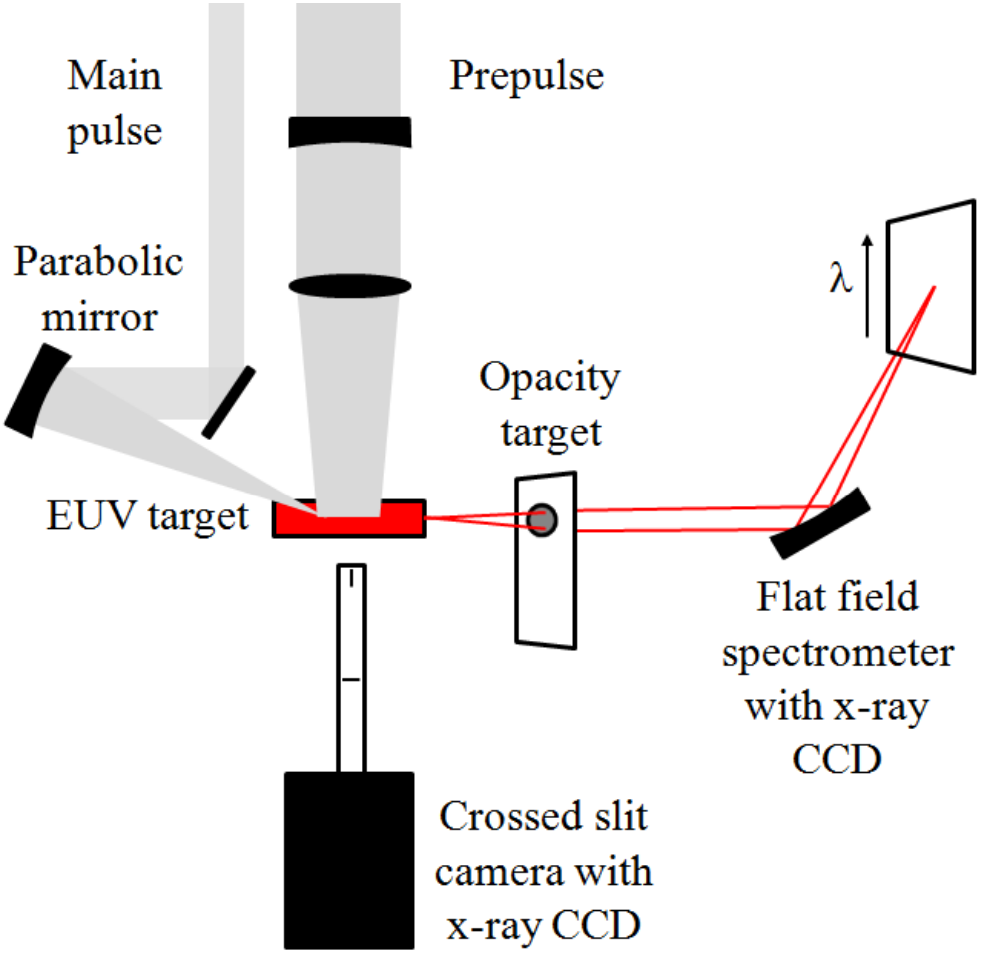

FIGURE 3.1: Experimental arrangement for broadband EUV probing of thin (50 nm) iron targets. The EUV source is created at the germanium target and monitored with a crossed slit camera. The EUV beam and heating beam are both incident on the front side of the opacity target. The throughput then passes to a flat field spectrometer and CCD.

To form the crossed slit camera, two slits are positioned orthogonally at set distances from the plasma, providing magnification at the image plane (here a CCD camera). 3 μm aluminium and 25 μm beryllium filters have been used to block visible light, which would otherwise lead to overexposure of the CCD camera. The filtering employed allowed detection of radiation with photon energy $\gtrsim$ 900 eV. Figure 3.2 shows images obtained using the crossed slit camera, with irradiation solely by a prepulse (a) then by the main pulse (b) and then both pulses (c).

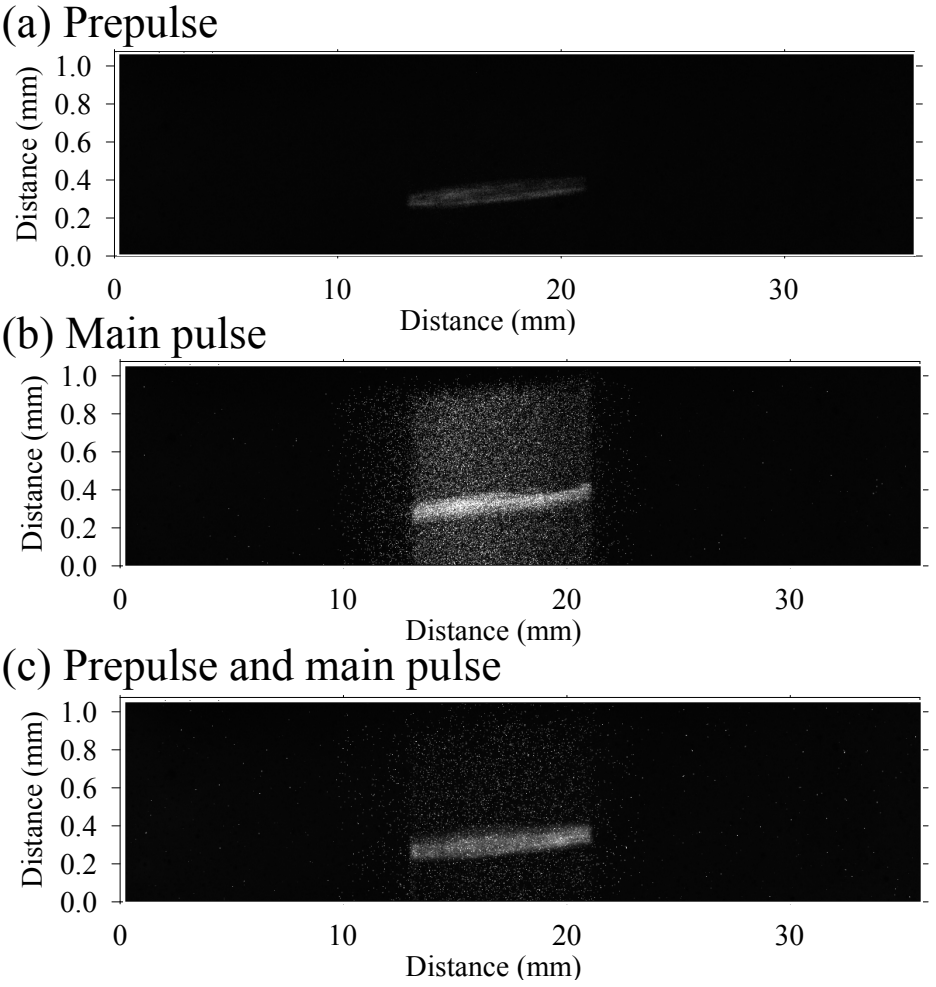

FIGURE 3.2: Crossed slit camera images of a germanium target irradiated by optical pulses in a line focus. The plasma line is $\sim$ 8 mm by 0.1 mm. (a) was taken of the germanium target irradiated by the prepulse, (b) by the main pulse and (c) by both. The three images displayed are all background corrected and presented with equal brightness and contrast.

This diagnostic was used to ensure overlapping of the prepulse and main pulse in line focus, for production of the germanium broadband EUV source (see sections 3.2 and 5.3).

Referring to figure 3.2 comparing (b) and (c), a lower intensity of emission is seen when the main pulse is applied in conjunction with the prepulse compared to the emission with just the main pulse. By creating the preplasma, there is a larger under-dense region for absorption of the main pulse. In this case the plasma has reached a lower temperature with the combination of prepulse and main pulse, producing less radiation with photon energy > 900 eV.

3.2 Diagnostic for measurements of opacity at EUV wavelengths

3.2.1 Flat field spectrometer

A flat field spectrometer has been used as the primary diagnostic in an experiment to measure opacity from the transmission of EUV light through thin (50 nm) iron targets [117] (see figure 3.1, section 3.1). In conjunction with experiment, simulations of iron target ablation were carried out by the author, the details of which can be found in chapter 5.

The spectrometer is constructed around an aberration-corrected, concave, aperiodically ruled grating (Hitachi 001-0437) that produces a flat focal plane, allowing

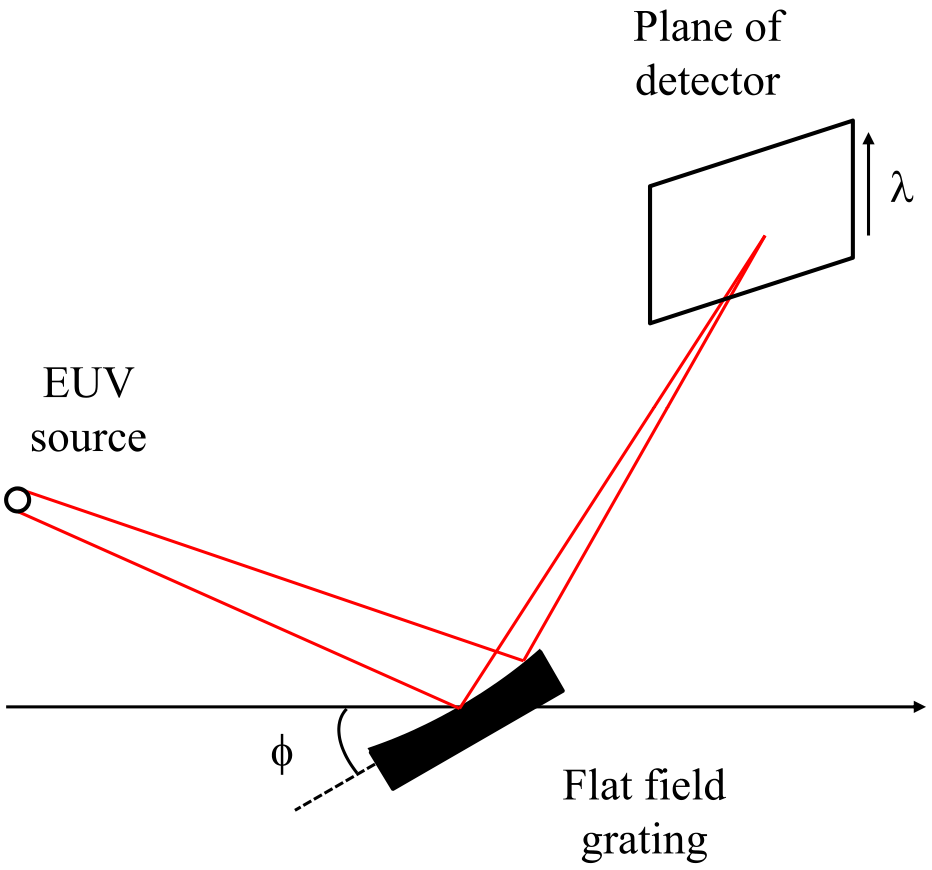

FIGURE 3.3: A schematic for use of a flat field grating in EUV probe opacity experiments.

a planar detector, such as a CCD to be used. The incoming EUV beam is directed at a grazing angle onto the grating, for high-reflectivity [118]. The beam is focused in the vertical direction and spectrally resolved with frequency (energy, wavelength) given by the vertical displacement at the focal plane. Spatial information is given in the horizontal direction [117]. Figure 3.3 gives a schematic of the geometry used in ray-tracing a flat field grating.

Ray tracing methods proscribe the position of the plane of the detector. In figure 3.4 the focal plane has been mapped for typical experimental parameters [117].

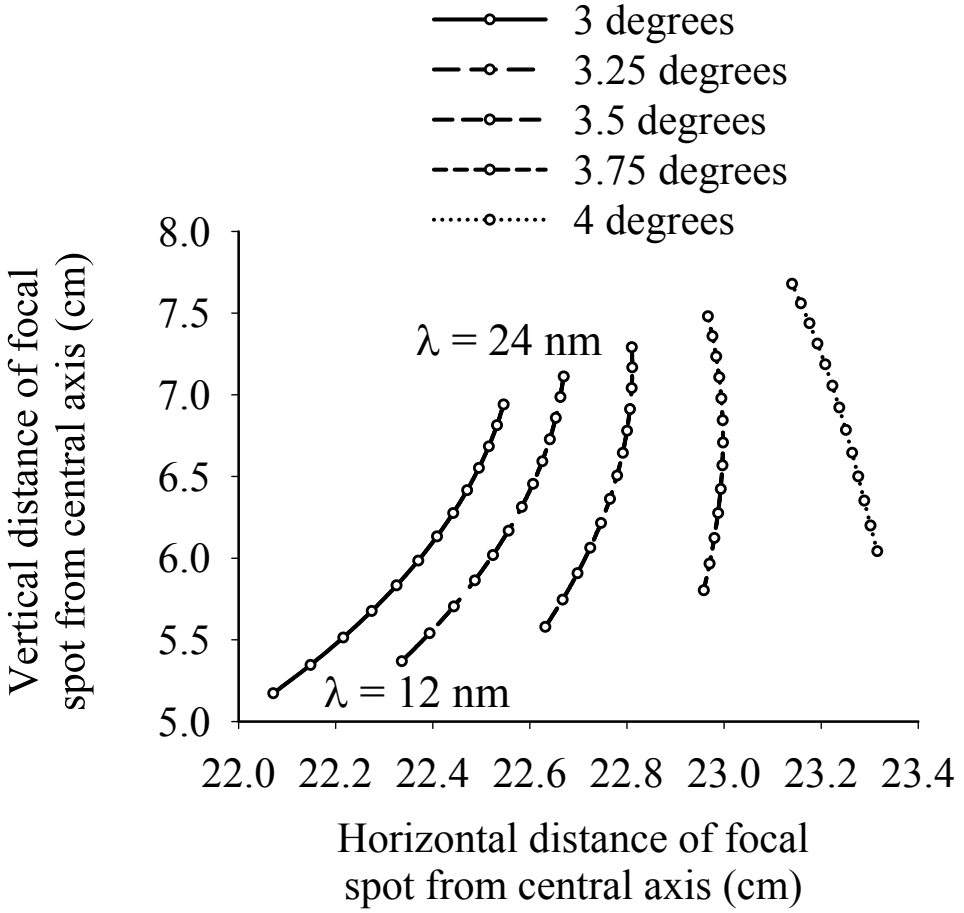

FIGURE 3.4: By considering the relevant parameters, together with use of a ray-trace code produced by F. Strati at the University of York [119] the focal plane has been mapped. A series of curves are shown, distinguished by the grating angle ϕ, with axis defined by the beam direction. The grating has 1200 lines/mm, with the source 600 mm before the grating. The circles indicate focussing positions for wavelengths from 12 - 24 nm spaced at 1 nm intervals.

As ray tracing reveals, longer wavelengths will be seen higher on the plane of the detector, thereby dictating the detector size and position. Once the spectra is obtained, line-outs reveal the strength of signal and, in comparison with cold transmission data, the absorption coefficient for the opacity sample. It has been possible to obtain transmission data from plasma emission from germanium targets. A sample image is given in figure 3.5 where multiple emission lines from the germanium backlighter can be seen. Images were taken through the iron target

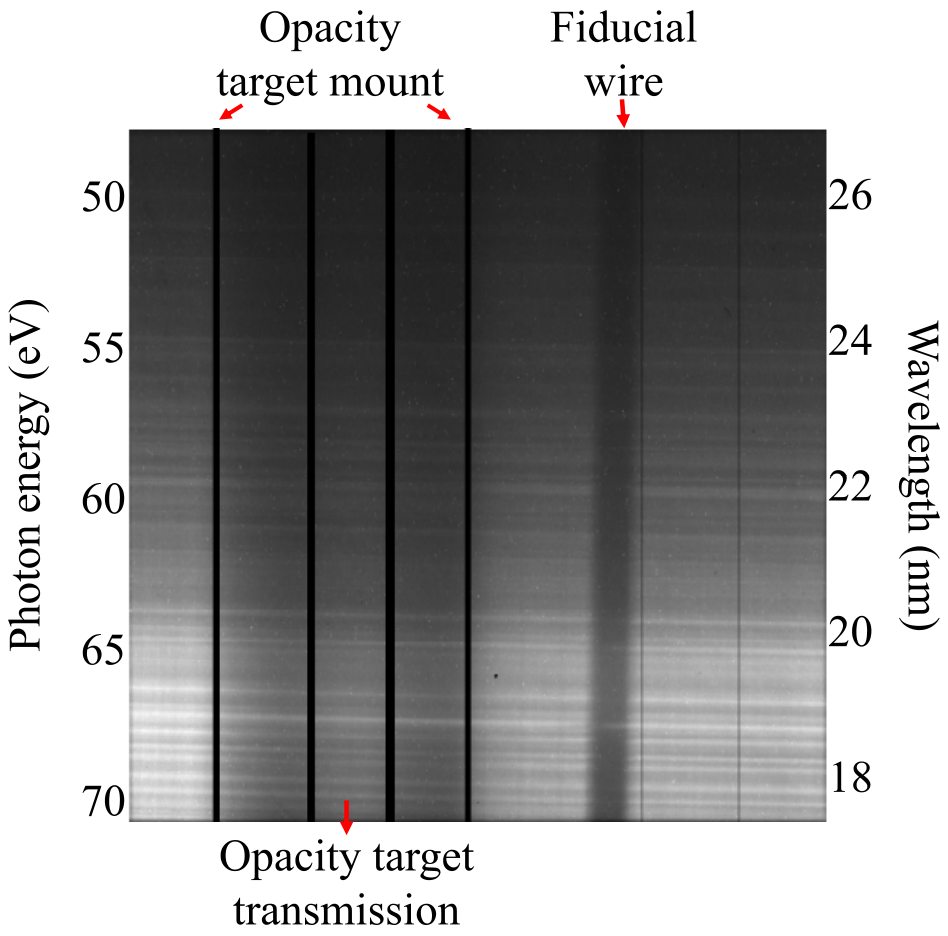

FIGURE 3.5: A CCD image from a flat field spectrometer showing EUV backlighter emission through a thin (50 nm) iron target. The flat field spectrometer resolved the EUV spectrum with wavelength (photon energy) given by vertical displacement as shown [117].

with and without heating and with different delays between target heating and EUV backlighter emission.

By use of the flat field spectrometer, experimental values of transmission were obtained at EUV wavelengths. These are shown in chapter 5 in comparison with simulated transmissions. Further simulation gives predicted uniformities of the iron plasma and the suitability of the measurements for calculating opacity.

3.3 Diagnostic for measurements of laser ablation at EUV wavelengths

3.3.1 Double Lloyd's interferometer

A double Lloyd's mirror wavefront-splitting interferometer [120] has been employed to produce interference patterns at EUV wavelengths. Two independently adjustable flat surfaces operate under grazing incidence to reflect the EUV beam (for the work of this thesis a 21.2 nm zinc EUV laser). Interference fringes are produced at the required distance and with a tunable fringe period, adjusted by altering the angle between the mirrors. The interferometer works by reflecting one portion of the incident beam from the first mirror and another from the second mirror. An interference field exists in space in the region where the two reflected waves are superimposed [121]. The images of the source in the two mirrors can be considered as separate coherent sources [121]. The fringe separation at the detector, Δy is given by

$$\Delta y = \frac{\lambda}{2\phi - \alpha} \tag{3.1}$$

for wavelength λ, mirror angle ϕ and beam divergence α [120] (see figure 3.6). Assuming zero divergence in the far field and with a mirror angle $\phi = 0.6$ mrad for this work $\Delta y = 17$ μm with no dependence on the incidence angle of the beam [120].

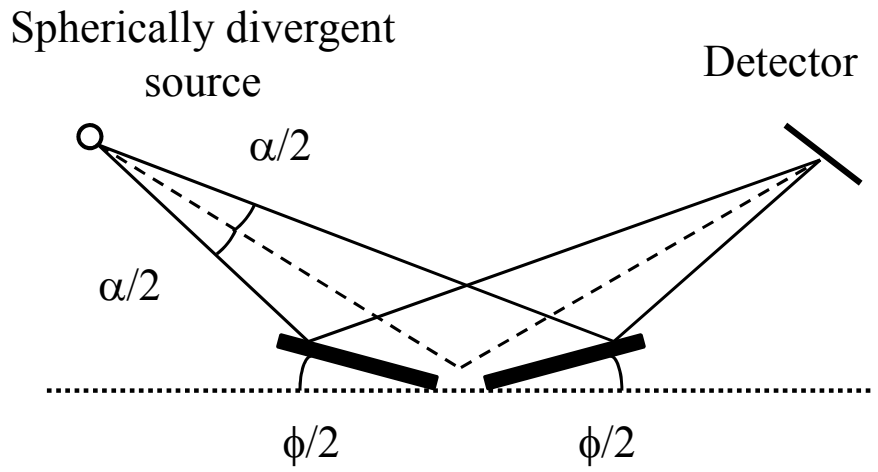

FIGURE 3.6: Geometry of a beam reflected by the double Lloyd's mirror. The focus of the source is at the detector. Both halves of the beam leave the source and then one half reflects from the first mirror and the other from the second mirror, inducing a path difference. The two half beams then cross over resulting in an interference pattern at the detector [120].

There are advantages with the double Lloyd's mirror interferometer over conventional, amplitude-splitting interferometers, such as the Mach-Zehnder interferometer. The double Lloyd's interferometer eliminates the need for the beam to be split by a transmitting optic, which can reduce the amplitude of the beam passing through the probed plasma [120]. A brighter beam would then be required to overcome the sample self emission.

Conventional interferometers are hindered by the need to manufacture ultra-thin high-transmission beam splitters at EUV wavelengths. To demonstrate the thickness required for a beam splitter, figure 3.7 (a) gives the attenuation length for bulk SiO_2 across EUV wavelengths from 5 to 40 nm.

In silica, attenuation occurs on a sub-micron scale at EUV wavelengths. Consequently amplitude-splitting EUV interferometry requires extremely thin beam splitters. Multilayer optics (e.g Mo:Si) have been manufactured to overcome this,

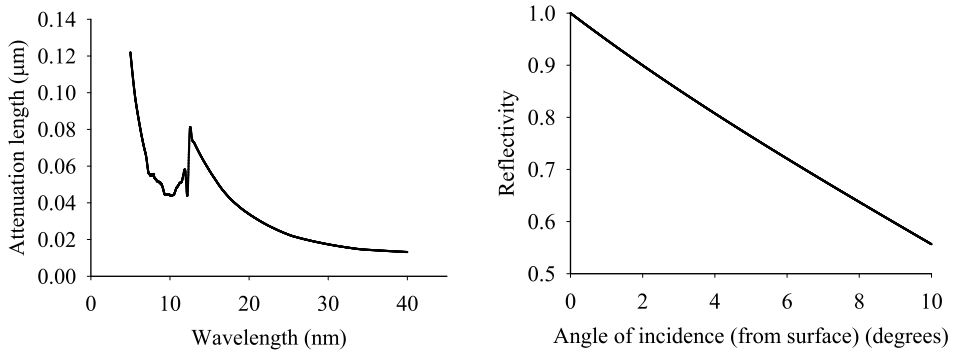

(a) Attenuation (b) Reflectivity

FIGURE 3.7: (a) Attenuation (1/e) lengths for EUV beams in bulk SiO_2 [56] and (b) reflectivity of bulk SiO_2 as a function of incidence angle for a 21.2 nm EUV beam [56].

providing beam splitters with reflectivities of up to $\sim$ 30% and transmittances of up to $\sim$ 20% at 13.5 nm [122]. However, by eliminating the need for beam splitters, as is done in the double Lloyd's interferometer, and taking advantage of the high-reflectivity of bulk materials, such as fused silica or Zerodur ®, at grazing angles, loses can be significantly reduced. This can be seen in the reflectivity of SiO_2 at 21.2 nm for varying grazing angles (figure 3.7 (b)). For the work of this thesis angles of between 6° and 10° have been used, providing reflectivities of between 55% and 70% [56].

Figure 3.8 shows a sample interferogram taken using a double Lloyd's mirror at 21.2 nm, where a laser-plasma has induced a phase and amplitude change in a component of the beams shown in figure 3.6. Another sample interferogram is shown in chapter 6 figure 6.4. Non-uniformities in the EUV laser or the imaged plasma can be seen by the varying intensity of the fringe pattern. However, the beam coherence appears approximately constant across the image and was found to be reproducible, enabling phase shifts maps to be obtained by comparison

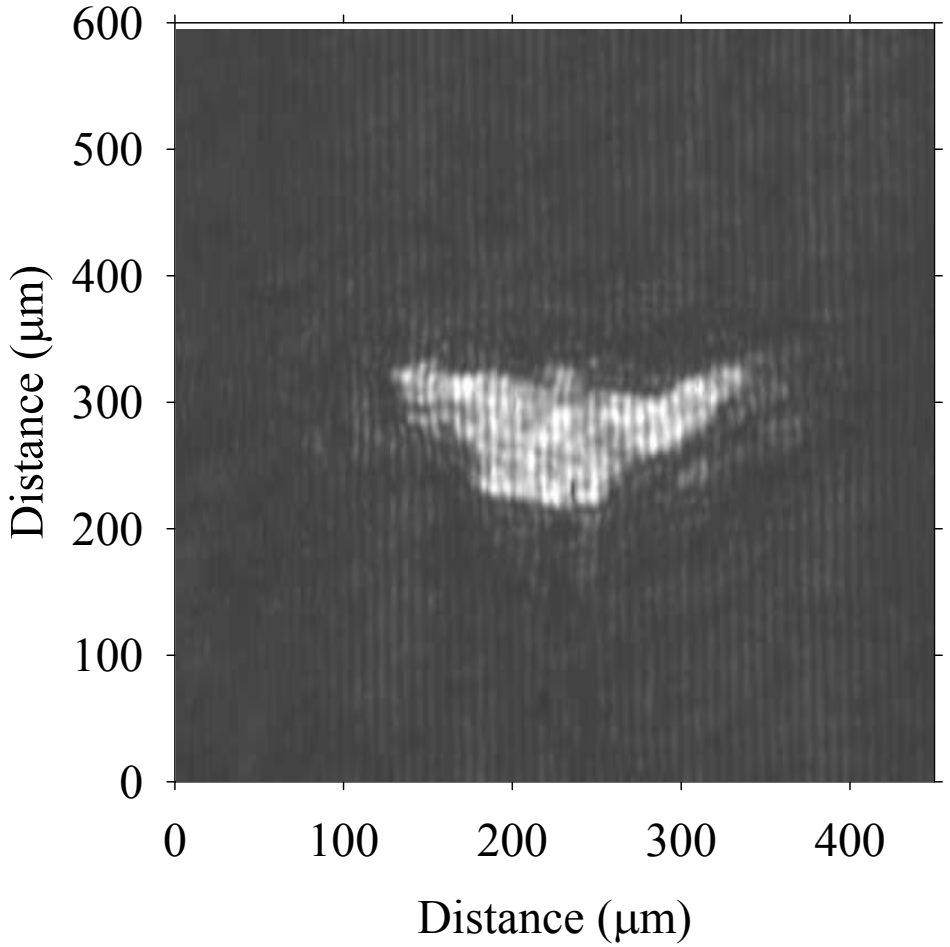

FIGURE 3.8: Interferogram of a laser ablated 200 nm thick CH plastic target taken using the double Lloyd's mirror arrangement 400 ps after the peak of the heating pulse.

with reference interferograms, as discussed below. Chapter 6 details an experiment conducted using the double Lloyd's interferometer to obtain phase shift and transmission data through laser heated parylene-N targets.

3.3.2 Complex interferometry

To allow measurement of small changes in phase shift with interferograms such as figure 3.8, a sensitive technique for analysis is required. Analysis of the interferograms has been conducted using complex interferometry software developed

by M. Kalal and based on algorithms developed by M. Kalal, K.A. Nugent and B. Luther-Davies [123, 124, 125]. Complex interferometry differs from classical interferometry in that not only the phase data, but also amplitude and phase shift time derivative can be extracted from each interferogram simultaneously if required [126]. The basis of this method is in a fully automatic algorithm developed for numerical analysis of the data, using fast Fourier transforms. This allows large quantities of data from two-dimensional interferometry to be analysed [124]. Customised software for interferogram analysis has been developed by M. Kalal and was utilised in this project. The following is a summary of the complex interferometry procedure.

Each data shot comprises a probe and reference beam interference pattern recorded with time averaging over the duration of the EUV probe. The pattern at the plane of interference taken is to be in the (x, y) plane. The intensity of the final interferogram $i(x, y)$ is a superposition of a series of instantaneous interferograms $i(x, y, t)$ taken through the duration of the probe pulse $f(t)$ [125, 126]. Therefore

$$\begin{aligned} i(x,y) &= \int_{-\infty}^{+\infty} i(x,y,t)dt \\ &= \int_{-\infty}^{+\infty} a_0^2 f(t) + \\ &\quad a^2(x,y,t)f(t) + \\ &\quad 2a_0 a(x,y,t)cos[2\pi(\chi_0 x + \psi_0 y) + \varphi(x,y,t)]f(t)dt \end{aligned} \tag{3.2}$$

for reference and probe instantaneous amplitudes a_0 and $a(x, y, t)$ and spatial

frequencies in the x and y directions χ_0 and ψ_0, such that the fringe spatial frequency $f_0 = (\chi_0^2 + \psi_0^2)^{1/2}$ [125, 126]. The phase shift between the reference and probe beams is $\varphi(x, y, t)$ and the temporal profile of the EUV beam is described by $f(t)$, normalised to satisfy the criteria:

$$\int_{-\infty}^{+\infty} f(t)dt = 1; f(t) \geq 0. \tag{3.3}$$

Using the formula $cos\ \theta = (e^{i\theta} + e^{-i\theta})/2$ the expression for the interferogram takes the form

$$\begin{aligned} i(x,y) \;=\; & \int_{-\infty}^{+\infty} a_0^2 f(t) + \\ & a^2(x,y,t)f(t) + \\ & a_0 a(x,y,t) exp[2\pi i(\chi_0 x + \psi_0 y) + i\varphi(x,y,t)]f(t) + \\ & a_0 a(x,y,t) exp[-2\pi i(\chi_0 x + \psi_0 y) - i\varphi(x,y,t)]f(t)dt. \end{aligned} \tag{3.4}$$

The first two terms of equation (3.4) give the instantaneous background of the interferogram $b(x, y, t)$ and the last two terms the superimposed instantaneous fringe visibility $v(x, y, t)$ and its complex conjugate. Equation (3.4) is rewritten as

$$\begin{aligned} i(x,y) \;=\; & \int_{-\infty}^{+\infty} b(x,y,t)f(t) + \\ & v(x,y,t) exp[2\pi i(\chi_0 x + \psi_0 y)]f(t) + \\ & v^*(x,y,t) exp[-2\pi i(\chi_0 x + \psi_0 y)]f(t)dt \end{aligned} \tag{3.5}$$

where $b(x,y,t) = a_0^2 + a^2(x,y,t)$ and $v(x,y,t) = a_0 a(x,y,t) exp[i\varphi(x,y,t)]$ [125, 126].

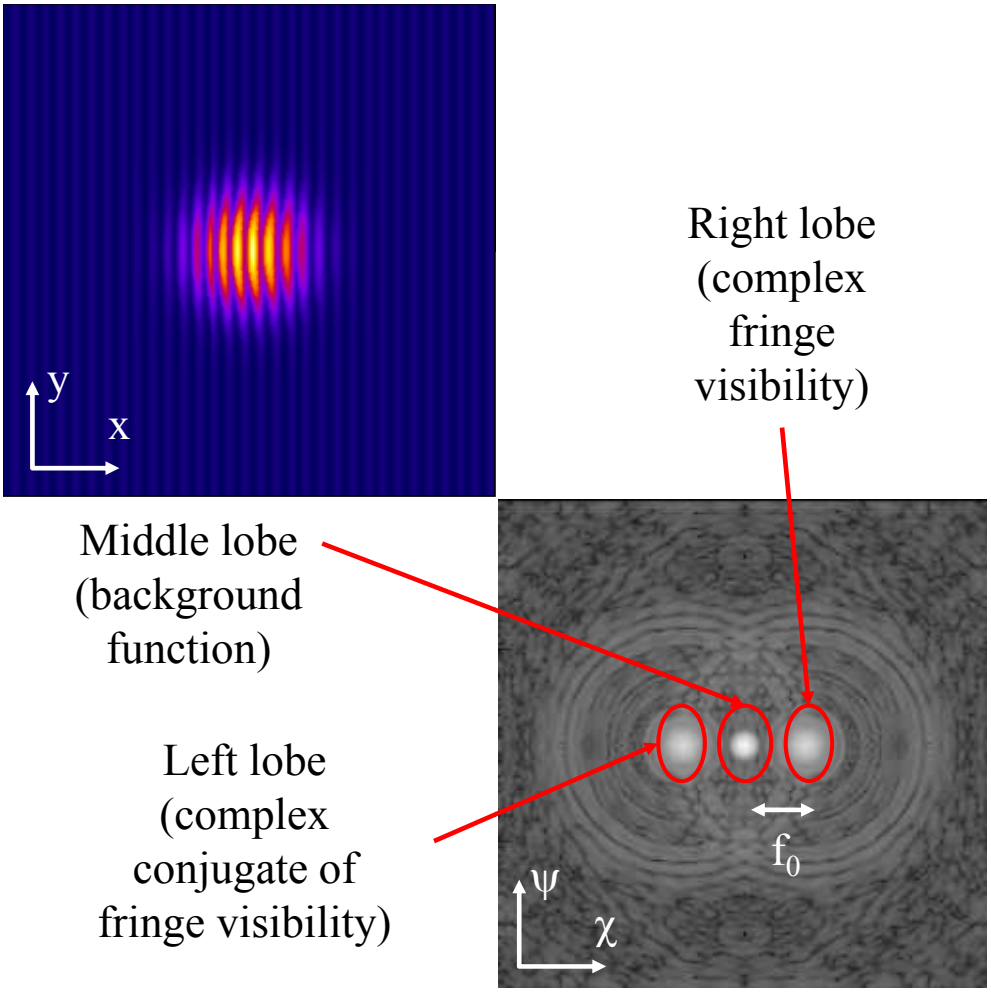

FIGURE 3.9: A simulated interferogram and corresponding Fourier transform spectrum. Labelled are the lobes selected to obtain the required quantities from the image [125, 126]

A Fourier transform of the interferogram converts the image in the (x,y) plane to the (χ,ψ) plane. A simulated interferogram and corresponding Fourier transform are shown in figure 3.9 where three lobes can be seen, with separation in frequency space of f_0. The separation arises due to the slow spatial variations of the background compared with the fringes. The intensity I in frequency space is described

analytically by

$$I(\chi,\psi) = B(\chi,\psi) + V(\chi-\chi_0,\psi-\psi_0) + V^*(\chi+\chi_0,\psi+\psi_0) \tag{3.6}$$

with background $B(\chi,\psi)$ and visibility $V(\chi,\psi)$ intensities denoting the Fourier transforms of the functions $b(x,y)$ and $v(x,y)$ [123].

In frequency space, it is possible to select a lobe corresponding to V or V^* (as shown in figure 3.10). The part of the spectrum outside of this area is set to zero, removing the unwanted background irradiance variations with spacing significantly different to the fringe spacing [127]. The area is then shifted to the central part of the spectral plane and then by performing the inverse Fourier transform the visibility $v(x,y,t)$ is obtained. The contribution of the background variation has been eliminated from the subsequent reconstruction [125]. The background function $b(x,y,t)$ can be similarly obtained from the middle lobe of the Fourier transform (see figure 3.10).

As it is the time-averaged rather than instantaneous quantities that are recorded over the duration of the EUV probe, $b(x,y,t)$ and $v(x,y,t)$ are replaced by $\bar{b}_0(x,y)$ and $\bar{v}_0(x,y)$, the normalised quantities, corresponding to the centre of the EUV pulse $f(t)$ [126]. Signal free regions of the interferogram are selected during processing, to enable normalisation, through which the background amplitude is set to 1. From $\bar{b}_0(x,y)$ and $\bar{v}_0(x,y)$ the phase shift $\varphi_0(x,y)$ and normalised amplitude

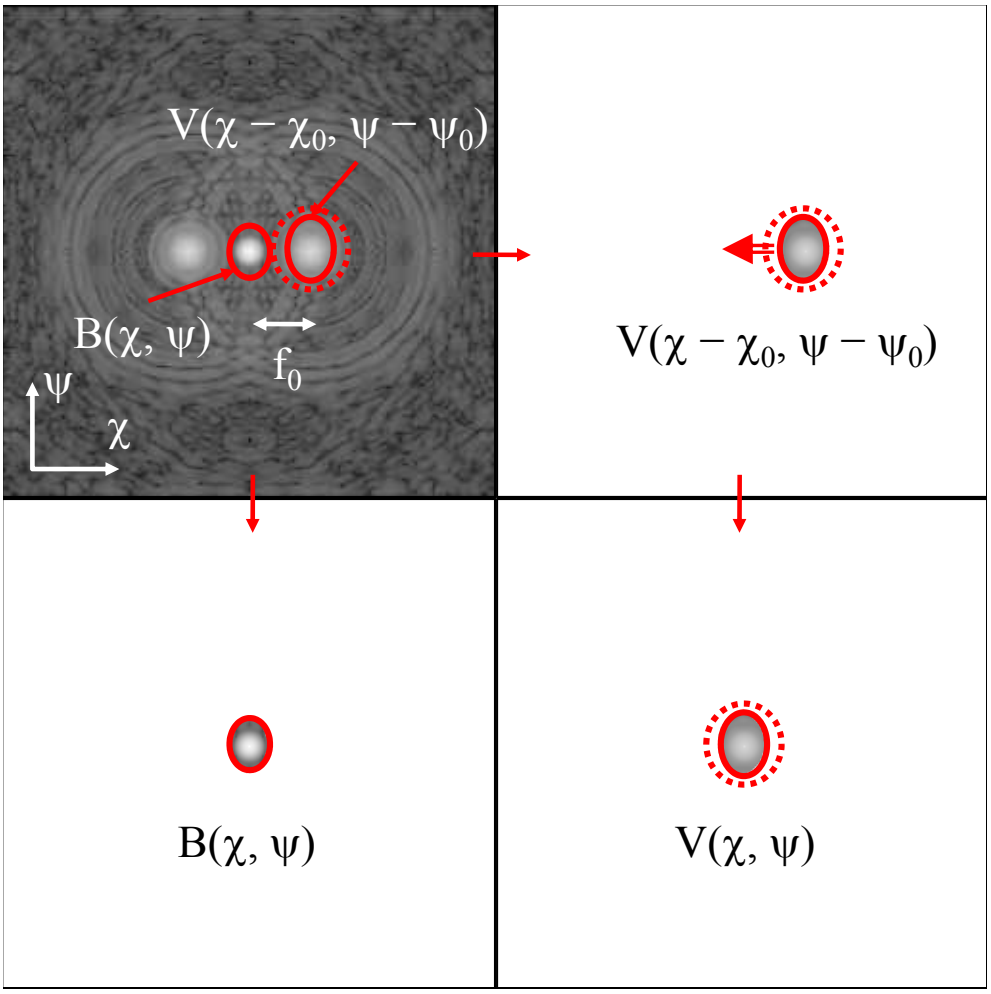

FIGURE 3.10: Illustration of the complex interferometry technique of spatial filtering [125, 126, 127]. Shown is the Fourier transform from figure 3.9 with selection of the middle or right lobes depicted, as described in the text. The dashed circle indicates a larger selection of the spectral plane being taken, where fewer frequencies are neglected, resulting in finer variations in the resulting phase map.

$\bar{a}_0(x, y)$ can be found [126] with

$$\varphi_0(x, y) = \Im[ln\bar{v}_0(x, y)], \tag{3.7}$$

$$\bar{a}_0(x, y) = \sqrt{2\bar{b}_0(x, y) - 1}. \tag{3.8}$$

Amplitude and phase shift maps constructed through analysis of the interferogram

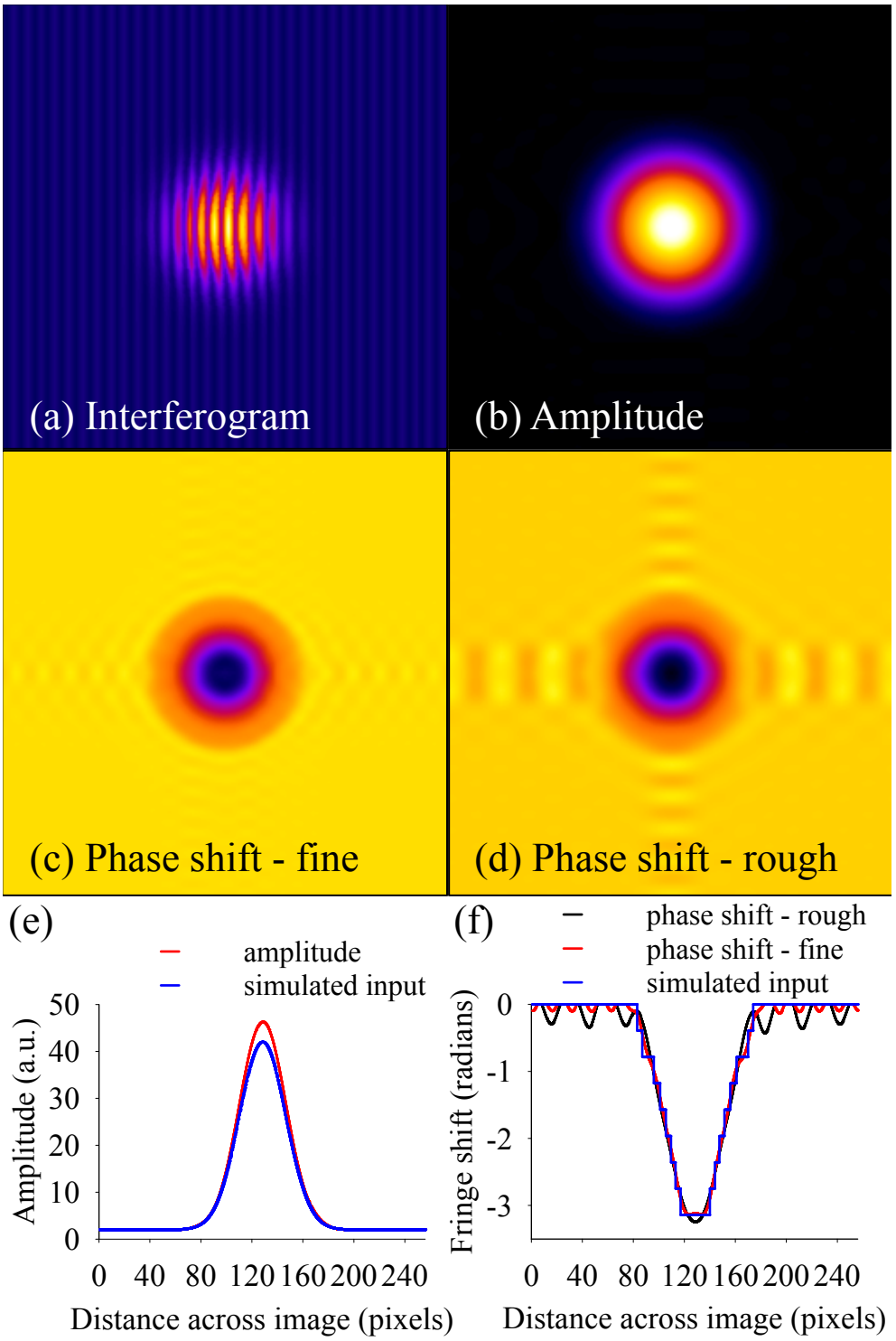

FIGURE 3.11: An interferogram, (a), with corresponding amplitude, (b), and phase shift, (c), maps. Also shown the resultant image from greater spatial filtering, (d), and profile comparisons of the simulated input and reconstructed amplitude and phase shift, (e) and (f).

of figure 3.9 are shown in figure 3.11. Both amplitude and phase shift reconstruction show agreement to the simulated input, shown as profiles across the centre

of each image in figure 3.11 (e) and (f). By altering the area of the lobe selected on the Fourier transform (see the dashed circle in figure 3.10) more (fine) or less (rough) spatial frequencies are included. This determines the level of detail on the resultant image (see figure 3.11 (c) and (d)) and needs to be set so that random noise is removed. Errors arise due to the finite sampling interval in frequency space [125], demonstrated by the greater agreement between input and reconstruction where more spatial frequencies are included (see figure 3.11 (f) comparing the simulated input (blue line) to the phase shift reconstructed with fine (red line) and rough (black line) detail). Given a high enough fringe spatial frequency f_0 there will be negligible overlap between the shifted functions B, V and V^* so that the lobes can be easily distinguished, and the background variations removed.

Moving away from the idealised example given above, real interferograms will be subject to noise over the image, from intensity variations across the backlighting source and from the recording device. The demonstrative analysis of the simulated interferogram has been repeated with the addition of a random noise pattern and a pattern of EUV backlighter amplitude variation, taken from experimental measurement. The resulting phase shift maps and profiles are presented in figure 3.12 where the effect on phase shift reconstruction can be seen, with the greater deviations arising from the experimental noise pattern (figure 3.12 (c)).

Noise from intensity variations across the backlighting source and from the CCD detector will introduce error into the experimental technique. To increase accuracy a second, auxilliary data shot is taken (prior to the shot with the ablating beam) and used to calculate the normalised visibility function $\bar{v}_0(x, y)$ at the centre of

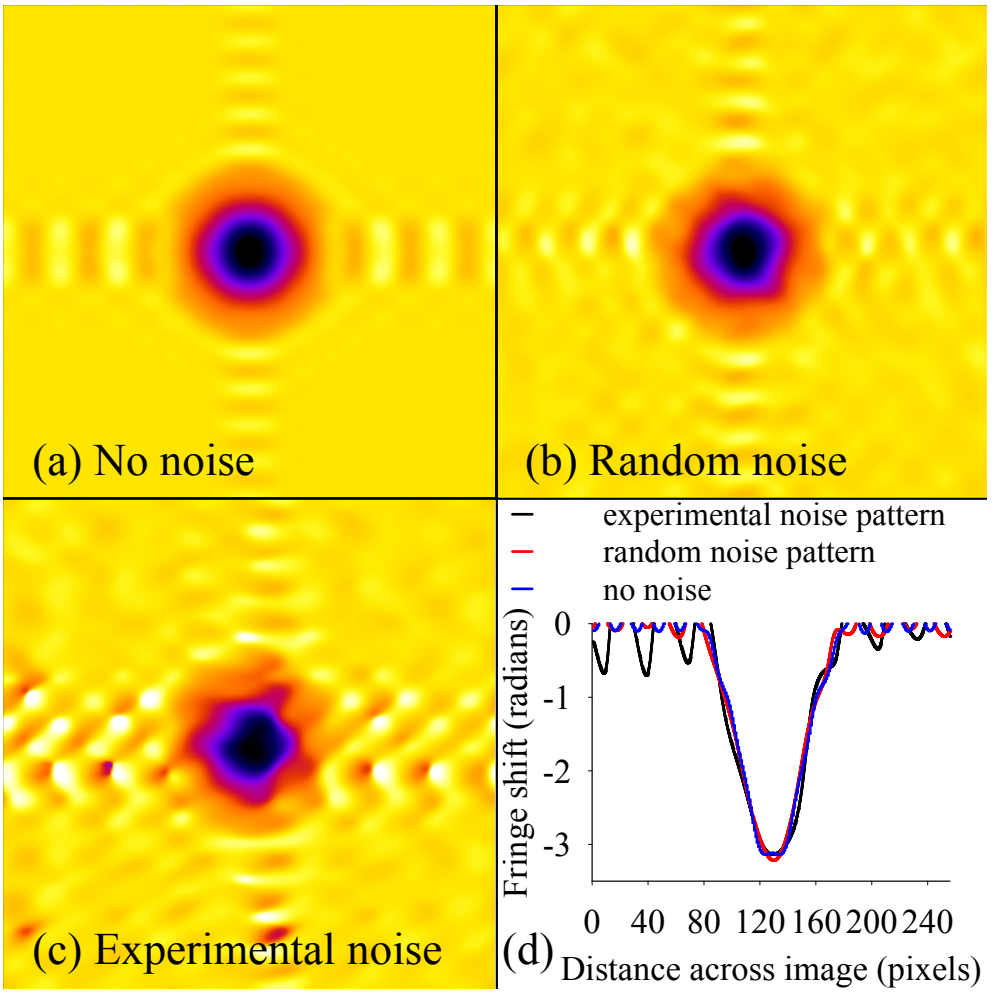

FIGURE 3.12: Phase shift maps reconstructed from simulated interferograms with no noise (a), random noise (b) and experimental amplitude variation noise (c) superimposed. Profile comparisons across the images in part (a), (b) and (c) are given in part (d).

the EUV pulse $f(t)$, where the probed target is now stationary. The background function is normalised to $\bar{b}_0(x, y)$ by selecting signal free regions of the data shot. The resulting phase shifts and amplitudes are then produced as in figure 3.11. A caveat of this is that the algorithm used cannot return phase shift values outside of the interval $-\pi$ to π. Additional programming is included for removing the artificial jumps that arise from larger phase shifts [126].

The technique of complex interferometry improves the accuracy of fringe shift and transmission measurements by effectively spatially averaging over a chosen area

so that noise at frequencies different to the fringe spatial frequency is removed and by selecting signal free regions to remove systematic noise (present across the interferogram). The interferometer reduction procedure is described more fully in the references [123, 124, 125, 126, 127]. Use of this diagnostic to study the region of warm dense matter, between the critical and ablation surfaces of a laser heated plasma, is presented in chapter 6.

Summary

Three diagnostics used in this work have been described, including use of a double Lloyd's mirror and flat field spectrometer for EUV probing of laser-plasmas and a crossed slit camera for monitoring the line focus of an EUV source. Complex interferometry has been shown to be a valuable tool in plasma characterisation. In chapter 6 this is applied to interpret the interferometry of warm dense matter.

Chapter 4

Simulation codes

The following chapters include simulation results obtained using the two-dimensional codes POLLUX [49] and h2d [22]. Within this chapter the physical processes which form the basis of each code are explained. A post processor to calculate EUV transmissions from code generated data, created as part of this work, is then described.

Both the POLLUX and h2d codes are based on hydrodynamic (fluid) models capable of simulating laser-plasma interactions and determining average macroscopic quantities, such as density and temperature. Initial values and boundary conditions are expressed in an input file, which are then advanced over time steps using the governing equations. The core equations of mass, momentum and energy

conservation are supplemented by models of radiation transport, electron and ion transport, ionisation and others, closed by the equation of state employed.

4.1 POLLUX

The 2D Eulerian hydrodynamic code, POLLUX [49], created by G. Pert and later modified by R. Taylor, J. Edwards and R. Evans, has been used to model laser ablation and other laser-plasma phenomena [128, 129, 130, 131, 132]. Utilising planar or cylindrical Eulerian y, z geometry in two dimensions, POLLUX allows simulation of high-intensity ($> 10^9$ W cm^{-2}) laser irradiation of a solid target in a spot focus [128]. As a Eulerian code mass flows between the cells, which remain stationary, facilitating tracking of areal density variations indicative of the Rayleigh-Taylor instability (see section 5.1).

Formation of a two temperature plasma is modelled with separate electron and ion temperature and with laser energy absorption by inverse bremsstrahlung up to the region of critical density within the expanding plasma. At the critical density the energy is assumed to be absorbed at a rate of 20% for the work of this thesis, and 80% reflected [129]. The deposited energy is transported beyond the critical region by electron thermal conduction and distributed partly to the ions by electron-ion collisions [49, 128]. Within POLLUX a perfect gas equation of state is used to close the system.

As is common in such codes, the presence of steep temperature gradients, particularly at the critical region, leads to an overestimation of the energy transport by

electrons. The classical Spitzer-Harm theory of thermal conductivity was derived assuming small temperature gradients with an upper limit to the heat flow given by $Q_{max} \propto N_e T_e (T_e/m_e)^{1/2}$ for electron density, temperature and mass N_e, T_e and m_e and with the constant of proportionality taken to be approximately 0.6 [133]. The electron velocities are described by the Maxwell-Boltzmann distribution, which peaks at the thermal velocity. The fast electrons towards the tail of the distribution, where the heat flow approaches Q_{max}, increase the average electron mean free path ($1/(N_e\ \sigma_{\text{collision}})$, for collisional cross-section $\sigma_{\text{collisional}}$), to distances greater than the scale length ($T_e/\nabla T_e$). This can result in thermal energy being transported as fast as in vacuum.

To mitigate this, and take into account the majority thermal electrons, a flux limiter is applied when calculating thermal conduction. The flux limiter is chosen to match experimental electron energy transport and many studies have been performed to better determine suitable values (typically 0.01 - 0.1 [51, 133, 134, 135, 136, 137]).

Inclusion of opacity data into the code allows calculation of the transmission of EUV and x-ray radiation through the code predicted densities and temperatures. IMP opacity files [106] are used in the model to calculated the transmissions directly, for longitudinal probing. Results from the code are presented in chapter 5, showing laser modulation patterns, simulating target and/or laser imperfections that lead to Rayleigh-Taylor instability formation. As a flow dominated process RTI is suitable for study with hydrodynamic codes [83]. A sample input file, where the Eulerian grid is defined, is given in appendix A.

4.2 H2d

The radiation hydrodynamic code h2d, written by J. Larsen [22], enables 2D modelling of the macroscopic properties of a plasma in the presence of a radiation field with incident intense optical laser radiation [89, 138, 139, 140, 141]. A Lagrangian coordinate system in r, z cylindrical geometry is used with the 'z' axis as the axis of symmetry in the axial direction, and the 'r' axis being orthogonal in the radial direction. A computational mesh, or grid, is established, defining quadrilateral zones, or cells, with the motion of the vertices obeying the law of conservation of momentum. As a Lagrangian coordinate system is in use, the mass in a zone is automatically conserved. However, mesh distortions arising from nonuniform pressures or shear forces can result in mesh point crossings, where zones must be redefined in order to continue with the simulation. Artificial pressures and viscosities, as well as surface tension forces, are included to resist distortion of the mesh and prevent mesh point crossings, without violating the conservation of momentum [22]. By choosing the h2d simulation code, based on a Lagrangian coordinate system, it has been possible to simulate laser ablation of multi-layer targets in vacuum for direct comparison with experiment.

Within each zone three fluids are considered; free electrons, massive particles (ions and neutral atoms) and the radiation field. The electron and ion fluids are treated separately with interactions via Coulomb collisions. This interaction is based on a collisional model with the electron-ion collision rate being modified to include electron degeneracy. Each of the three fluids is in thermodynamic equilibrium, described by the Maxwell-Boltzmann distribution. The code includes flux-limited

energy transport in the direction of the density gradient, to mitigate overestimation of the penetration of thermal energy into cold material [22]. The modelling of the radiation field is facilitated by division of the photon energy spectrum into a finite number of groups. All photons that fall within a group are treated the same, leading to group-averaged absorption coefficients [22].

Four models are available to calculate the degree of ionisation in the plasma: a Saha model, Thomas-Fermi model, LTE 'average atom' model or an assumption of fully stripped ions. The material species, density and electron and radiation temperatures are used to calculate the ionisation for the first three of these models. The LTE 'average atom' model is used in this work. A single average ionisation state is assumed, in which it is not necessary to have an integer number of bound electrons for each level, rather a Maxwellian distribution over the discrete energy levels is used. In particular this is applicable where electron-ion collision rates are fast enough to dominate the photon field, such as in the warm, dense matter regime. In the limit of a high-temperature, low-density plasma the LTE 'average atom' results are identical with the Saha model [22].

Within h2d the temperature and mass density are treated as independent variables. The dependent variables are the pressure and specific energy, from which the sound speed, specific heat capacity and thermal conductivities are calculated. To calculate changes in internal energy, within h2d, detailed information about the specific heats of each material are needed. Likewise, accurate determination of the hydrodynamic response of a plasma relies on a reliable model of the pressure [22]. H2d does not calculate equation of state (EOS) data and requires externally

generated EOS packages. For this work the SESAME EOS package [142] was used, which is a computer-based library of tables giving the thermodynamic properties of materials.

During laser-plasma interactions h2d assumes that electron energy absorption is by inverse bremsstrahlung up to the critical density, at which point an energy dump or model of resonance absorption can be called. A ray trace algorithm included in the code maps the incoming laser beam trajectory for a set of rays determined by user input. This method is based upon geometrical optics and ignores wave effects in the laser interaction. The laser source is further specified by its power, frequency and temporal profile. Each ray is defined by passing through a reference point in the model in a specified direction, with a fraction of the total laser power. The plasma index of refraction η_{plasma} is calculated to modify the direction of the ray by refraction as it passes between zones, with equation (2.11)

$$\eta_{\text{plasma}} = (1 - \frac{N_e}{N_{\text{crit}}})^{\frac{1}{2}}$$

for electron density N_e and critical density N_{crit}. The electron density determines the resultant laser absorption within each zone.

Each of the specified rays that make up the incident laser will pass through the mesh, following the laws of geometrical optics. Whether or not the ray passes straight through a zone or is deflected, is determined by the angle of incidence and the electron density gradients. 'Turning points' signify deflections of the ray from a straight line path. From any given position a ray may cross between zones or

hit a turning point in a given amount of time. If the time taken to reach the next turning point is greater than the time taken to cross into an adjoining zone then absorption by inverse bremsstrahlung occurs within that zone. If the converse is true an energy dump or resonance absorption will occur within the zone [22].

After completion of the simulation, the flow properties, including density, temperature and ionisation, are extracted for each zone within the mesh. Results from h2d simulation of laser ablation are presented in chapters 5 and 6. An annotated sample input file is given in appendix B.

4.3 Post-processor for calculating transmission data from POLLUX and h2d simulations

Through the use of the simulation codes described above, vast amounts of data can be produced, describing the evolution of laser-plasmas. Within the work of this thesis, the transmission of EUV wavelength radiation has been used to diagnose warm, dense plasmas, therefore it was necessary to be able to calculate transmissions from simulated data for comparison.

To assist in this a post-processor has been developed to calculate the transmission of EUV rays and other radiation through simulated plasmas, using theoretical opacity codes (see section 2.2). Multigroup opacities, with temperature and density dependence, are first selected for groups either side of the required probe energy, or frequency. By interpolation a set of values for opacity at the probe

photon energy are then calculated, typically with 19 temperature steps between 5 and 200 eV and 9 density steps between 0.001 and 10 g cm^{-3}. Room temperature opacity data from published literature [56] is used to provide the low-temperature limit for the opacity data set. The POLLUX (or h2d) simulated temperatures and densities are output and a value of opacity for each cell (or zone) is calculated, with linear interpolation between the discrete values at particular temperatures and densities in the above opacity datasets.

The transmission T through each cell was given by equation (2.5):

$$\frac{I}{I_0} = T = exp(-\sigma_s\ \rho\ z)$$

where I and I_0 are the transmitted and incident probe intensities, σ_s is the specific absorption coefficient (opacity), ρ is the mass density and z is the cell thickness in the direction of probing. Using equation (2.5) the transmission is calculated for each cell. The total transmission through the target is obtained by multiplying the relevant transmissions T through all cells axially.

Summary

By efficiently post processing the large volumes of code generated data it has been possible to obtain simulated values of EUV transmission and phase shift, for direct comparison with experimental work and to further the understanding of laser-plasma interactions. The simulation codes presented in this chapter have been used to model the imprint of laser modulation in Rayleigh-Taylor instability

formation (section 5.1), x-ray backlighting of an iron layer (section 5.2), heating of buried layer iron opacity targets (section 5.3) and the transmission and phase shift for laser heated plastic targets (chapter 6).

Chapter 5

EUV probing of the Rayleigh-Taylor instability and iron opacity

The two-dimensional simulation codes POLLUX and h2d have been used to model laser ablation diagnosed with EUV and x-ray radiation for three studies detailed within this chapter. A version of the POLLUX code, customised for studies of instability growth, has been used to investigate the Rayleigh-Taylor instability (RTI). H2d has been used to study the laser irradiation of multilayer targets of iron, plastic and aluminium and, with inclusion of theoretical opacity codes, to determine transmissions through iron of 18 - 22 nm wavelength radiation for

comparison with experiment. In addition to those previously mentioned, the use of an x-ray backlighter at photon energy 1.5 keV as a probe of iron when heated by laser irradiation is also simulated and shown to be a useful diagnostic technique.

5.1 POLLUX in modelling Rayleigh-Taylor instabilities

The application of EUV backlighters to the probing of RTI growth on planar targets has been investigated using the two-dimensional hydrodynamic code POLLUX, introduced in chapter 4. The motivation for studies of RTI is laid out in section 2.1, with emphasis on optimising the compression of inertial fusion targets.

To investigate the effect of RTI growth on CH plastic, a proposed shell material for DT fuel pellets in ICF, a carbon target was irradiated normally by a laser pulse of peak irradiance 5×10^{14} W cm^{-2} and wavelength 0.35 μm, parameters applicable to ICF pellet compression [75]. These experimental conditions are simulated here, but with the RTI artificially seeded by assuming spatial perturbations in laser intensity.

5.1.1 Simulation parameters

Simulations were carried out in planar geometry for small (10 μm width) and large (100 μm width) carbon targets assuming irradiation focal diameters much greater than the target size. A 10 μm thick target of solid state density was

assumed embedded in an Eulerian mesh containing a low-ambient-density plasma (3×10^{-6} g cm^{-3}). Spatial perturbations in laser intensity have been used to seed the RTI with a sinusoidal modulation pattern of the laser irradiance imposed in the lateral direction with modulation wavelengths ranging from 100 μm to 1 μm. The incident irradiance was assumed to be temporally flat-top with a duration of 1 ns, peaking at 5×10^{14} W cm^{-2} with a linear intensity ramp of duration 250 ps. An electron flux limiter of 0.06 was selected, found to be appropriate for the chosen irradiance [51, 134]. EUV transmissions were calculated using CH plastic IMP opacities [106] for an extended source of photon energy of 90 - 100 eV.

5.1.2 Simulation results and discussion

Figure 5.1 shows mass density contours for 100 μm wide targets 500 ps and 1 ns from the onset of laser irradiation. Simulation of a modulation wavelength of 100 μm is depicted in figure 5.1 (a) and (c) and 25 μm in figure 5.1 (b) and (d).

For both modulation wavelengths the imprint of the laser pattern can be clearly seen. At later time, comparing figure 5.1 (a) to (c) and (b) to (d) the imprint no longer appears sinusoidal. To further study the evolution of this imprint and how it exhibits itself on smaller scales, lateral transmission profiles of EUV probe radiation were extracted from simulation for each modulation wavelength at 500 ps and 1 ns from the onset of laser irradiation. Figures 5.2 and 5.3 show simulated transmission profiles for a 100 μm target under varying laser irradiance patterns at 500 ps and 1 ns respectively. Profiles for the smaller, 10 μm target are shown in figure 5.4.

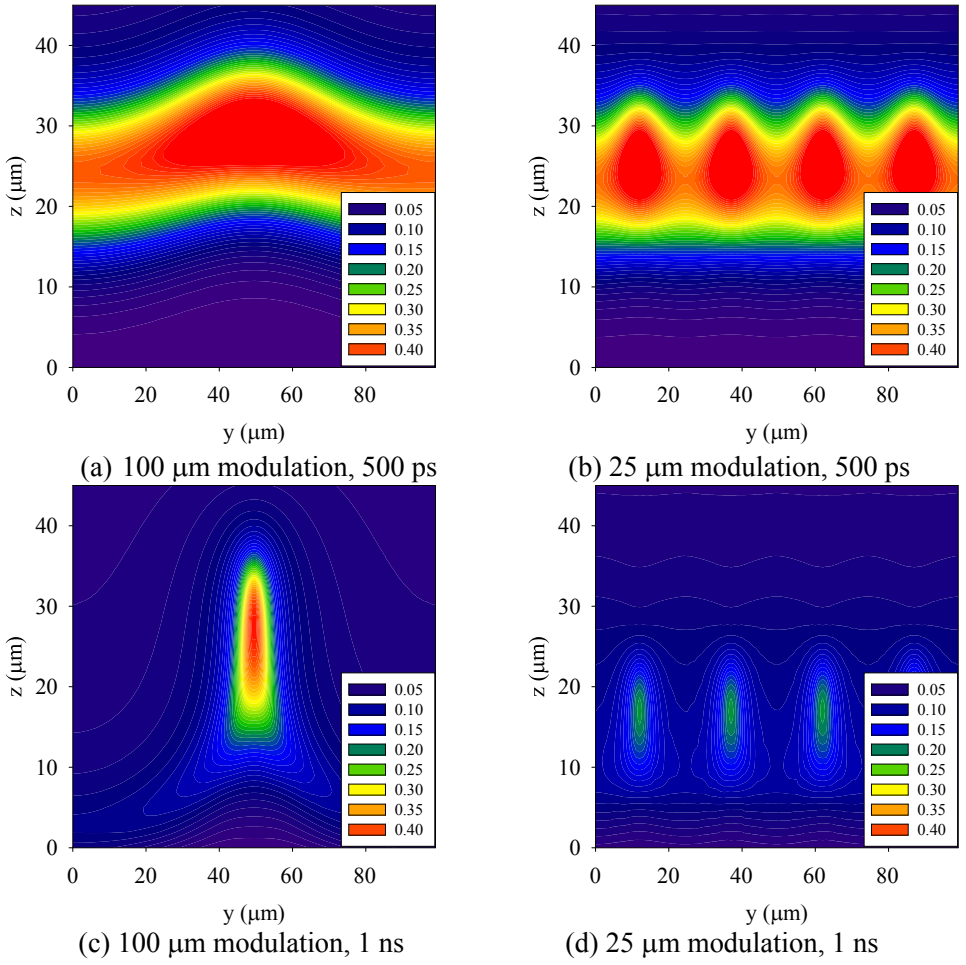

FIGURE 5.1: POLLUX simulated mass density contours for an ablated planar target under a modulated laser irradiance. The target size is 100 μm laterally (in y) and the modulation wavelength is (a) 100 μm at 500 ps, (b) 25 μm at 500 ps, (c) 100 μm at 1 ns and (d) 25 μm at 1 ns. The original target thickness is 10 μm (in z). The laser is incident normally in the negative z direction. The colour scale shows mass density in g cm^{-3} (as labelled).

EUV probing can produce high-visibility transmissions for plasmas irradiated by modulated intensity variations, as can be seen in figures 5.2 and 5.3. The sinusoidal modulation pattern used to seed the instability is distinct in figure 5.2 at an early time. As the instability develops the transmission profile changes, indicating a change in opacity σ_s and/or areal density ρz of the ablating plasma.

In contrast to figure 5.2 lateral transmission profiles for the smaller, 10 μm target (see figure 5.4) show reduced signs of the modulated laser imprint, even though

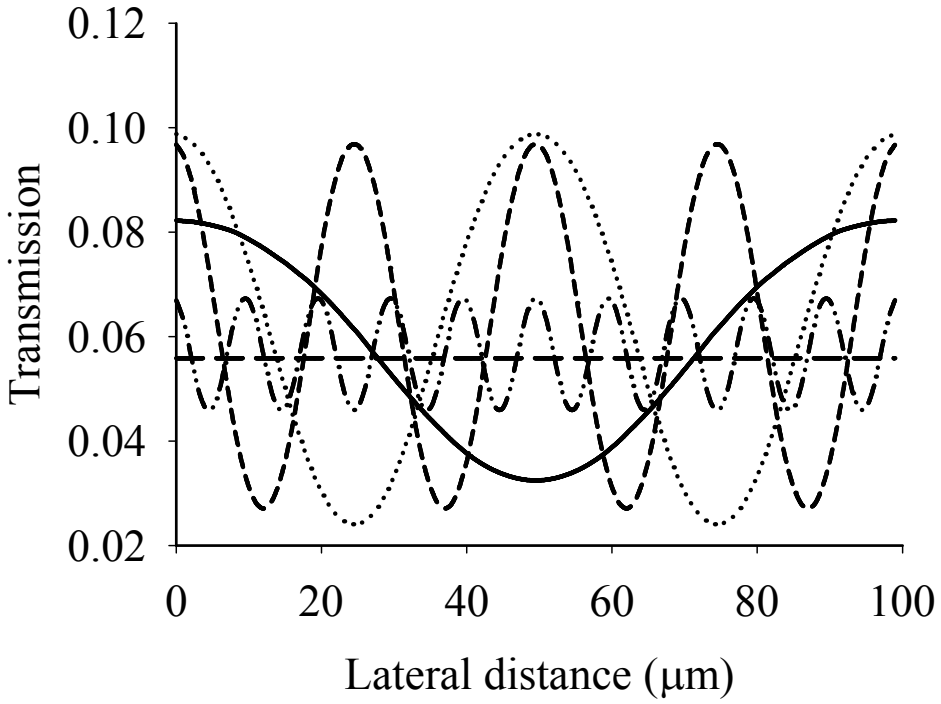

FIGURE 5.2: POLLUX simulated lateral transmissions of a 90 - 100 eV probe 500 ps from the onset of laser irradiation. Recall simulations conducted in planar geometry. Simulations are for a 100 μm target with the following modulation wavelengths: 100 μm (solid line), 50 μm (dotted line), 25 μm (short dashed line), 10 μm (dot-dashed line) and no modulation (long dashed line).

identical modulation amplitudes were simulated. Owing to lateral transport of material, the modulation pattern has been smoothed out. This demonstrates wavelength dependent dampening of instability inducing perturbations, as predicted by the Takabe equation for instability growth (equation (2.4) [81], section 2.1.1.1). Shorter wavelength perturbations experience greater dampening due to lateral material flow, resulting in the smoothed modulation pattern of figure 5.4.

To understand how EUV probing can be used to diagnose RTI, is it necessary to

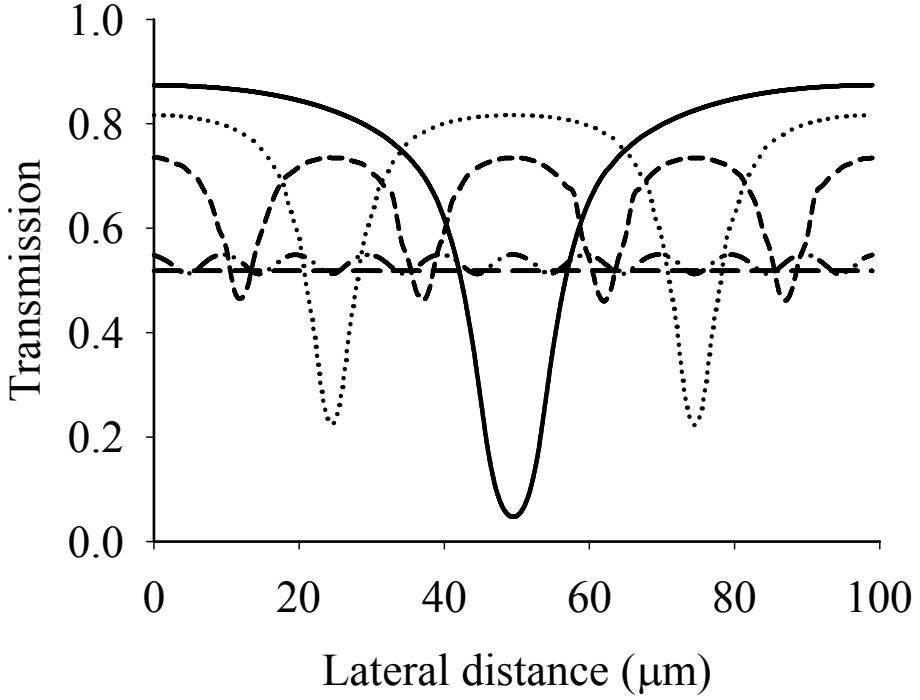

FIGURE 5.3: As figure 5.2, 1 ns from the onset of laser irradiation.

determine where in the target absorption is taking place. Through use of the post processor described in chapter 4, axial transmission profiles were obtained from POLLUX simulated data. IMP opacities [106] for a 90 - 100 eV probe energy were again selected. Figure 5.5 shows axial transmission profiles for an initially 10 μm thick target, illuminated without modulation of the irradiating laser.

Superimposed on figure 5.5 are density and opacity profiles at 500 ps (a) and 1 ns (b) from the onset of the irradiating laser. The steepest gradient in transmission corresponds to the strongest region of absorption. The opacity peaks for the solid density, low-temperature material. As the target material is ablated, the opacity

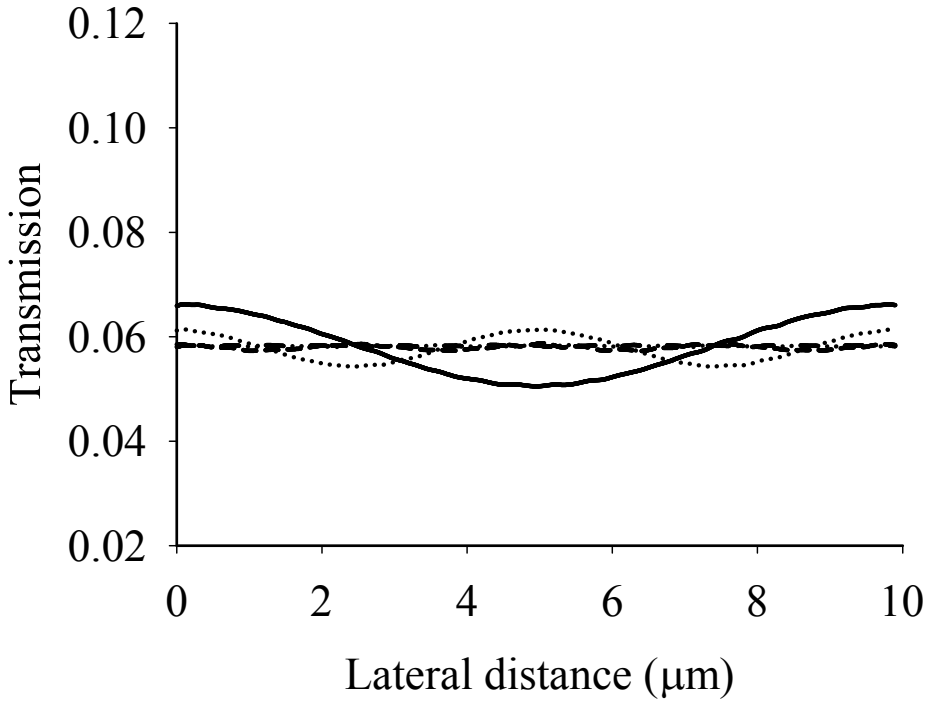

FIGURE 5.4: POLLUX simulated lateral transmissions for a 10 μm target 500 ps from the onset of laser irradiation. The following modulation wavelengths are shown: 10 μm (solid line), 5 μm (dotted line), 2.5 μm (short dashed line) and 1 μm (dot-dashed line). The transmission is presented on the same scale as figure 5.2 for comparison.

rapidly drops. At such times the transmission of the remaining solid target is measured with longitudinal probing [5, 46, 47]. Consequently the regions of peak density dominate the absorption. However, as can be seen from figure 5.5 (a) and (b) the opacity is not solely density dependent (see also figure 2.8).

In order to investigate smoothing of the RTI growth imprinted by the laser irradiance variation, and dependence on opacity, the change in areal density ρz has been explored. EUV probing was applied to experimental studies of the RTI in the mid

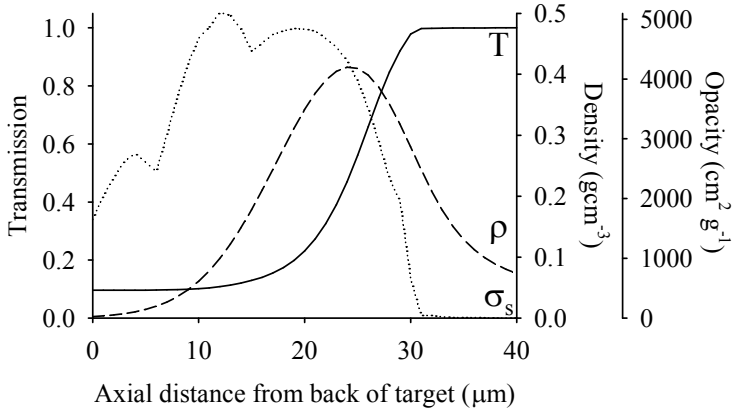

(a)

Transmission, density and opacity
500 ps from the onset of irradiance

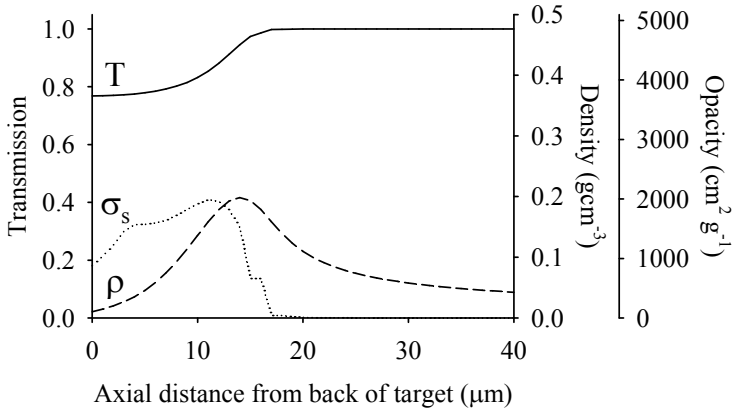

(b)

Transmission, density and opacity
1ns from the onset of irradiance

FIGURE 5.5: POLLUX simulated axial transmission profiles of 95 eV radiation as a function of distance from the back side of the target (solid curve) for an ablated planar target at 500 ps (a) and 1 ns (b) from the onset of laser irradiation. Also shown are the corresponding density (dashed line) and opacity (dotted line) profiles taken from POLLUX simulation and IMP opacities [106].

to late 1990s [45, 46, 47, 48, 83, 84]. Values for rms areal density amplitude $\Delta\rho z$ were calculated from the EUV transmissions taken from longitudinal radiography [47] with

$$(\rho z)_{\max} - (\rho z)_{\min} = ln\left(\frac{I_{\min}}{I_{\max}}\right)\frac{1}{\sigma_s} = 2.86\Delta\rho z \tag{5.1}$$

given by the maximum and minimum intensity $I_{\max}$ and $I_{\min}$ and opacity σ_s [48]. The 2.86 factor arises in conversion to the rms value from the maximum value of the sinusoidal modulation pattern [48]. Figures 5.6 and 5.7 show the evolution of the target-average rms areal density ($\Delta\rho z/\rho z$), generated directly by the POLLUX code.

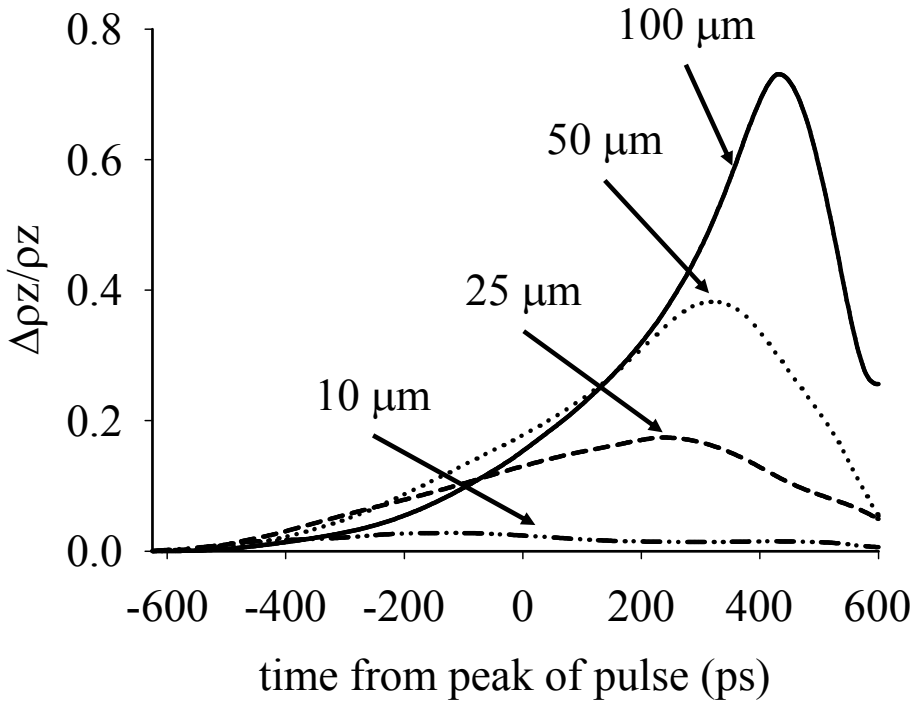

FIGURE 5.6: POLLUX simulated target-average rms areal density for a 100 μm target. The following modulation wavelengths are shown: 100 μm (solid line), 50 μm (dotted line), 25 μm (short dashed line) and 10 μm (dot-dashed line).

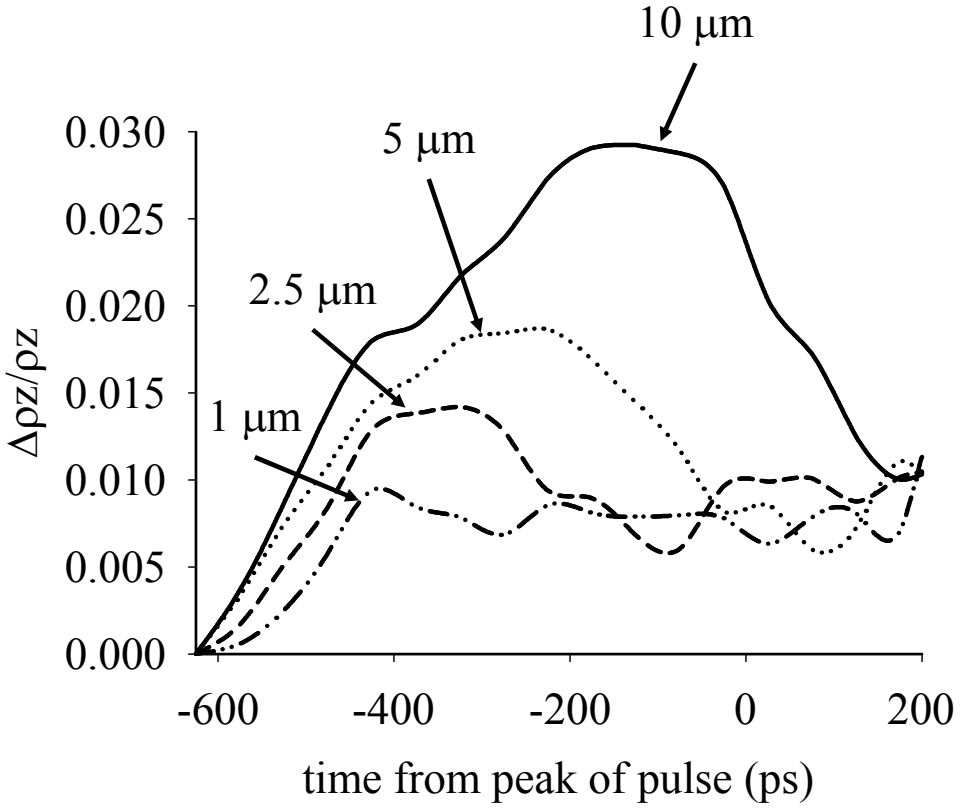

FIGURE 5.7: POLLUX simulated target-average rms areal density for a 10 μm target. The following modulation wavelengths are shown: 10 μm (solid line), 5 μm (dotted line), 2.5 μm (short dashed line) and 1 μm (dot-dashed line).

For both target sizes the rms areal density $\Delta\rho z/\rho z$, and therefore instability, grows in time under a modulated irradiance, demonstrating a departure from a 1D expansion (when the laser irradiance has no modulation and $\Delta\rho z/\rho z \equiv 0$). Increased smoothing for shorter wavelength perturbations is indicated by differences in height and position of the peak rms areal densities between figures 5.6 and 5.7. Shorter wavelength modulations are smoothed more rapidly (the peak is earlier in the simulation) and larger instabilities can grow under longer wavelength modulations (the peak is higher).

Equation (5.1) has been used to calculate the rms areal density $\Delta\rho z/\rho z$ from POLLUX simulated target-averaged maximum and minimum transmissions, which

can then be compared to POLLUX code generated values. In the calculation the solid, room temperature value for opacity σ_s [56] is assumed, as was done by [5, 46, 47]. In figures 5.8 and 5.9 the target-average rms areal densities from the calculation, using equation (5.1), and those computed directly by the POLLUX code, i.e. from the actual changes in areal density, are compared.

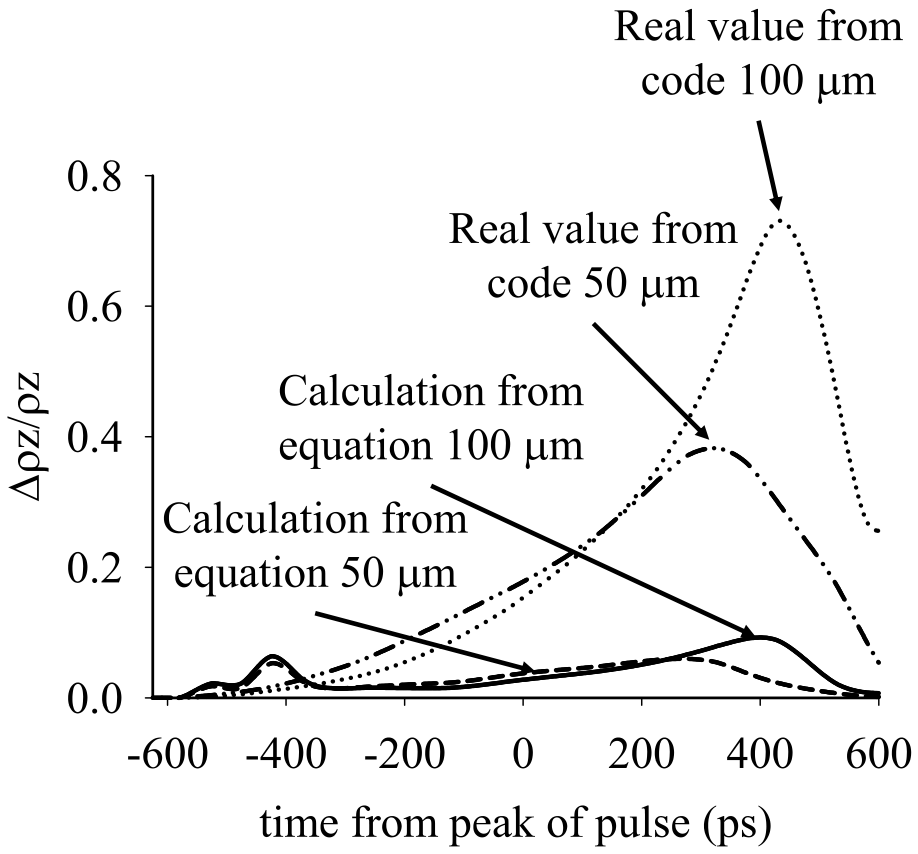

FIGURE 5.8: Comparison of simulated target-average rms areal density for a 100 μm target from calculation (using equation (5.1)) and generated directly by the POLLUX code. The following modulation wavelengths are shown: calculation 100 μm (solid line), real value from code 100 μm (dotted line), calculation 50 μm (short dashed line) and real value from code 50 μm (dot-dashed line).

The 100 μm target (figure 5.8) and 10 μm target (figure 5.9) both show the calculated values peaking early and then decreasing, as expected due to lateral transport of material and the resultant smoothing. This is predicted to occur $>$ 200

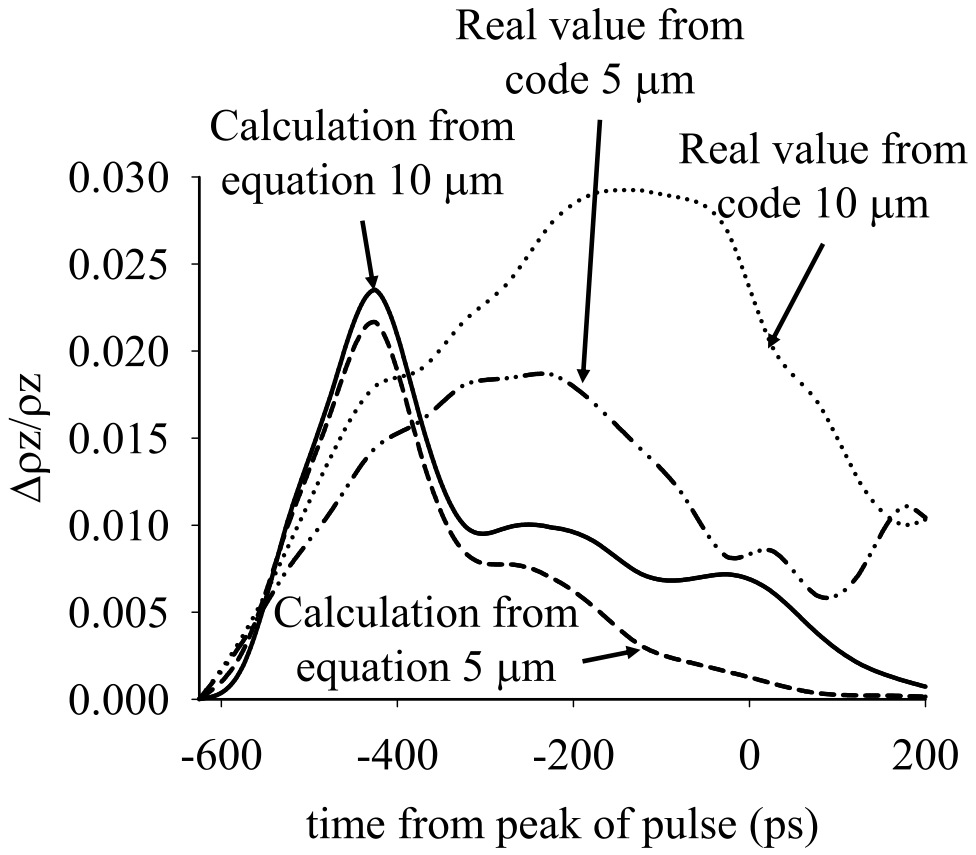

FIGURE 5.9: Comparison of simulated target-average rms areal density for a 10 μm target from calculation (using equation (5.1)) and generated directly by the POLLUX code. The following modulation wavelengths are shown: calculation 10 μm (solid line), real value from code 10 μm (dotted line), calculation 5 μm (short dashed line) and real value from code 5 μm (dot-dashed line).

ps earlier than is shown by the code-generated rms areal densities. The evolution of the instability is different between the calculation and code in all of the four modulation wavelengths shown.

Accurate determination of the RTI growth rate is reliant on reliable opacity data, and an assumption of constant opacity or linear scaling with density as made by various authors [5, 46, 47] is incorrect (see opacities shown in figure 2.8). In order to use the method based around equation (5.1) for these RTI growth measurements, it is important to select target materials and probing photon energies where the

opacity does not change significantly upon ablation.

5.1.3 Conclusion

The use of EUV probing to characterise RTI for CH plastic targets has been explored. Study of transmission and change in areal density have shown that solid density material dominates the absorption for longitudinal EUV radiography. In order to elucidate the evolution of the RTI, the material opacity, being both density and temperature dependent, must be known and taken into account, where assumptions of constant opacity are incorrect. It has been seen that lateral transport is an important factor in determining the ablation pattern of planar targets undergoing RTI. However, significant smoothing occurs only for modulation wavelengths less than ~ 50 μm. This can be used to minimise the growth of RTI, that leads to deformation of the outer shell of ICF targets, by, for example, introducing laser speckle patterns with modulations of shorter wavelength.

5.2 H2d in modelling x-ray backlighter iron opacity measurements

The 2D radiation hydrodynamic code h2d, introduced in chapter 4, has been used in support of an experimental study into the opacity of iron for solar models. The basis of the experiment, conducted at the Bhabha Atomic Research Centre, was the use of signature K_α (energy $E_{K\alpha} = 1.5$ keV) emission from a laser heated

aluminium layer to probe an iron target. 0.8 μm of aluminium was deposited on a 1 μm thick iron layer and heated by a single 500 ps, $\sim$ 8 J optical laser pulse with 120 μm focal spot. A crystal spectrometer was employed to measure K_α emission transmitted through the aluminium and iron layers, and compared to the transmission through a cold iron target and with no iron layer present, where filtering was employed to remove the dominant He_α signal. Measurements of frequency dependent opacity are key for benchmarking of models, where direct measurements of the star's interior structure are not possible [92]. For example, within a star the heavy elements will sink under the influence of gravity. Radiation pressure opposes this, the force of which is proportional to the frequency-resolved opacity [92]. For experimental details and analysis the reader is referred to Rossall et al. [143].

5.2.1 Simulation parameters

A 200 μm diameter aluminium-iron target of thickness 0.8 and 1 μm respectively, was first specified within an h2d input file. A 1.064 μm laser source, incident normally on the aluminium surface, has been used to simulate laser ablation and determine heating of the buried iron layer. Three simulations were conducted, with laser energies of 7.3, 8 and 8.6 J, to provide a range of transmissions for comparison with experiment. The laser profiles and a diagram of the target are presented in figure 5.10. A flux limiter of 0.1 was selected based on laser parameters [135, 136] and an energy dump of 20% at the critical surface assumed [144, 145]. Outputs of mass density and electron temperature for each zone, as well

as the mesh coordinates, have allowed calculation of the transmission of 1.5 keV photons, by incorporation of the IMP opacity code [106] and with use of the post processor described in chapter 4. SESAME equation of state data was included for aluminium and iron [142].

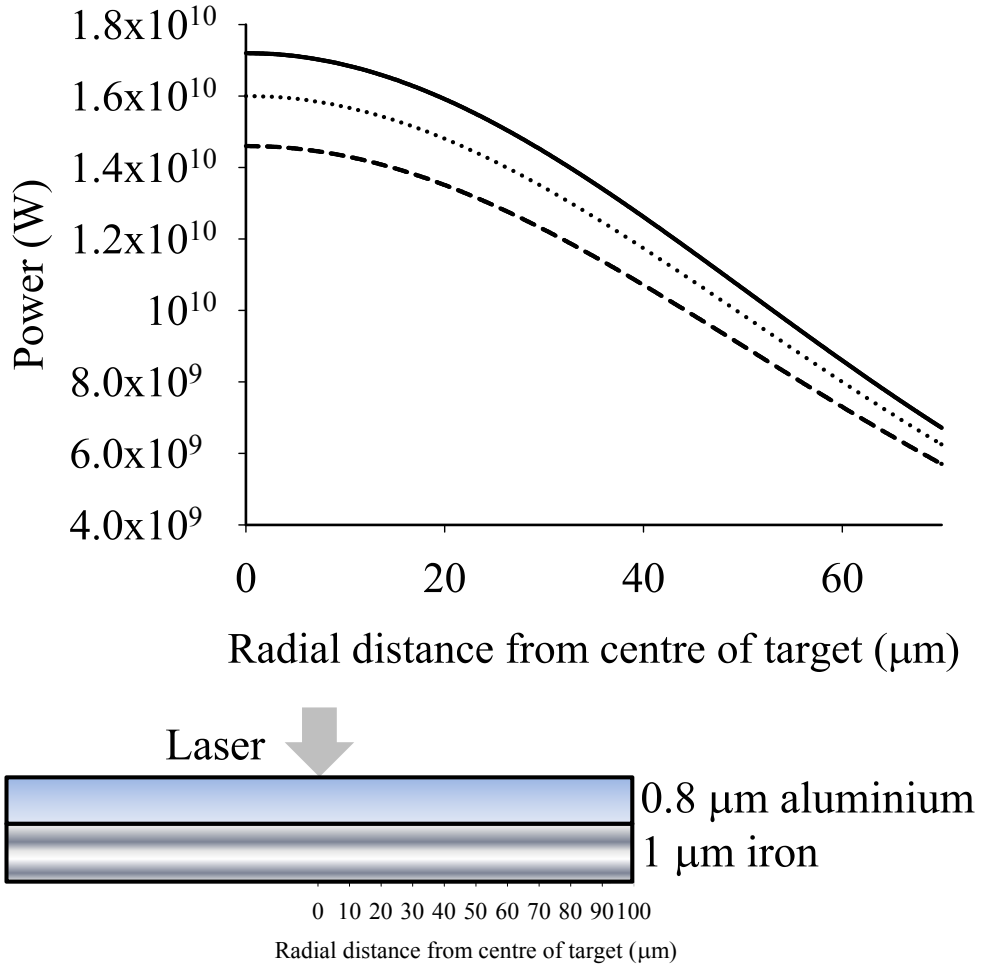

FIGURE 5.10: Laser power profiles for h2d simulation from the centre of the cylindrically symmetric target. Shown are the profiles for the 7.3 (dashed line), 8 (dotted line) and 8.6 (solid line) J optical laser pulse. Below is a diagram of the aluminium-iron target as simulated.

5.2.2 Simulation results and discussion

Axial transmissions through the iron layer were calculated for the three laser energies and superimposed on the experimental data points (see figure 5.11). Good

agreement with the experimental results is seen for the three energies studied. The transmission, seen in figure 5.11, increases from 10 to 30% over the 7.3 to 8.6 J laser beam energy range. Comprehensive analysis of the experimental data can be found in [143].

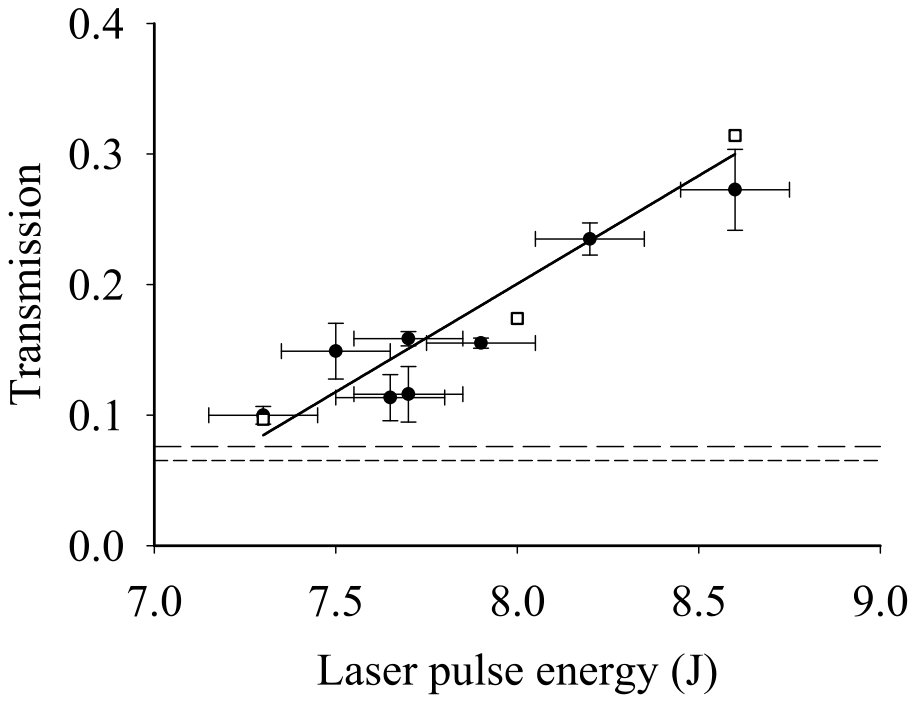

FIGURE 5.11: Transmission of K_α photons through an iron layer as a function of laser pulse energy as determined by experiment. The filled squares show experimentally determined transmissions with a line of best fit (solid line) [143] and the open squares show h2d simulated transmissions for 7.3, 8.0 and 8.6 J beam energies. Also shown is the experimentally measured cold iron transmission (long dashed line) [143] and the corresponding value taken from the literature (short dashed line) [56].

For the simulations, the transmission was selected at the time of peak K_α flux. This was determined from a simple theoretical model of target emission based on collisional excitation of the K-shell, together with h2d simulated densities and temperatures. The total aluminium K_α emission $\epsilon_{K\alpha\text{total}}$ can be derived from the

electron collisional excitation rate K for the aluminium plasma, with

$$\epsilon_{K\alpha} = N_i N_e K \propto N_e \int_{\sqrt{2E_{Z^*}/m_e}}^{\infty} \sigma(v) v g_v(v) dv \tag{5.2}$$

given by ion and electron densities N_i and N_e, energy of the K-edge E_{Z^*} and electron velocity v and mass m_e, electron velocity distribution function g_v and cross section for K_α production $\sigma(v)$ [94].

The electron velocity distribution can be represented by a Maxwellian distribution

$$g_v(v)dv \propto \frac{v^2}{T_e^{3/2}} exp\left(-\frac{m_e v^2}{2T_e}\right) \tag{5.3}$$

for electron temperature T_e. Assuming for this simple model that the cross section remains constant for energies greater than E_{Z^*} (see away from the K-edge [146, 147]), and now considering in terms of energy, equation (5.2) integrates to

$$\epsilon_{K\alpha} \propto N_e \left[\frac{E_{Z^*}}{\sqrt{T_e}} + \sqrt{T_e}\right] \left(-\frac{E_{Z^*}}{2T_e}\right). \tag{5.4}$$

The h2d simulated electron density and temperature have been used to calculate emission from each zone and, integrating axially, this provides the total aluminium K_α emission $\epsilon_{K\alpha\text{total}}$. Multiplying by the transmission through the iron layer provides the flux through the target, as is shown together with the simulated emission and transmission in figure 5.12. For comparison with experiment, values of simulated transmission were taken at the time of peak flux (figure 5.11). The transmission of the iron skews the peak of the detected emission profile to a later

time, which must be considered for future use of this probing method.

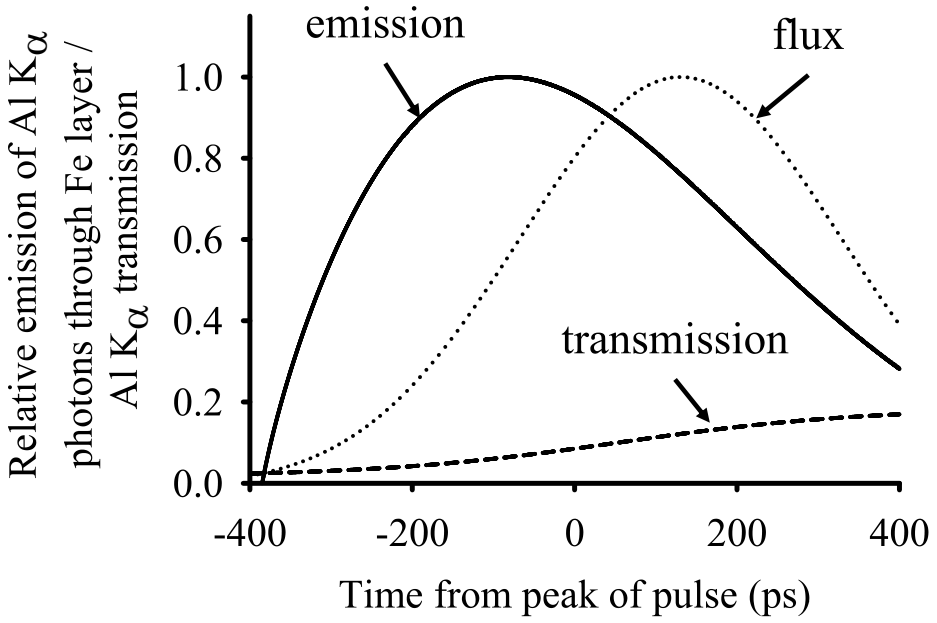

FIGURE 5.12: Flux of aluminium K_α photons through an iron layer at the radial centre of the laser beam, from h2d simulation of the aluminium-iron targets for a 7.3 J 500 ps laser pulse assuming a focal spot width of 120 m (dashed line). The flux is the product of the emission of aluminium K_α from the aluminium layer (solid line) and transmission of aluminium K_α through the iron layer (dotted line).

Experimentally determined spectroscopy measurements indicated a two temperature spatial distribution of the plasma, with a hot central temperature of (1.0 ± 0.1) keV and cold outer temperature of (140 ± 10) eV, brought about by the Gaussian profile of the heating beam and enhanced by whole-beam self focussing within the coronal region [143]. The two dimensional code, h2d has been used to investigate the spatial dependence of laser heating for this beam profile. Radial temperature profiles are presented in figure 5.13 for the three beam energies simulated. Figure 5.13 shows evidence for a hot central plasma of ≈ 1 - 1.7 keV and cold surrounding plasma of ≈ 100 - 200 eV, therefore approximately agreeing

with the experimental measurements. The profiles of figure 5.13 show the higher laser energies causing an increase in the self-focussing effect, demonstrated by the temperature profile narrowing between the 7.3, 8 and 8.6 J simulations.

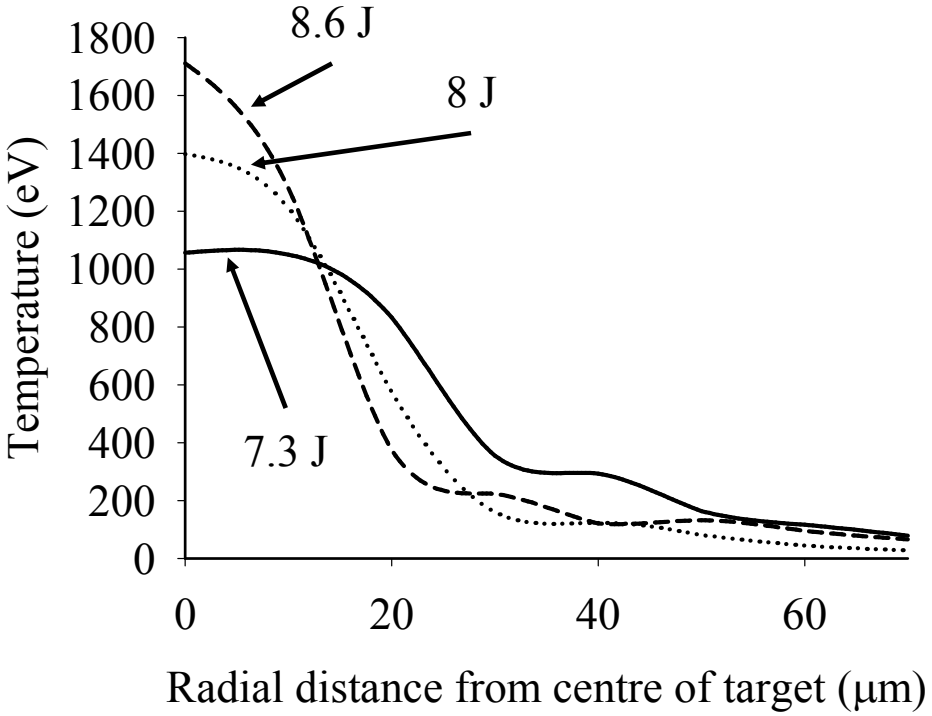

FIGURE 5.13: Radial temperature profiles for an ablated aluminium-iron target, taken from h2d simulation. Shown are the simulated temperatures at the critical surface in the aluminium layer for a 7.3 J (solid line), 8 J (dotted line) and 8.6 J (dashed line) pulse at the time of the peak of the heating pulse.

Increased focussing of the laser beam within the coronal plasma has led to a higher intensity at the critical surface, and therefore increased heating. Thermal conduction transfers energy from the critical surface to the layers below, resulting in a higher iron temperature and ionisation. Once sufficiently ionised the iron plasma becomes transparent (see explanation relating to CH plasma in chapter 6 for an analogous discussion). The iron becomes transparent to the 1.5 keV photons leading to a rise in transmission (see figure 5.11).

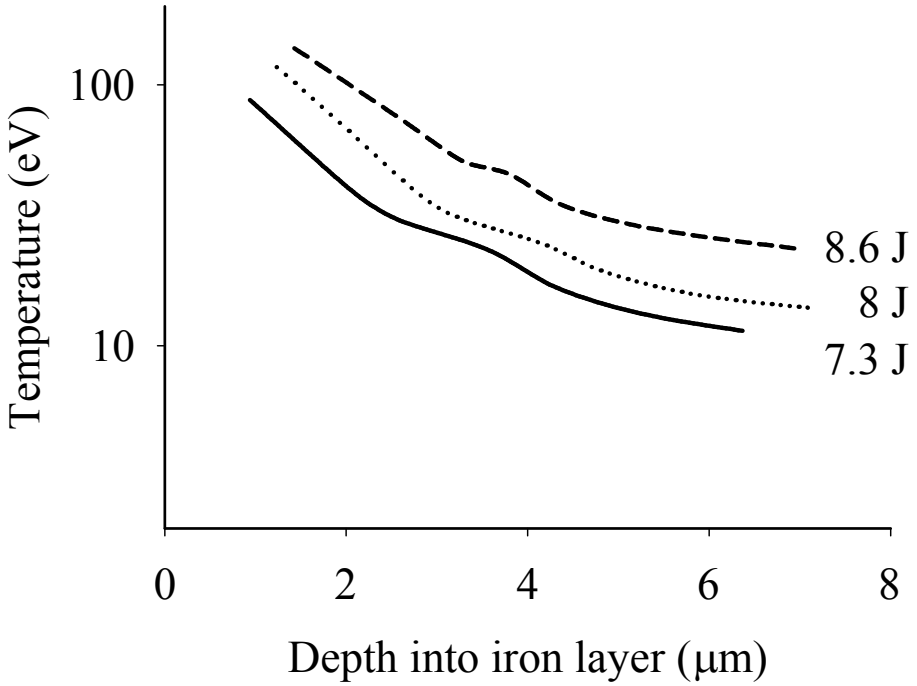

FIGURE 5.14: Axial temperature profiles through the iron layer of an ablated aluminium-iron target, taken from h2d simulation. Shown are the simulated temperatures at the centre of the target for a 7.3 J (solid line), 8 J (dotted line) and 8.6 J (dashed line) pulse at the time of the peak of the heating pulse.

Axial temperature profiles have also been extracted from the simulations, at the time of peak aluminium K_α flux. Figure 5.14 shows a near order of magnitude decrease in temperature from the front to back side of the iron layer with a range of 10 eV to 70 eV for the 7.3 J pulse simulation and 20 eV to 150 eV for the 8.6 J pulse. For comparison, a temperature of $\sim$ 190 eV is predicted for the boundary between the radiative and convective zones in the sun [90]. A near order of magnitude range is also seen for simulated density with a range of 0.2 g cm^{-3} to 1.1 g cm^{-3} for the 7.3 J pulse and 0.1 g cm^{-3} to 0.8 g cm^{-3} for the 8.6 J pulse. Due to the non-uniformity of the plasma formed, an opacity measurement could not be made. However, with the use of a tamp on the back side of the target this may be improved, thereby achieving the aim of providing a measure of opacity

in a single shot, without the need for separate heating and probing beams.

5.2.3 Conclusion

H2d simulation of an iron opacity experiment has been conducted as a test of feasibility into using a single pulse to both heat and probe an iron layer, providing a simpler method for measuring solar opacities than pump-probe experiments (where separate heating and probing beams are required). A self-focussing effect of the laser beam within the coronal aluminium plasma was noted experimentally, and has also been seen in 2D simulation. Simulation was shown to be in good agreement with experimentally determined transmission data, the measurement of which is required for determining opacity. However, it was also seen that under the conditions of the experiment large temperature and density gradients form, preventing a value of opacity from being found. For future work this effect can be lessened by using of a thick, tamp material on the back of the target to prevent expansion. A 5 μm tamp of CH plastic would result in only a 30% decrease in transmission for the 1.5 keV probe photon energy, so would be suitable.

5.3 H2d in modelling heating of iron opacity targets

A broadband germanium EUV backlighter source, created using the VULCAN laser, CLF, RAL, was used to determine the evolution of transmission through thin

(50 nm) heated iron targets, under irradiances of $\sim 8 \times 10^{16}$ W cm^{-2}. The primary diagnostic for this work was the flat field spectrometer, described in section 3.2. For experimental details of the broadband EUV source and analysis the reader is referred to Wagenaars et al. [117]. Within this section simulation results are presented, together with the EUV transmission through the targets as measured experimentally.

5.3.1 Simulation parameters

The code h2d has been used to simulate laser heating of a thin, iron target of 50 nm thickness with 100 nm plastic (parylene-N) front surface tamp and 100 nm back surface tamp, as depicted in figure 5.15. A 1.054 μm wavelength, 24.9 J, 1 ps pulse was set incident on the front side of the target, with a Gaussian temporal intensity profile and a focussed Gaussian spatial profile of full-width-at-half-maximum 200 μm (see figure 5.15). The peak irradiance is $\sim 7.9 \times 10^{16}$ W cm^{-2}. Prior to the heating pulse, a prepulse inherent to the VULCAN laser, of duration 1 ns and irradiance contrast 10^{-7} was modelled. The presence of the prepulse, produced by ASE within the laser system, will alter the target for interaction with the main, intense part of the pulse.

For h2d simulation a flux limiter of 0.06 was selected based on experimental evidence for thin multilayer targets [137]. The mass density, electron temperature and mesh coordinates during the ablation of the target were calculated for each zone by the code. The IMP [106] or LEDCOP [99, 107] opacity codes for iron and

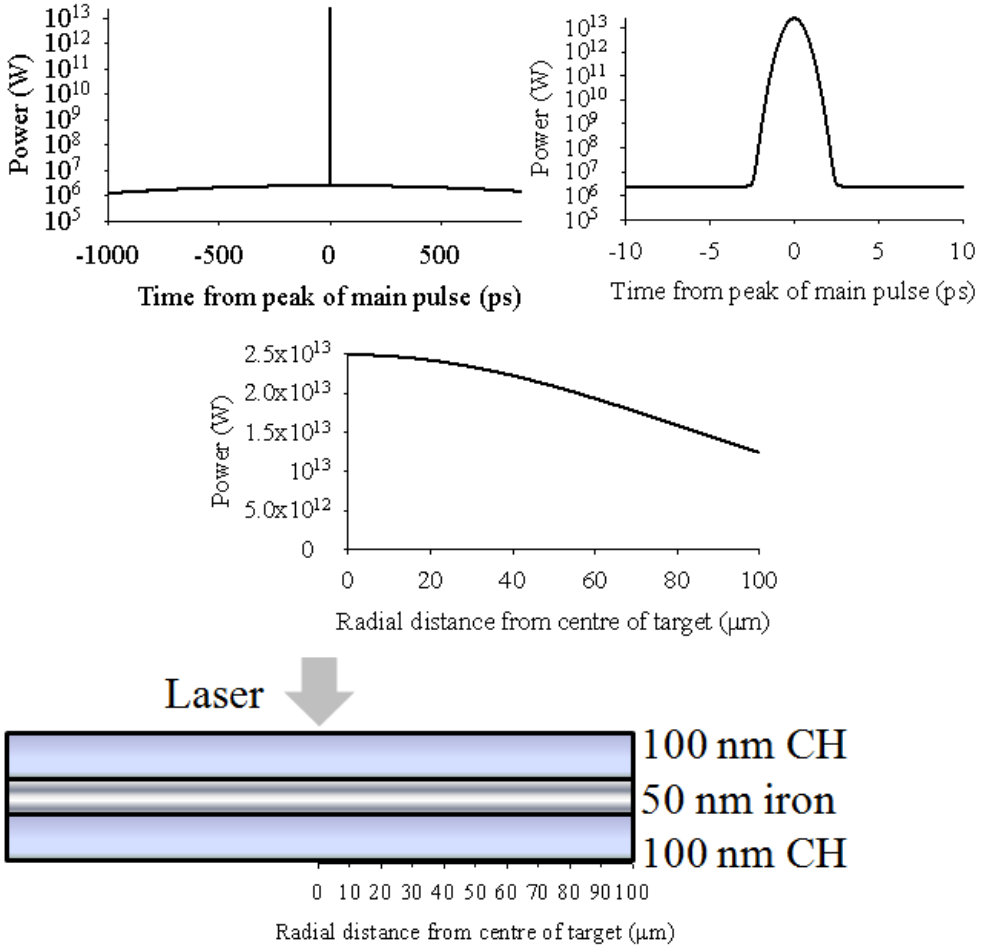

FIGURE 5.15: Laser power profiles for h2d simulation from the centre of the cylindrically symmetric target. Shown are the temporal and spatial profiles of the heating beam. Below is a diagram of the plastic-iron-plastic target as simulated.

CH plastic were used, together with a post processor to evaluate the transmission of EUV backlighter photons through the target.

5.3.2 Simulation results - EUV transmission

Experimental and simulated transmissions are shown in figure 5.16 for varying delays between target ablation and EUV backlighter emission, taken from analysis of flat field spectrometer images. The predicted cold transmission, taken from

tabulated values [56], is also shown and found to be in agreement with the experimental value. For more details regarding the experiment see Wagenaars et al. [117].

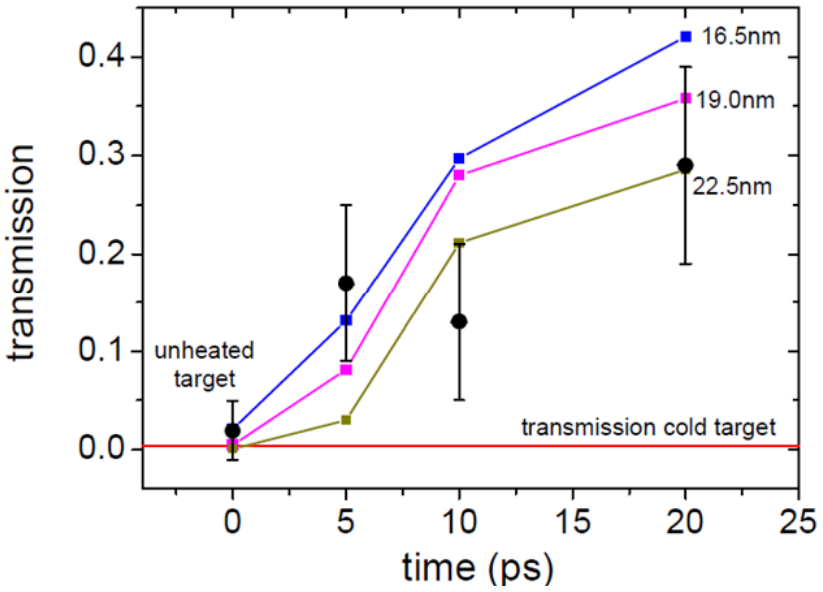

FIGURE 5.16: The resulting measured EUV transmissions averaged over the wavelength range 18 - 22 nm captured by the flat field spectrometer through an ablated iron target are shown as a function of time delay between ablation and probing. Also shown are simulation results for iron transmissions at three different arbitrary wavelengths across the germanium backlighter spectrum [117].

A rapid increase in transmission from $\sim$ 0 to 30% is seen during the first 20 ps from the peak of the heating pulse. As a test of the simulated transmission values, and in particular use of the IMP opacity code, radial transmissions are presented in figure 5.17, calculated using both IMP [106] and LEDCOP opacity data fixed to cold opacities (see section 2.2.2 for description and comparison of these two codes). In this regime the transmission results obtained with the two different opacity codes are in approximate agreement as there is a significant contribution to the transmission from the cold, unablated material.

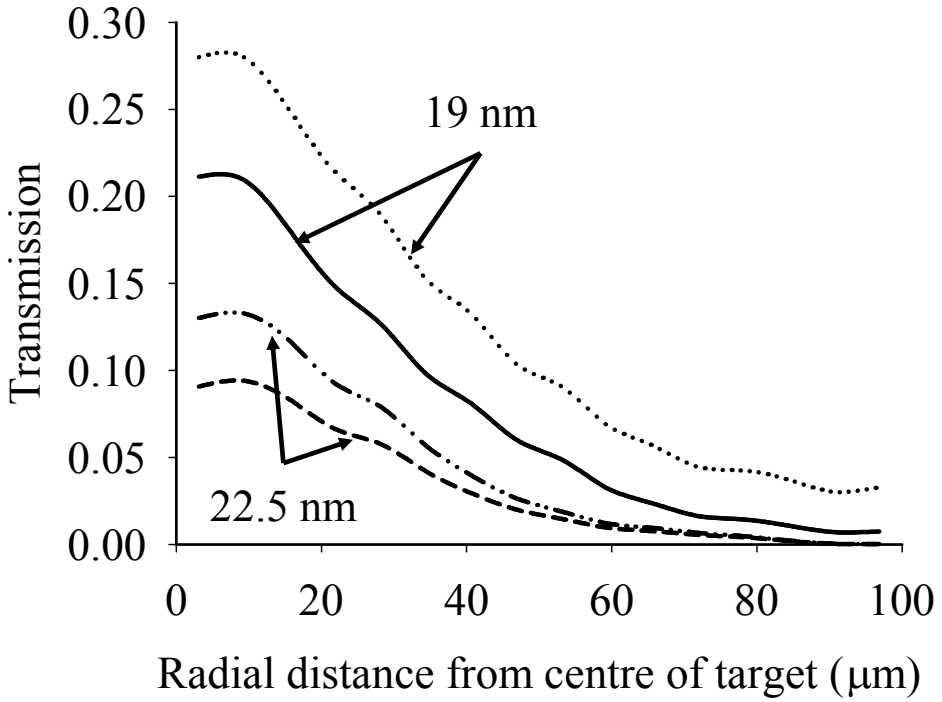

FIGURE 5.17: Radial transmission profiles calculated using h2d simulated data and two opacity codes. Shown are profiles for a 19 nm probe wavelength using IMP (solid line) and LEDCOP (dotted line) data and a 22.5 nm probe using IMP (dashed line) and LEDCOP (dot dashed line) data.

5.3.3 Simulation results - Density and temperature

The short duration heating beam leads to rapid changes in plasma parameters, as is shown in the profiles of temperature and density within the iron layer (see figures 5.18 and 5.19). The values shown in figures 5.18 and 5.19 have been averaged axially through the initially 50 nm thickness of iron, and are shown as a function of radial distance from the centre of the cylindrically symmetric h2d target.

The density drops as the plasma expands, rapidly decreasing at the centre of the target from approximately 7 g cm^{-3} to 2 g cm^{-3} between 5 and 10 ps after the peak of the heating pulse (see figure 5.18). Due to the presence of the 100 nm tamping layer on top of the iron layer the expansion is, at first, hindered and the density of the iron layer is near the solid value of 7.87 g cm^{-3} at 5 ps into ablation

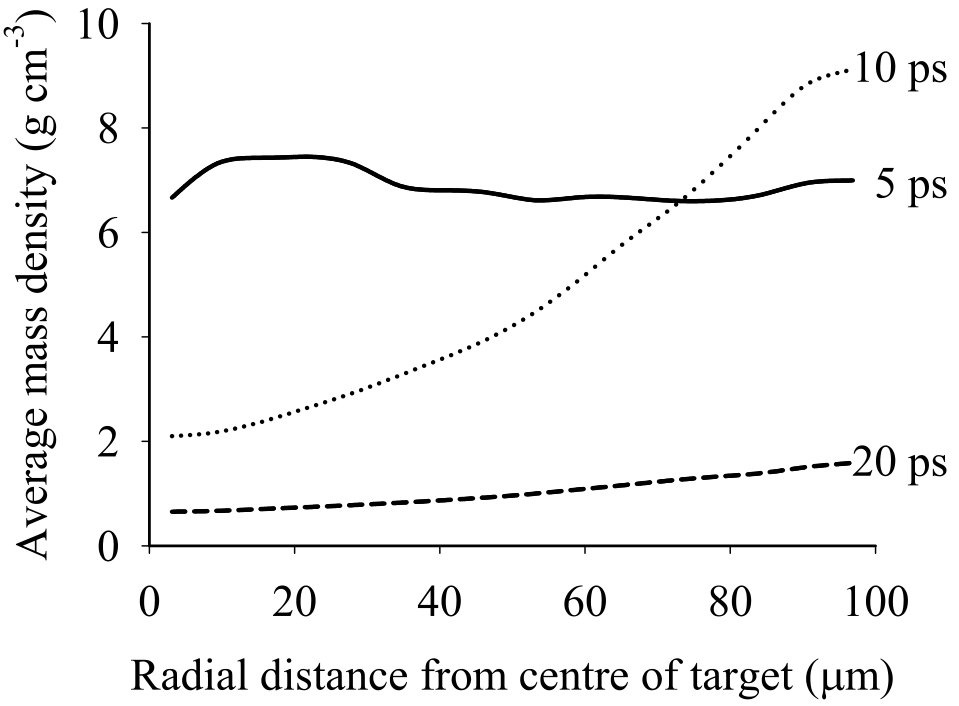

FIGURE 5.18: Radial mass density profiles taken from h2d simulation of a laser heated iron target. Shown are axially averaged profiles within the iron layer of the modelled targets at 5 ps (solid line), 10 ps (dotted line) and 20 ps (dashed line) from the peak of the 1 ps heating pulse. Data is shown across the focal radius of the target (100 μm). The solid density of iron is 7.874 g cm^{-3}

by the heating beam and 1 ns after the onset of the low-intensity prepulse (see the solid line in figure 5.18).

Figure 5.20 shows the axial profile of electron density 10 ps from the peak of the heating pulse. The critical density $N_{\rm crit}$ ($= \pi/(r_0\lambda^2)$cm^{-3} for classical electron radius r_0) for the $\lambda = 1.054$ μm wavelength heating beam is indicated. From figure 5.20 it is seen that the critical surface lies within the CH plastic layer at this time.

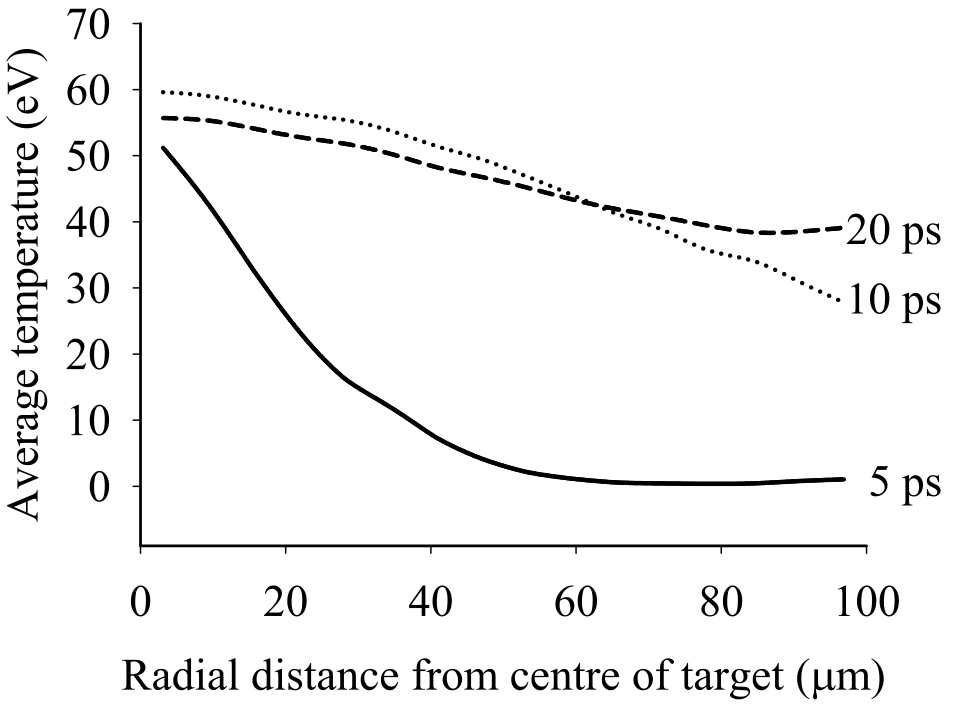

FIGURE 5.19: As figure 5.18 with radial temperature profiles. Shown are axially averaged profiles within the iron layer at 5 ps (solid line), 10 ps (dotted line) and 20 ps (dashed line).

Further out from the centre of the target the laser pulse has caused heating with a different pattern of evolution. For the temperature (see figure 5.19), thermal conduction from the critical surface has allowed heating within the iron layer leading to a temperature gradient across the target at early time (see the solid line in figure 5.19). After 10 ps the effects of lateral transport can be seen in both the temperature and density profiles. The cooler outer regions of the target have experienced minimal expansion and the density remains at solid value, with extra material being pushed from the central, hotter region. As material and heat is conducted outwards, the temperature of the outer regions increases in time.

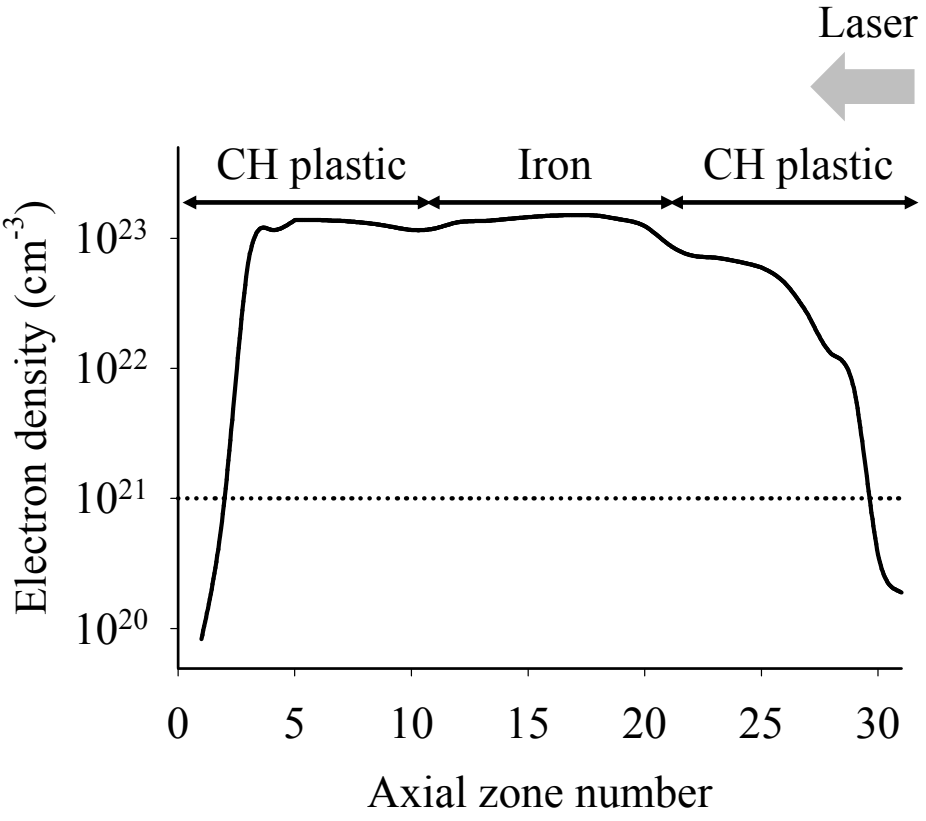

FIGURE 5.20: Axial electron density profile at the centre (radially) of the incident beam taken from h2d simulation of a laser heated plastic-iron-plastic target, 10 ps from the onset of irradiation (solid line). The position of layer boundaries and direction of the heating beam are shown, as is the critical density (dotted line).

The density (see figure 5.18) continues to drop as the target expands and slowly cools. The increase in predicted transmission (figure 5.16) reflects the rapidly changing temperature and density in the centre of the target at early time.

To test the suitability of the experimental data in measuring opacity, the uniformity of the iron layer has been found. In figures 5.18 and 5.19 average density and temperature profiles were presented for the iron layer. In figure 5.21 (a) and (b) the density and temperature range (from the front side to the back side of the

iron layer) is now shown, for a time 10 ps from the peak of the heating pulse.

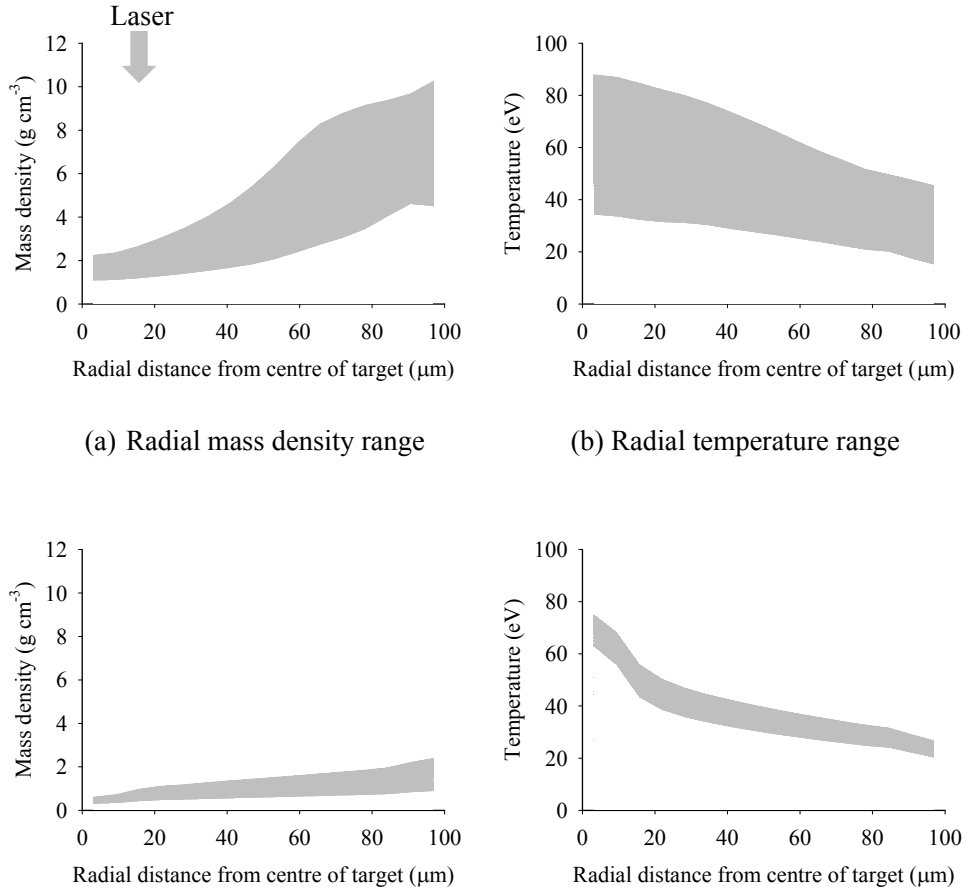

(a) Radial mass density range (b) Radial temperature range

(c) Radial mass density range (modified) (d) Radial temperature range (modified)

FIGURE 5.21: Radial mass density and temperature ranges from the front side to the back side of the iron layer, taken from h2d simulation of a laser heated (tamped) iron target, 10 ps from the peak of the 1 ps heating pulse. Data is shown across the focal radius of the target (100 μm) with (a) mass density, (b) temperature, (c) mass density - 'modified simulation' (see text) and (d) temperature - 'modified simulation' (see text). The shaded regions indicate the range of values through the iron layer.

At the centre of the target (which is cylindrically symmetric), the density range from the front side to the back side of the iron layer is 1.1 g cm^{-3} and the temperature range is 54 eV. For use as a benchmark for opacity codes, the ablation of the thin (50 nm) iron layer would need to be optimised, reducing this gradient, such that the resultant transmission could be attributed to iron of known temperature

and density. Increasing the tamping layer thickness should further reduce the ablation of the iron during the time of peak heating [148]. It is also advantageous to reduce the thickness of the iron layer, so that heating can occur more rapidly over the target [148]. By improving the contrast of the heating beam, i.e. reducing the intensity of prepulse, less ablation will occur prior to the arrival of the main pulse, reducing the gradients in the iron plasma.

To test these proposals the simulation above has been repeated, increasing the thickness of the two tamping layers from 100 nm to 200 nm, while decreasing the thickness of the iron layer from 50 nm to 30 nm and improving the contrast by 10^2. All other parameters of the simulation have been kept the same. The resulting density and temperature range is shown in figure 5.21 (c) and (d) (referred to as the 'modified simulation').

With these modifications the density range from the front side to the back side of the iron layer has now reduced to 0.3 g cm^{-3} and the temperature range to 12 eV. From figure 5.21 (c) it is seen that the density, as well as being more uniform axially, is lower than for the experimental parameters (comparing figure 5.21 (a) and (c)). With the reduced prepulse intensity, the critical surface is now deeper within the plasma, altering the heating of the iron layer. Correspondingly, the iron layer at target centre had expanded from 50 nm to 220 nm at 10 ps in the original simulation of the experiment, compared to an increase of 30 nm to 450 nm in the 'modified simulation'.

5.3.4 Simulation results - EUV emission vs. EUV lasing

Experimental transmissions were obtained using a broadband germanium EUV backlighter source, where multiple lines of germanium emission made up the resulting spectrum in the 18 - 22 nm wavelength range [117]. The duration of EUV emission, and from this the temporal resolution of the transmission measurements, was not recorded experimentally. The EHYBRID code [149] was used to model the time history of EUV emission predicted in the 18 - 22 nm range in germanium, under experimental conditions [117, 150]. The resulting temporal profile is shown in figure 5.22. A long duration of emission (160 ps compared to the 1 ps irradiating pulse) is predicted, the effect of which would be to increase the range of density and temperature of the iron layer during probing, weakening this method as a measure of opacity.

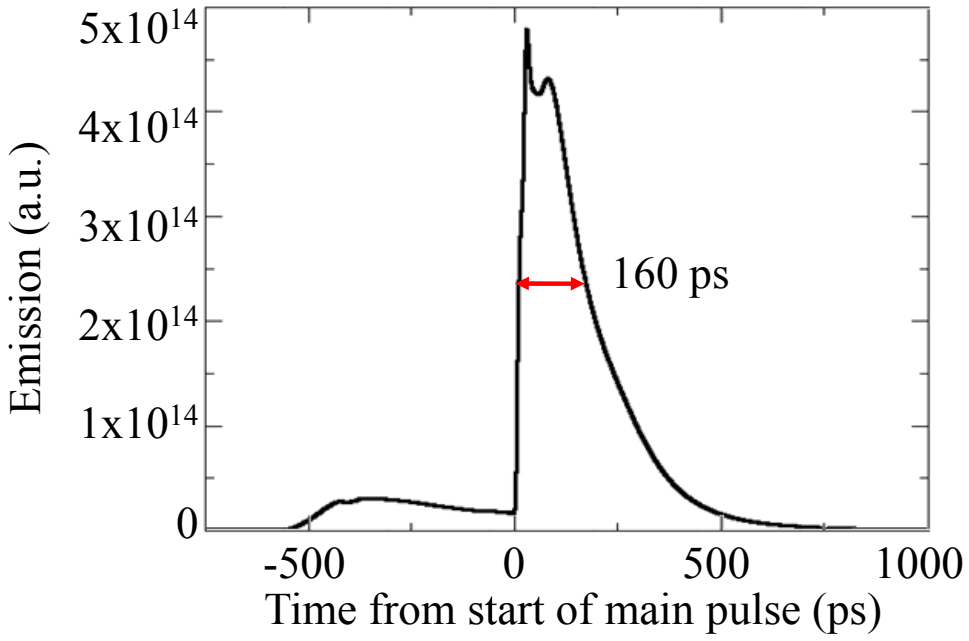

FIGURE 5.22: EHYBRID model of the time history of EUV emission from a germanium target, under experimental conditions [117, 150]. The full-width-at-half-maximum duration for the emission is 160 ps.

Previously EUV lasers have been used for probing at discrete wavelengths, allowing specific absorption features to be investigated at higher temporal resolution [50, 53]. The h2d simulation described above, with original target design of 50 nm of iron with a 100 nm plastic front and back surface tamp and original prepulse to main pulse contrast of 10^{-7}, has been taken in conjunction with IMP opacities [106] to calculate EUV transmissions at discrete wavelengths. Simulated transmissions of the lasing lines for germanium and molybdenum through the target have been investigated, these being 23.6 and 18.9 nm respectively. IMP opacity code data was selected for these photon wavelengths, with transmissions being calculated as before. The simulation results are shown in figure 5.23 (a) and (b).

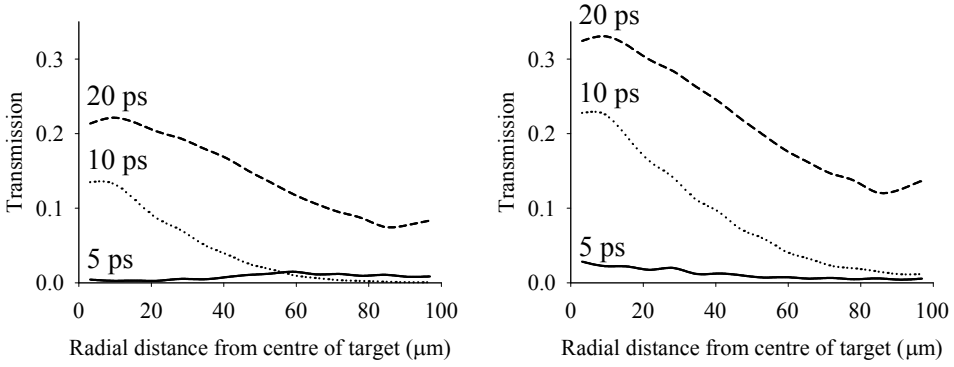

FIGURE 5.23: Radial transmission profiles taken from h2d simulation and IMP opacities for a laser heated iron target at (a) 23.6 nm probe wavelength and (b) 18.9 nm probe wavelength. Shown are profiles at 5 ps (solid line), 10 ps (dotted line) and 20 ps (dashed line) from the peak of the 1 ps heating pulse. Data is shown across the focal radius of the target (100 μm).

The general trend demonstrates the lower transmission for the longer wavelength (lower photon energy) probe (figure 5.23). The transmission also drops further out from the centre of the target, where the iron material is denser and cooler. However, at early time (see the transmission curve at 5 ps in figure 5.23 (a)) one of

the many absorption features in iron has reversed this trend and the transmission is higher further out from the centre of the target for the 23.6 nm probe. The absorption feature can be seen in the profile of solid state iron opacity in figure 5.24 [56].

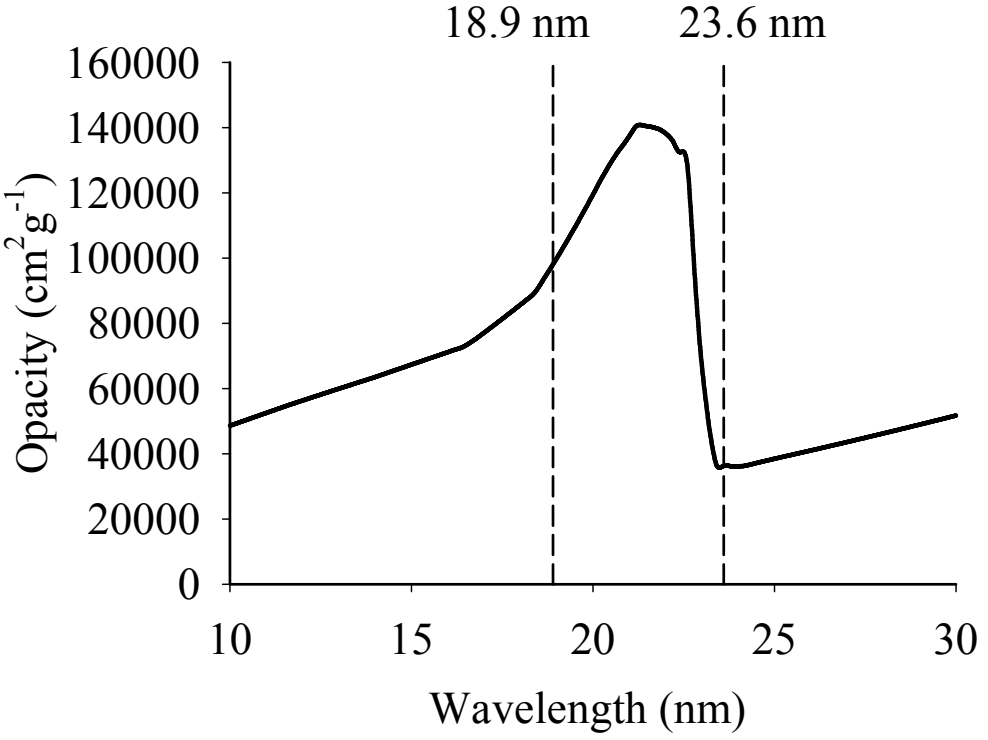

FIGURE 5.24: Opacity, as specific cross section σ_s, of solid state iron as a function of probe photon wavelength, taken from [56]. Indicated are the probe wavelengths 18.9 nm and 23.6 nm.

As is seen in figure 5.24, in general opacity increases with increasing wavelength. The presence of the absorption feature changes this, resulting in a lower opacity for the 23.6 nm probe compared to the 18.9 nm probe. Consequently the transmission through the cooler, denser plasma at early time is higher for the 23.6 nm probe

than the 18.9 nm probe (comparing the transmission curves at 5 ps in figure 5.23 (a) and (b)). This demonstrates the importance of including absorption features in models of opacity, and the use of narrowband EUV probes in detecting them.

5.3.5 Conclusion

Simulation has been carried out, modelling heating of iron opacity targets and calculating the transmission of EUV sources for comparison with experiment. Profiles of temperature have shown poor uniformity over the iron layer, preventing an opacity measurement from being made. Improvements in target design for future work have been suggested. By examining transmission profiles at different wavelengths across the broadband EUV spectrum, the need for accurate opacity data containing absorption features has been highlighted. Differences in transmission calculated using the IMP and LEDCOP opacity codes were found, but for this work were within the experimental error.

Summary

Within this chapter three simulations of laser ablation have been presented. Both the POLLUX and h2d radiation hydrodynamic codes have proven to be useful in support of experimental effort into instability formation in laser ablation and iron opacity for solar models. Through simulation it has been possible to find weaknesses in experimental methods, and propose improvements for future work. The role of modern opacity codes in studies of laser ablation has been demonstrated.

Chapter 6

EUV interferometry of warm dense matter in laser-plasmas

6.1 Introduction

Since their inception EUV lasers have been used to probe the properties of laser-plasmas [4, 36, 45, 46, 47, 59, 138]. Interferometry at EUV wavelengths has enabled study of lower density plasma plumes [59] and shown that anomalous refractive indices η (e.g. with $\eta > 1$) can exist in plasmas dominated by strong absorption features [151].

The constraints of probing laser ablated targets were laid out in section 1.2.2. The critical density of a plasma scales with wavelength λ as λ^{-2}, such that EUV light at wavelengths less than approximately 40 nm can penetrate through plasmas with

greater than solid density without collective absorption associated with the critical density, which impedes longer wavelength probing.

By carrying out EUV interferometry the properties of plasma material found between the critical and ablation surfaces can be determined, through the interpretation of interferograms containing both absorption and phase shift data. With increasing density and lower temperature, the warm dense plasma material between the critical density surface and ablation surface in a laser-plasma interaction can have an equation of state not properly described by either solid state or plasma physics [111]. Within this same region is the greatest disagreement between theoretical opacity codes, as described in section 2.2.2. It is also difficult to measure the plasma properties in this region as, for example, spectral emission is dominated by the hot plasma found at densities $\leq$ critical density. Similarly measurements of laser produced plasmas at electron densities near to or greater than the critical density cannot be accurately made by optical laser probing due to refraction (at electron densities below and within typically an order-of-magnitude of the probe critical density) or non-penetration (at electron densities greater than the probe critical density) [110]. X-ray probing or scattering can be effective in diagnosing warm dense plasma [112], but scattering output increases with density so that cold, solid target material can readily dominate measurements rather than the elusive material between the critical density and ablation surfaces.

High-power laser light ($> 10^9$ Wcm^{-2}) rapidly produces an expanding plasma when incident onto solid targets so that the major component of a laser pulse only penetrates to a critical electron density ($= \pi/(r_0\lambda^2)$ cm^{-3} for laser wavelength

λ with classical electron radius r_0). Laser energy absorbed up to the critical density is conducted to higher densities producing further ablation of material from the remaining solid target, thereby defining the region of interest between critical and ablation surfaces. The properties of the plasma where the electron density is greater than the critical density for the laser are crucial in understanding the physics of laser interaction with solid targets and consequently are of key importance for applications such as ICF [74]. In particular CH plastic, as is considered in this work, is of interest as a possible shell material for DT fuel pellets (see section 2.1).

EUV radiation (of $\lambda = 21.2$ nm) has interactions with warm dense plasma to produce signature effects of the plasma conditions via absorption and refractive index variations. Away from narrowband bound-bound absorption features, absorption of EUV radiation in the plasma between critical and ablation surfaces is mainly determined by bound-free transitions in different ionisation stages. Phase shifts are similarly determined by refractive index effects associated with bound-free and free-free absorption. The contributing processes have been described in section 2.2.1.

Transmission measurements of plasma-based EUV lasers have provided information on plasma opacity [53] and the rate of ablation of solid targets irradiated by optical lasers [50]. In an experiment by Edwards et al. [50] a study of laser ablation of solid iron was presented. The rate of ablation was found by considering the transmission of the EUV laser through the ablated target and transparency of

the rare iron plasma in the ablated region. This was carried out by direct measurement of the EUV laser throughput but by inclusion of an interferometer it is possible to get further measurement, in order to characterise the plasma.

Interferometry has been utilised to measure both transmission and phase information for an EUV laser beam at wavelength $\lambda = 21.2$ nm (photon energy 58.5 eV) probing longitudinally through laser heated CH plastic (parylene-N C_8H_8) targets (thickness 350 nm) irradiated by a 300 ps duration pulse of wavelength 438 nm and of peak intensity 10^{12} W cm^{-2}. By probing longitudinally (in approximately the same direction as the incident optical laser as depicted in figure 2.9, section 2.3), it has been possible to obtain spatially integrated values of phase shift (dependent on the real component of the material refractive index) and to determine the EUV probe intensity upon transmission (dependent on the absorption coefficient or equivalently the imaginary component of the material refractive index).

6.2 21.2 nm zinc EUV laser

The EUV laser at a wavelength of $\lambda = 21.2$ nm arising from a $3p - 3s$ transition in Ne-like zinc was produced using the PALS infrared (1.315 μm) laser operating with 480 ps duration output pulses [152]. The EUV laser was created by irradiating a solid zinc target of length 3 cm with a low-energy (< 2 J) prepulse focused to a 500 μm wide line, followed 10 ns later by the main pulse of 400 J, focused to a line of width 100 μm. The long scale length pre-plasma with which the main pulse interacts provides good conditions for gain by reducing refraction effects,

optimising the gain volume and maximising the absorption of the pump laser [1]. To improve further the brightness, reproducibility and uniformity of the EUV laser beam, a Mo/Si multilayer half cavity mirror (reflectivity of 30% at 21.2 nm [153]) was installed at the reinjection point of the beam and tuned to drive the laser emission further into saturation. Operating well into laser saturation, the EUV output energy per pulse was reproducible to within 30%. The position of the half cavity mirror has previously been optimised to produce the maximum amplification [153]. By having an extra pass of the system, significant amplification has been shown, despite mirror losses. Figure 6.1 shows EUV footprints taken for the single pass and double pass systems. A 5 times increase in peak EUV laser intensity for the double pass system is observed. During each shot the surface of the mirror is damaged limiting the number of shots possible to $\sim$ 100 before replacement is necessary [153]. A further disadvantage of the double pass system is that temporal stretching occurs, increasing the duration of the emission [154]. Streak camera measurements indicate that the pulse duration of the EUV laser pulse was 200 ($\pm$ 20) ps for the measurements described in section 6.4, defining the temporal resolution of the experiment. However, for longitudinal probing of dense plasmas a high-brightness EUV source is essential, justifying the use of the double pass system.

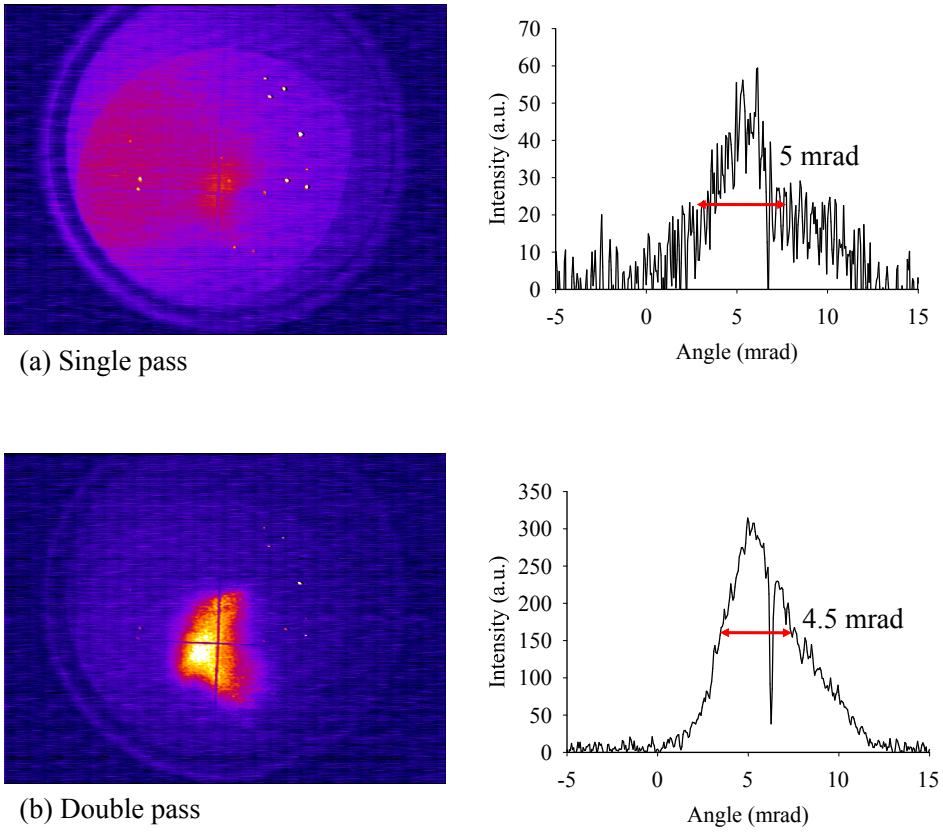

FIGURE 6.1: EUV laser footprints comparing intensity using the (a) single and (b) double pass amplification systems, together with background corrected vertical profiles obtained at the PALS facility. The beam is emitted at an deflection angle of 5.5 ($\pm$ 0.5) mrad [153]. The approximate full-width-at-half-maximum divergence for the beam is shown.

6.3 Experimental setup

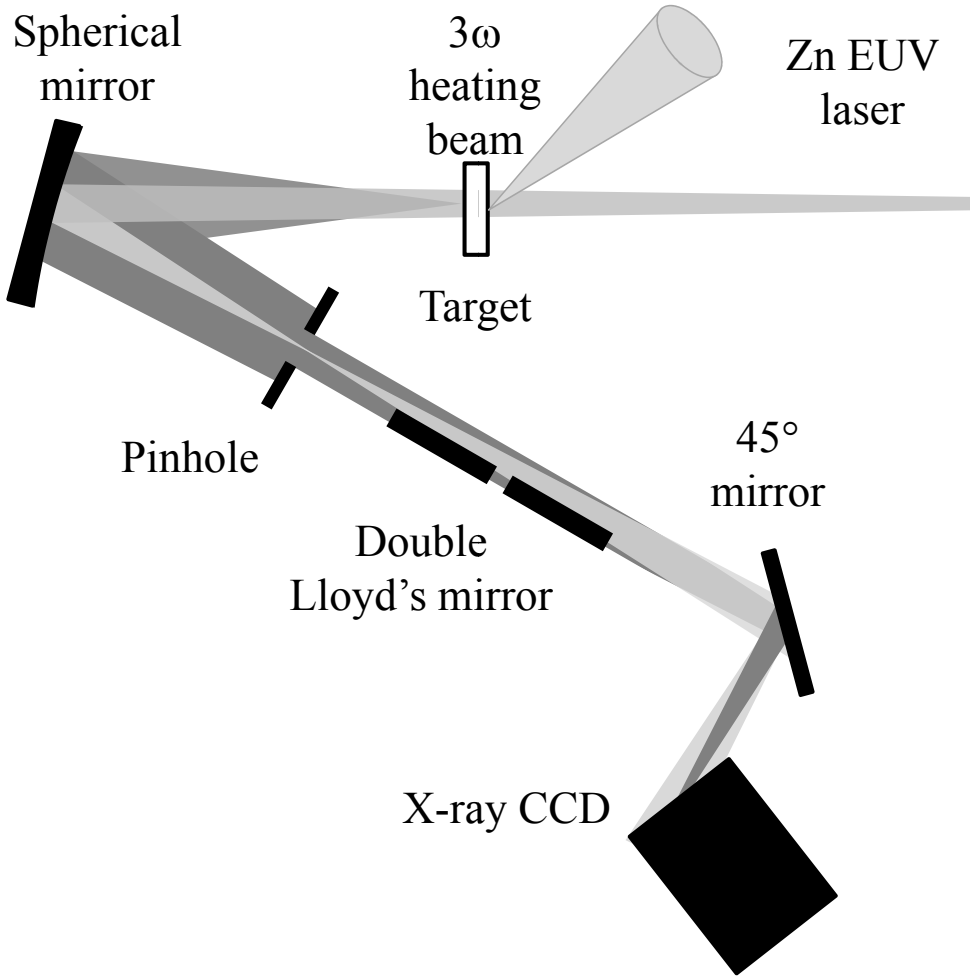

FIGURE 6.2: Experimental arrangement for EUV interferometry of planar CH plastic targets. The EUV laser and heating beam are both incident on the front side of the target. The focal position of the EUV laser is close to the pinhole. The sample target is imaged onto the CCD detector.

A schematic of the interferometry experiment is given in figure 6.2. The EUV laser passed normally through a 350 nm thick plastic sample target, heated by a 300 ps duration pulse of peak irradiance 10^{12} Wcm^{-2}, illuminating an area of 7 $\times$ 11 mm. The 438 nm wavelength heating pulse was focused to a 300 μm spot on target. A spherical multilayer mirror (giving a magnification $\times$ 6.75) imaged the sample target onto a CCD detector, placed with the detection area at an angle of

11° to the EUV beamline so that EUV interference fringes spaced at 8 μm at the sample target surface could be accurately recorded with the 13 μm size pixels on the CCD detector. A fringe spacing of 16 pixels was noted. A 400 nm aluminium filter blocked longer wavelength plasma radiation at the detector. The spherical mirror also acts as a filter to short wavelength radiation emitted by the target plasma, due to reduced reflectivity.

A pinhole was placed beyond the sample target, close to the focal point of the EUV laser, to reduce detection of plasma self emission and enhance contrast. This technique of spatial filtering for improved contrast in EUV probing is depicted in figure 6.3 [155]. The EUV probe illuminates the object normally, passing to the spherical imaging mirror [155]. Referring to figure 6.3 the near parallel rays of the EUV probe pass freely through the pinhole, located at the focal plane, whilst the majority of the isotropic self emission from the heated target is stopped by the pinhole [155]. Taking the total intensity of target emission for unobstructed propagation I_t, the intensity produced in the image plane by the mirror I_m is

$$I_m = I_t \Omega_m / (4\pi) \tag{6.1}$$

with spatial angle

$$\Omega_m = \pi d_m^2 / (4a^2) \tag{6.2}$$

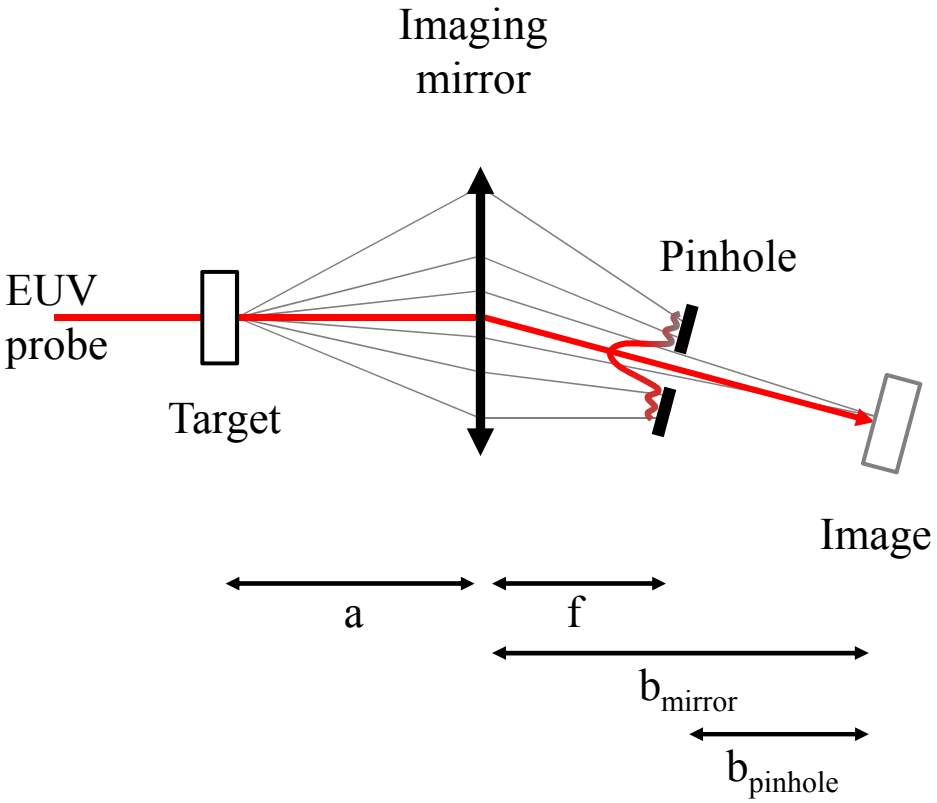

FIGURE 6.3: Diagram of the principle of spatial filtering for heated target self emission by a pinhole inserted close to the EUV probe focal point. Adapted from [155].

given by the mirror size d_m and target to mirror distance a. Upon insertion of the pinhole the revised intensity in the image plane I_p becomes

$$I_p = I_t \Omega_p / (4\pi) \tag{6.3}$$

with the spatial angle

$$\Omega_p = \pi d_p^2 / (4f^2) \tag{6.4}$$

given by the pinhole diameter d_p and focal length of the mirror f [155]. Combining these equations, the contrast enhancement in the image plane I_m/I_p is [155]

$$\frac{I_m}{I_p} = \frac{\Omega_m}{\Omega_p} = \frac{d_m^2}{d_p^2}\frac{f^2}{a^2}. \tag{6.5}$$

For the experimental parameters ($f = 250$ mm, $a = 287$ mm, $d_m = 25.4$ mm and $d_p = 0.3$ mm) the contrast enhancement calculated by equation (6.5) is 5440.

The spatial resolution can also be calculated. Taking the target to mirror distance a and mirror focal length f the image distance b_{mirror} can be found from the relation

$$\frac{1}{f} = \frac{1}{a} + \frac{1}{b_{\text{mirror}}}. \tag{6.6}$$

From the experimental parameters above the mirror-image distance $b_{\text{mirror}} = 1940$ mm. The magnification at the image plane $M = b_{\text{mirror}}/a = 6.75$. For a mirror-pinhole separation of 285 mm, the pinhole-image distance is $b_{\text{pinhole}} = 1655$ mm. The spatial resolution, or smallest resolvable distance Δl, is given by the Rayleigh-criterion

$$\Delta l = 1.22\frac{\lambda b_{\text{mirror}}}{d_p} \tag{6.7}$$

with wavelength λ (21.2 nm). The resulting spatial resolution from equation (6.7) $\Delta l = 0.021$ mm $= 21$ μm, taking into account the magnifying effect of the spherical mirror.

The interference fringes were created using a double Lloyd's mirror interferometer [120] (see section 3.3) placed between the spherical multilayer mirror and the CCD

detector. EUV radiation passing through the unablated sample target produced fringes by interference with EUV radiation passing through the target position where the heating beam was incident. For each measurement a reference shot was first recorded on the CCD detector, without the heating beam. This allows measurement of the phase shift induced in the EUV laser as it passes through the ablated sample target. The effect of the heating beam on the target over an area 245×145 μm^2 can be clearly seen in the interferometer images (figure 6.4). The

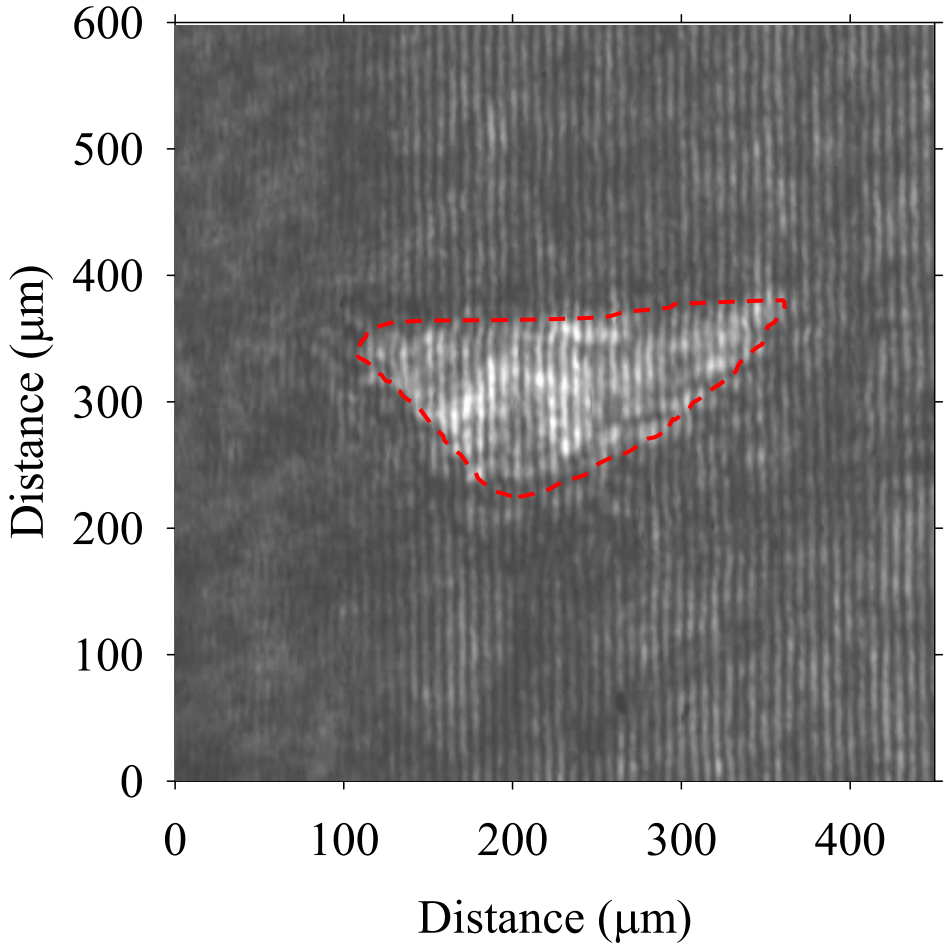

FIGURE 6.4: A sample interferogram showing the ablated 350 nm thick parylene-N target 400 ps after the peak of the heating pulse with the red dashed line showing the footprint of the heating pulse. The scale of the image is shown.

time of arrival of the heating pulse was adjusted with respect to the EUV laser to provide a temporal scan of the target ablation. The duration of the EUV probe

(200 ps) will have resulted in a certain amount of fringe blurring, and, as the fringe phase shifts associated with target irradiation shown in figure 6.4 are typically only up to ≈ 3 radians (half a fringe) a sensitive technique for their measurement was required. A Fourier transform technique of complex interferometer reduction, described in section 3.3.2 was used so that accurate fringe shift and intensity transmission measurements were made. Interferometry gave an accuracy of ± 10 nm in thickness measurements.

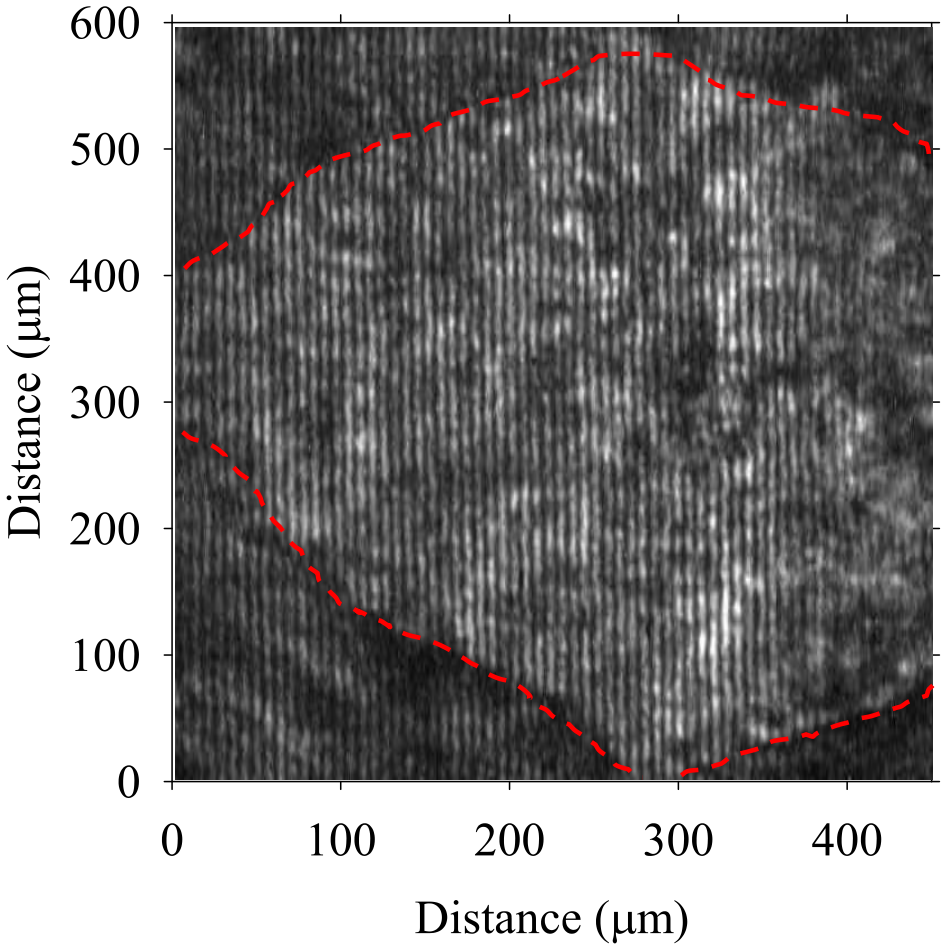

FIGURE 6.5: Interferogram taken through a hole within an aluminium target, demonstrating the direction of phase shift where there is no target/plasma present with the red dashed line showing the edge of the hole. In the image shown the phase shift from aluminium to vacuum (the hole) is seen to be towards the right, taken as a positive phase shift for the measurements.

Recording interferograms of target holes, as shown in figure 6.5, the phase shift was observed to move in the opposite (positive) direction to the situation with a plasma present, indicating refractive indices η below the solid parylene-N value when the plasma is present. Phase shifts seen within the region of the hole (of diameter ~ 600 μm), on the interferogram of figure 6.5 demonstrate some phase incoherence across the EUV beam. This phase inhomogeneity prevents detailed spatial imaging, however this is mitigated in the use of complex interferometry to spatially average over the ablation area [123, 124, 125].

6.4 Experimental analysis and h2d simulation

The 2D radiation hydrodynamic code h2d [22] has been used to model ablation of the planar CH plastic targets, predicting values of temperature, density and ionisation (see section 4.2 for a description of the h2d code). H2d has been used here with flux-limited electron conduction (flux limiter = 0.03 based on studies of electron heat transport at the experimental laser intensity [133]) with a Gaussian temporal and spatial laser profile and laser absorption assumed to be by inverse bremsstrahlung with resonance absorption at the critical density.

By examining the predicted plasma expansion from the h2d simulation (see figure 6.6), it is seen that the expansion of the probed plasma is approximately one-dimensional. Due to the large (300 μm) focal spot size, lateral transport of material is minimal and does not affect the transmission measurements [156]. The probe beam passes through an approximately constant areal density of material due to

the one-dimensional expansion, so that the probe transmission changes are solely due to changes in material opacity. Simulations indicate that at late times the level of 2D expansion of the cooling plasma is insufficient to raise the transmission above 0.45 (see figure 6.7).

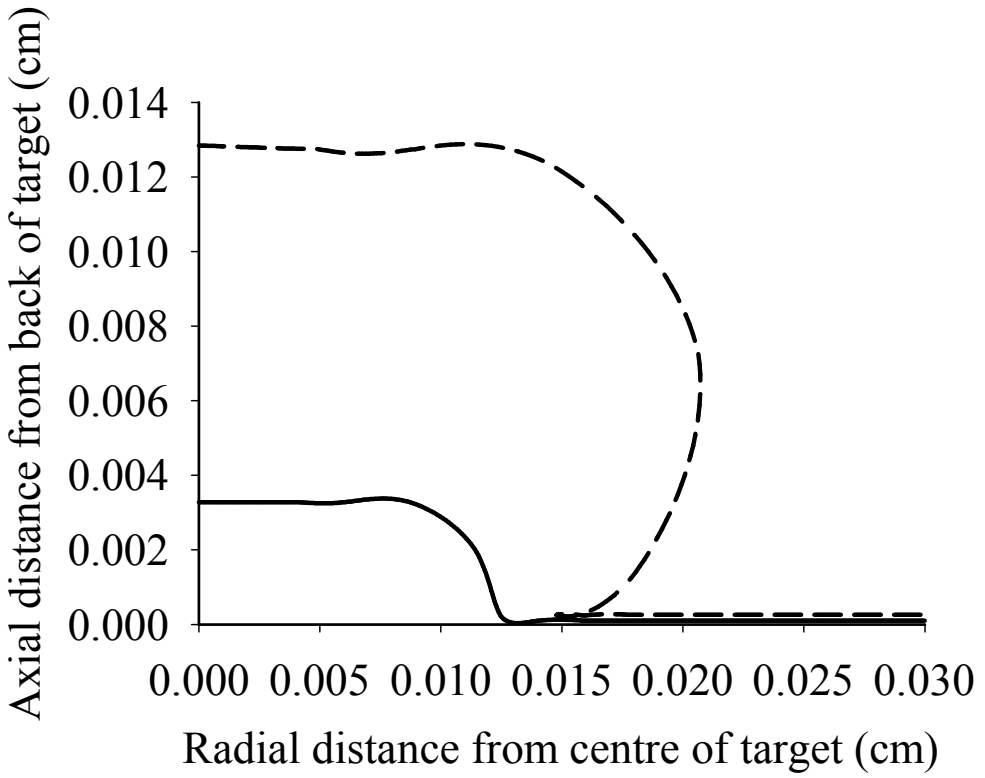

FIGURE 6.6: H2d simulated boundaries for the leading edge of the expanding CH plasma at 0 ps (solid line) and 400 ps (dashed line) from the peak of the heating beam. As laser ablation is occurring the expansion is close to 1D, in the direction normal to the target surface, which is also the axis of EUV probing. 400 ps from the peak of the heating beam lateral expansion has begun to lead to a departure from 1D behaviour of the plasma.

6.4.1 Transmission measurements

Plasma opacity values as calculated by the IMP code [106] together with the post processor developed as part of this work (section 4.3) allowed prediction of the spatially averaged transmissions. The experimentally determined transmission of the 21.2 nm probe beam through the irradiated target as a function of time is shown in figure 6.7 with results of the simulation superimposed.

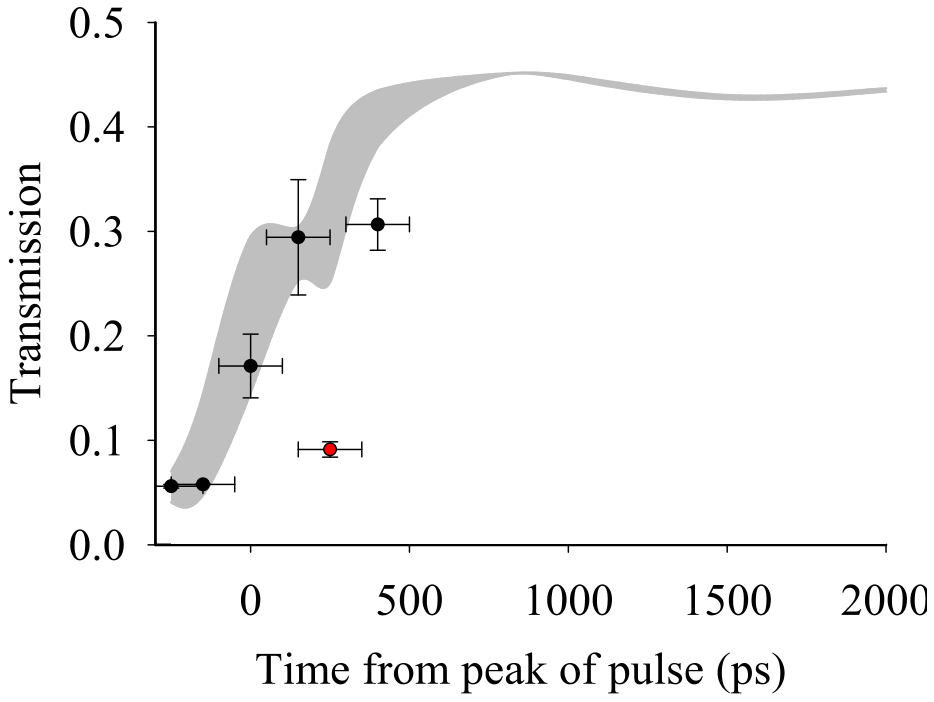

FIGURE 6.7: The transmission of 21.2 nm EUV laser pulses through a 350 nm thick parylene-N target irradiated by a laser of peak irradiance 10^{12} W cm^{-2} in a pulse of 300 ps duration as a function of time. Experimental transmission results are shown with error bars and the shaded region shows the range of simulated values over the experimental temporal resolution (200 ps) using the h2d code with IMP opacities. At late times, the simulation shows that the transmission remains approximately constant in time due to the approximately constant temperatures and areal densities of material.

The transmission of the EUV probe beam provides a measure of the rate of target ablation, as ablated plasma becomes close to transparent when the photon energy is less than the ionisation energy of the predominate ion species. Ablated plastic material becomes transparent due to a rapid increase in temperature causing ionisation to stages C^{3+} and higher with ionisation energy $E_{Z^*} \geq 64.5$ eV, where the photon energy (58.5 eV) is insufficient to enable photoionisation from the ground state. This effect can be seen in theoretical opacity values, such as those calculated by the LEDCOP or IMP codes (figure 6.8 and figure 2.8, section 2.2.2) where the transmission through the solid target rapidly approaches 1 as the temperature increases and density decreases.

Figure 6.7 shows that the transmission increases approximately uniformly during the target irradiation as ablation reduces the thickness of the remaining solid un-ablated target. The experimental and simulated results are in approximate agreement. An anomalous point at 250 ps heating pulse to EUV probe delay can be seen (highlighted in red). The origin of the point is not certain. However, an imprint from an extreme non-uniformity of the heating beam can be seen on the corresponding interferogram.

By assuming absorption occurs only in the unablated, solid region of the target the equation for transmission T (equation (2.5) $T = exp(-\sigma_s\ \rho\ z)$ section 2.1.1.1) can be used to calculate ablation depth z. Solid values for opacity σ_s [56] and density ρ have been used for the assumed unablated material, where the ablated material is taken to have negligible opacity (as indicated by e.g. figure 6.8). The

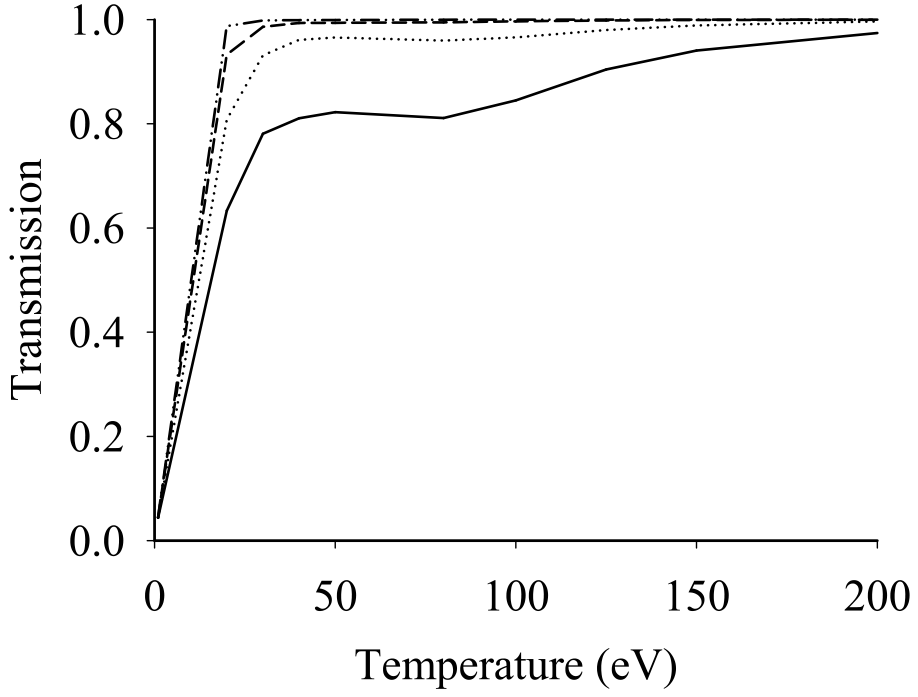

FIGURE 6.8: The transmission at 21.2 nm as a function of temperature calculated by the LEDCOP code [107] for a parylene-N target at various densities ρ but keeping the areal density constant as for solid parylene-N of 350 nm thickness: solid line - 1.11 g cm^{-3}, dotted line - 0.111 g cm^{-3}, dashed line - 0.0111 g cm^{-3} and dot-dashed line 0.00111 g cm^{-3}.

ablation depth z has been calculated from experimental transmissions with these assumptions and is shown in figure 6.9.

Laser intensity and wavelength dependent scaling laws for mass ablation rate $\dot{m}$ have previously been derived from large volumes of experimental data. For laser intensities below 10^{13} W cm^{-2} it has been found that $\dot{m} \propto I_a^{5/9}\lambda^{-4/9}$ with absorbed irradiance I_a and laser wavelength λ [52]. It was previously observed that absorbed irradiance $I_a \approx 90\%$ incident irradiance I in this regime, measured by detection of

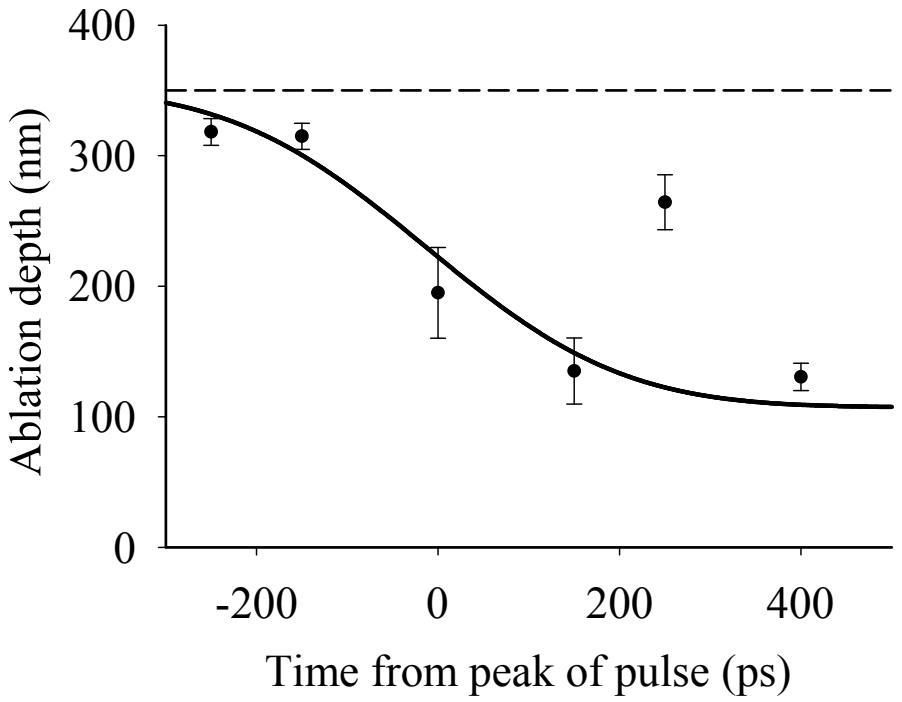

FIGURE 6.9: The ablation depth of the 21.2 nm EUV probe laser pulse through a 350 nm thick parylene-N target irradiated as for figure 6.7. Also shown is the depth predicted by a scaling law for mass ablation (solid line) and the original target thickness of 350 nm.

scattered light during target ablation [157]. A dependence on atomic number Z of $Z^{3/8}$ was also noted [52, 64]. In this lower intensity regime energy is presumed to be deposited further from the ablation surface, at the very edge of the critical surface, leading to a slower rate of ablation [52]. At higher intensities laser penetration is deeper and this, together with increased hot electron production, leads to faster rates of ablation.

By fitting the appropriate scaling law for the experimental intensity (10^{12} W cm^{-2}) the mass ablation rate $\dot{m}$ was found to vary as

$$\dot{m} = (4500 \pm\ 500) \times I^{5/9} \lambda^{-4/9} Z^{3/8}. \tag{6.8}$$

To find the depth of ablation z, as a function of time, a temporal Gaussian profile has been taken for the laser irradiance and as $\dot{m} = \rho_{\text{solid}} z/\Delta t$ with solid target density ρ_{solid} over time Δt the depth is readily calculated. The depth derived from the scaling law of equation (6.8) is shown in figure 6.9. The mass ablation rate at the peak of the 438 nm heating pulse was determined as $(6.3\pm 0.7)\times 10^4$ g s^{-1} cm^{-2}. This is consistent with previously measured values of mass ablation rate for laser intensities $\approx$ 10^{12} W cm^{-2} where a rate of 8.46×10^4 g s^{-1} cm^{-2} is predicted for a 350 nm laser and 4.14×10^4 g s^{-1} cm^{-2} for a 530 nm laser [158].

At higher irradiance ($> 10^{14}$ Wcm^{-2}) the same electron preheating that leads to early onset of emission for buried layer laser ablation studies, as described in section 1.2.2, may also lead to changes in opacity for target material beyond the critical density surface. However, such effects will not occur for the irradiances considered here ($\sim 10^{12}$ Wcm^{-2}). From the h2d generated model of ablation, temperature and density profiles have been extracted and are presented in figure 6.10 along with IMP opacities [106] and transmission profiles from post processing.

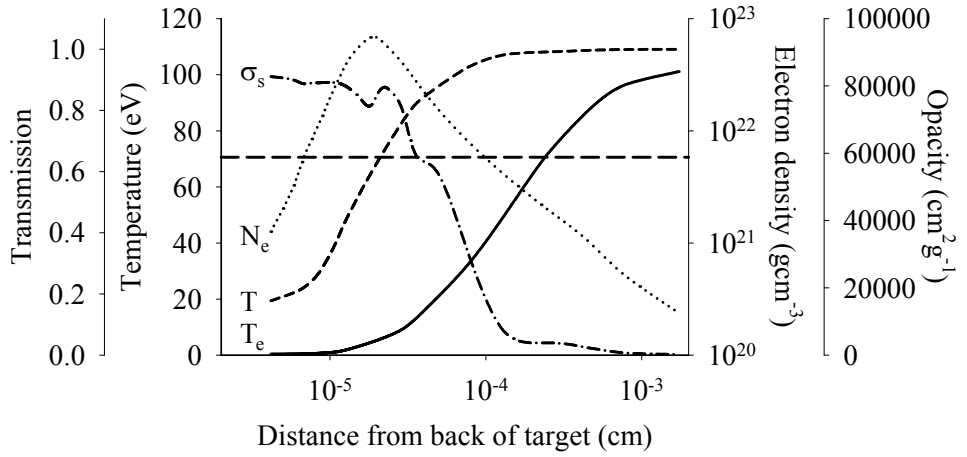

FIGURE 6.10: Temperature T_e (solid line) and electron density N_e (dotted line) profiles through the target from h2d simulation together with IMP opacity σ_s [106] (dot-dashed line) and transmission T (short dashed line) profiles calculated from post processing of h2d simulated data. The data presented is for 0 ps from the peak of the heating beam at the centre of the target. Also shown is the critical density (long dashed line) for the 438 nm heating beam. The irradiating and EUV probe lasers are both incident on the front of the target.

As is expected the steepest gradients for temperature, opacity and transmission occur in the region of critical density. Beyond this region, towards the back of the target, the temperature and transmission profiles level off. The opacity plateaus, at the solid value, and drops rapidly at lower densities, providing evidence that the assumption of constant opacity in the solid, unablated material and zero contribution from ablated material for calculating ablation depth is valid for ablation at this intensity.

6.4.2 EUV phase measurements

To obtain code predicted values of phase shift a model of refractive index is required. If an expansion with real plasma refractive index (given by equation (2.11) $\eta = (1 - N_e/N_{\text{crit}})^{1/2} \approx 1 - N_e/2N_{\text{crit}}$, for electron density N_e and critical density

N_{crit}) was assumed, the experimentally measured fringes shifts would not occur. The total phase shift comes from integrating over the entire sample in the direction of probing, effectively integrating $\int N_e dz$. For a 1D expansion in the limiting case of full ionisation, the phase shift will remain constant, with lower degrees of ionisation resulting in positive phase shifts. However, negative phase changes in the probing beam relative to the reference beam passing through the solid material are seen (figure 6.11), indicating that the refractive index η of some of the heated material has dropped below the plasma and the solid unheated target refractive index.

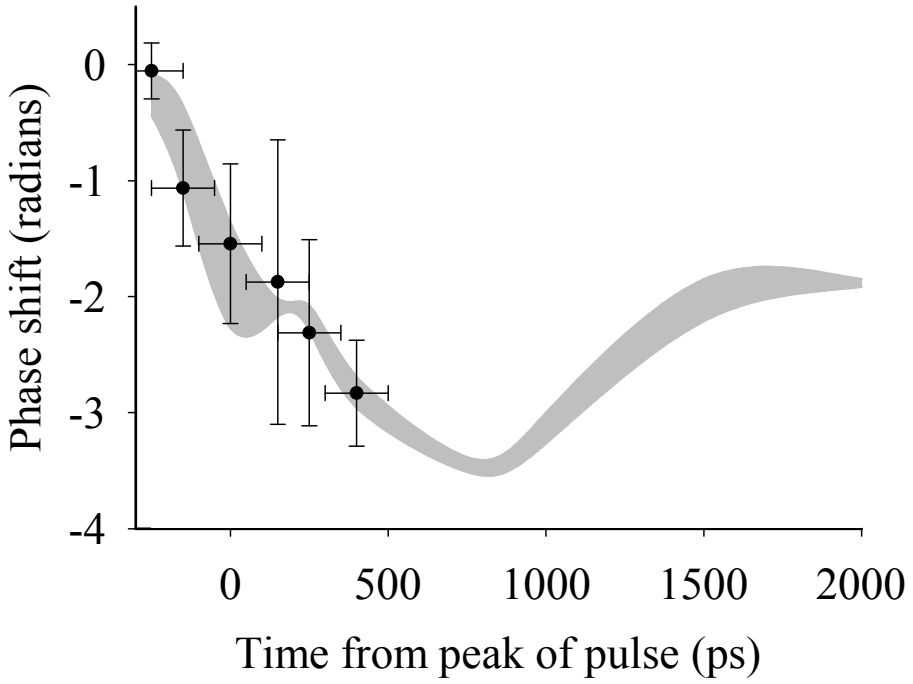

FIGURE 6.11: The phase shift of the 21.2 nm EUV probe laser pulse through a 350 nm thick parylene-N target irradiated as for figure 6.7. Negative phase shift as shown implies refractive indices in the probed material less than η_{solid}.

Phase shift measurements were also taken for a 200 nm thick parylene-N target (figure 6.12). For the thinner target smaller negative phase shifts are still seen,

but with values close to the experimental error.

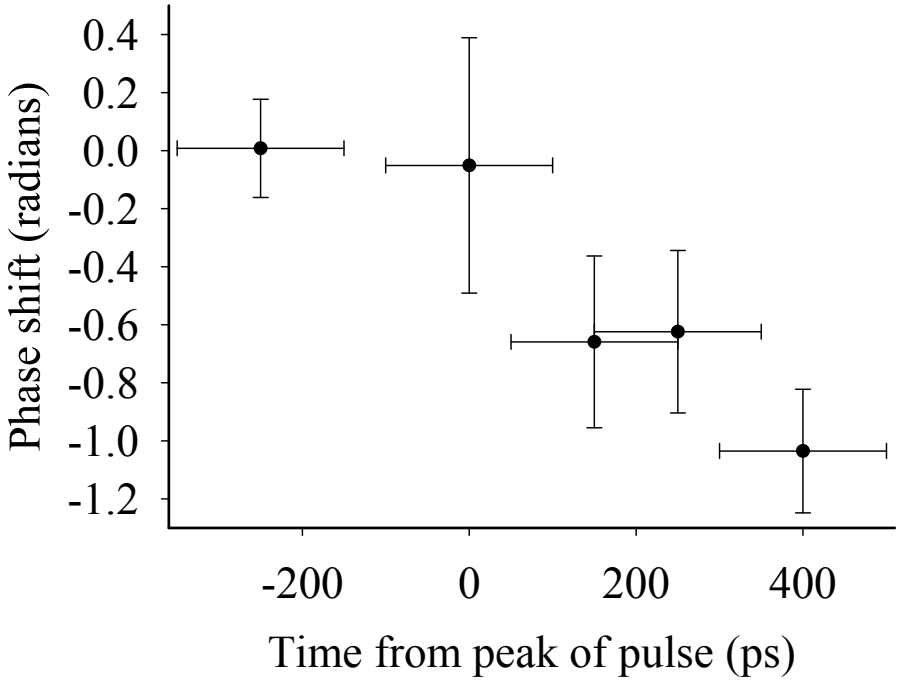

FIGURE 6.12: The phase shift of the 21.2 nm EUV probe laser pulse through a 200 nm thick parylene-N target irradiated as for figure 6.11.

A model for the refractive index of CH plastic has been determined using the Kramers-Kronig relationship as outlined in section 2.3.2, linking the atomic scattering factors $f_1(E)$ and $f_2(E)$ as a function of photon energy E. The values of $f_1(E)$ and $f_2(E)$ are related to the complex index of refraction ($\eta^* = 1-\delta-i\beta$), the number density of CH ions N_i and critical density N_{crit} such that $\delta = f_1 N_i/(2N_{\text{crit}})$ and $\beta = f_2 N_i/(2N_{\text{crit}})$ [56] (see e.g. [159] for calculations relevant to plasmas). Equation (2.13) as follows

$$f_1(E) = \bar{Z}^* + \frac{2}{\pi} P.V. \int_0^\infty \frac{f_2(\varepsilon)\varepsilon d\varepsilon}{E^2 - \varepsilon^2},$$

has been used to calculate the refractive index η, where the solution is obtained by taking the principle value (P.V) of the integral.

Work by Nilsen et al. [160] studying low-density, warm carbon plasmas has shown that there are no refractive index effects due to absorbing lines (bound-bound transitions) in the region of the EUV laser probing photon energy (58.5 eV). Consequently, the refractive index of the heated target material is determined assuming that bound-free and free-free absorption in CH plastic dominate in the Kramers-Kronig integration (equation (2.13)). The atomic scattering factor f_2 has been calculated from bound-free (photoionisation) cross sections σ using the Los Alamos Atomic Physics code [161], shown in figure 6.13, where $f_2 = \sigma/(2\lambda r_0)$ with classic electron radius r_0.

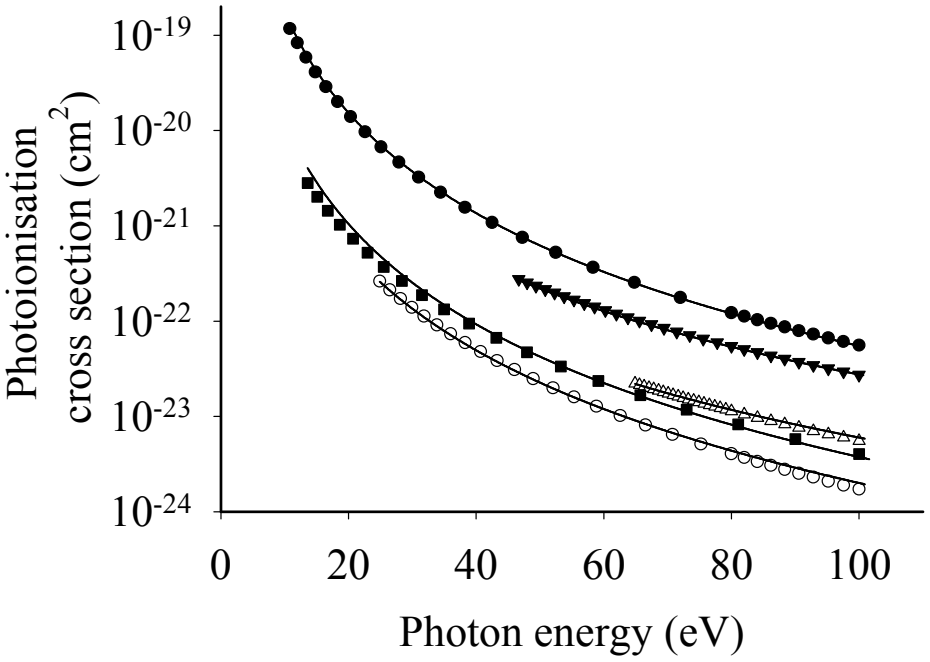

FIGURE 6.13: Los Alamos Atomic Physics code photoionisation cross sections for a CH plasma [161], with expressions of the form $1/(E)^{3-3.5}$ fitted to them (solid curves). Filled circles - C^+ (E_{Z^*} = 11.26 eV), filled squares - H^+ (E_{Z^*} = 13.6 eV), open circles - C^{2+} (E_{Z^*} = 24.38 eV), filled triangles - C^{3+} (E_{Z^*} = 47.89 eV) and open triangles - C^{4+} (E_{Z^*} = 64.49 eV).

For photons of energy E greater than the ionisation energy (E_{Z^*}) of an ionisation of Z^* the cross sections can be seen to vary as $1/(E)^{3-3.5}$, allowing an analytical solution of equation (2.13) to be found. Considering bound-free and free-free absorption, we obtain using the Kramers-Kronig relation for $E > E_{Z^*}$ the following more complete expression for plasma refractive index

$$\eta(E) = 1 - \frac{1}{2N_{\text{crit}}}\left[\bar{Z}^* N_i + \frac{2}{\pi}\sum_{Z^*} N_{i,Z^*} P.V. \int_{E_{Z^*}}^{\infty} \frac{f_{2,Z^*}(\varepsilon)\varepsilon d\varepsilon}{E^2 - \varepsilon^2}\right] \tag{6.9}$$

where N_i is the number density of CH ions, $\bar{Z}^*$ is the number of free electrons per CH ion, N_{i,Z^*} is the number of ions associated with an ionisation stage Z^*, $f_{2,Z^*}(\varepsilon)$ is the corresponding atomic scattering factor and the summation is over all ionisation stages. When calculating $f_{2,Z^*}(\varepsilon)$ the population of ions in each ionisation stage is required. H2d simulation provides average ionisations, from which the populations in the two adjacent level are calculated, assuming limited overlap between stages as is seen in studies of carbon ion populations [162, 163]. The contributions of each ionisation stage to $f_{1,Z^*}(E)$ values ,temporarily ignoring the effect of free electrons, are compared in figure 6.14. In the absence of any bound electrons f_1 equals the number of free electrons per ion [116] therefore for figure 6.14, with this contribution not plotted, $f_1 \rightarrow 0$ as $E \rightarrow \infty$.

Much of the contribution to the negative phase shifts observed is found to arise from bound-free absorption in lowly ionised carbon (figure 6.14 solid line). Using equation (6.9), the electron density, electron temperature and ionisation abundance data from h2d simulations has been post processed in order to evaluate refractive indices $\eta(E)$ in each zone and then evaluate the phase shifts for our

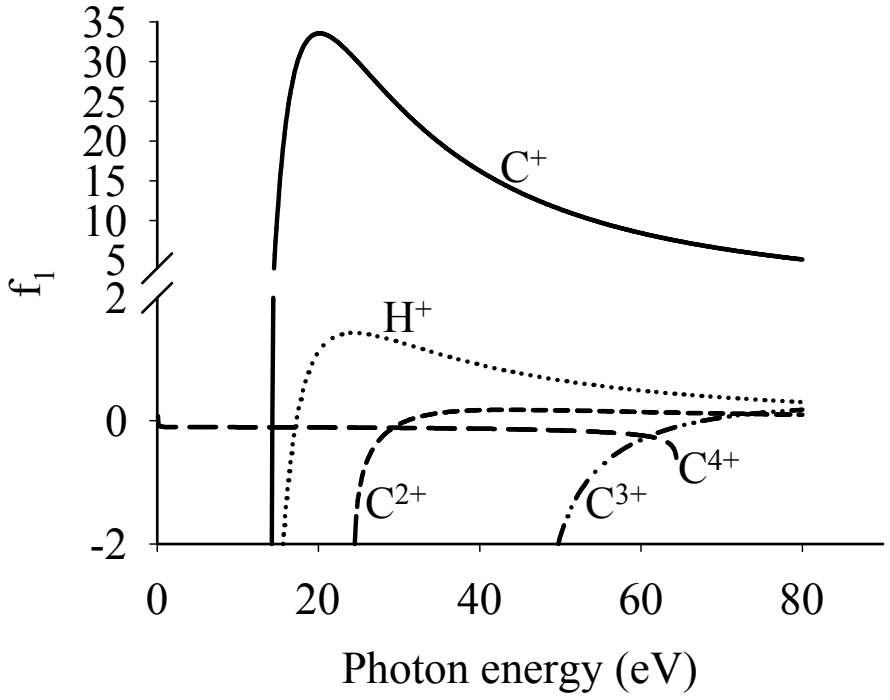

FIGURE 6.14: Atomic scattering factors $f_{1,Z^*}(E)$ for each ionisation stage, calculated by equation (2.13) but temporarily neglecting the contribution to the real atomic scattering factor from free electrons. Solid line - C^+, dotted line - H^+, short dashed line - C^{2+}, dot-dashed line - C^{3+} and long dashed line - C^{4+}. Note the break in f_1 axis.

EUV interferometry experiments (shown together on figure 6.11), using equation (2.10) given in section 2.3. The low values of refractive index observed in this experiment act as a signature of the presence of lowly ionised material (principally C^+ - see figure 6.14) at high-density between the absorption and ablation surface.

Using equation (6.9) and assuming an LTE variation of the abundance of ionisation stages Z^*, we can evaluate the refractive index as a function of temperature (figure 6.15). At low-ionisation the calculated refractive index differs greatly from the

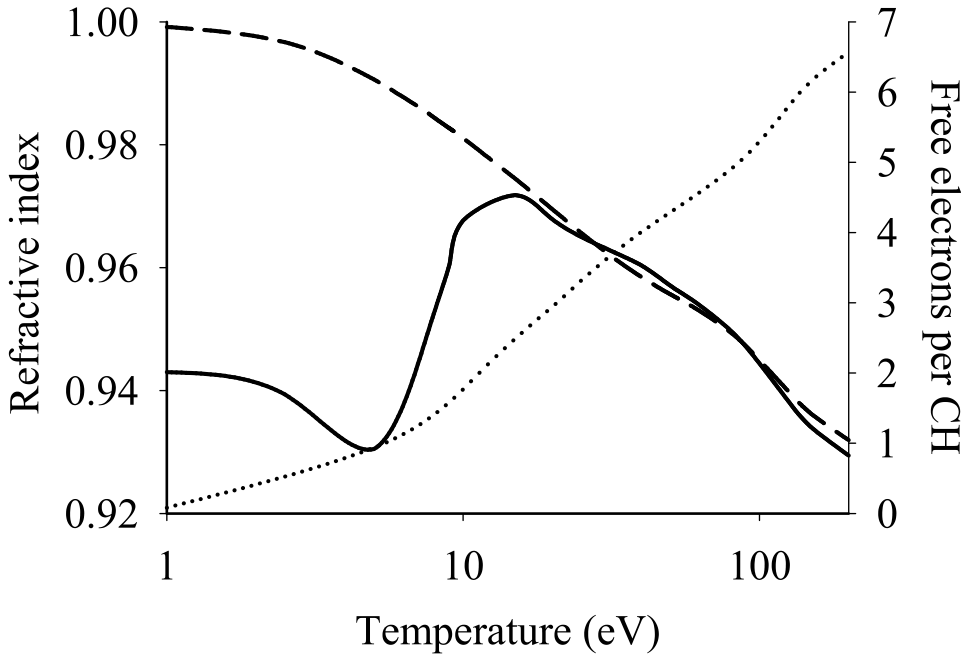

FIGURE 6.15: The refractive index at 21.2 nm for solid density plastic (parylene-N) as a function of temperature calculated from Los Alamos Atomic Physics code photoionisation cross sections and using the Kramers-Kronig relationship to relate real and imaginary atomic scattering factors (solid line). The number of free electrons per CH ion (dotted line) and the real plasma refractive index associated solely with free electrons (dashed line) are also shown.

traditional plasma refractive index model.

Sample calculations of the procedure for evaluating $\eta(E)$ agree with results by Nilsen et al. [116, 160] carried out for low-density (10^{20} ions cm^{-3}) carbon plasmas at temperatures of 2, 5, 10 and 20 eV (see figure 6.16).

To create a versatile model for calculation of the material refractive index many

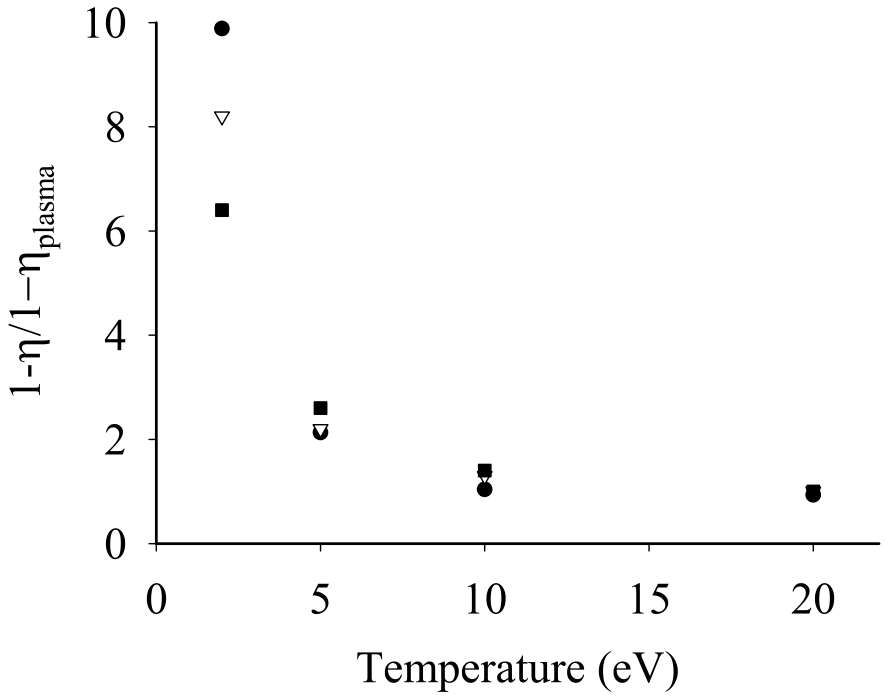

FIGURE 6.16: The model for refractive index presented in this work has been used to calculate values of refractive index for low-density (10^{20} ions cm^{-3}) carbon plasmas, presented for comparison with results by Nilsen et al. [116, 160] and the OPAL code (see section 2.2.2 [108]). Filled circles - refractive index model, open triangles - Nilsen et al. [116, 160] and filled squares - OPAL [108].

more transitions may need to be considered, analogous to models of opacity (section 2.2.2). For example, in a recent study the $2s - 6p$ bound-bound transition in C^{3+} (nominally 21.24 nm) was found to affect transmission measurements at 21.2 nm [164], although for a higher temperature plasma than seen here. The presence of the line may also alter the refractive index. However, the C^{3+} line centre and EUV lasing line (21.217 nm, see [165]) match very well making it possible that the refractive index perturbation due to the C^{3+} line is minimised, as the Kramers-Kronig refractive index effect due to an absorption line is zero at line

centre.

6.4.3 H2d simulated profiles

H2d simulated data has been post processed to provide transmissions and phase shifts at EUV wavelengths, for comparison with experiment. The evolution of target ablation, and resulting effect on the properties of the plasma, have been investigated in this way. Reasonable agreement between experimental and simulated data is seen (see figures 6.7 and 6.11), providing confidence in the model as an accurate representation of the ablation of the parylene-N target. Temperature and electron density profiles have been selected, at the centre of laser beam irradiance along the target normal, this being the direction of EUV probing. The opacity, represented by specific cross section σ_s and based on the IMP opacity code [106], and refractive index η, using the Los Alamos photoionisation cross sections as explained above, have been calculated through post processing. Comparisons are made in figures 6.17 to 6.22.

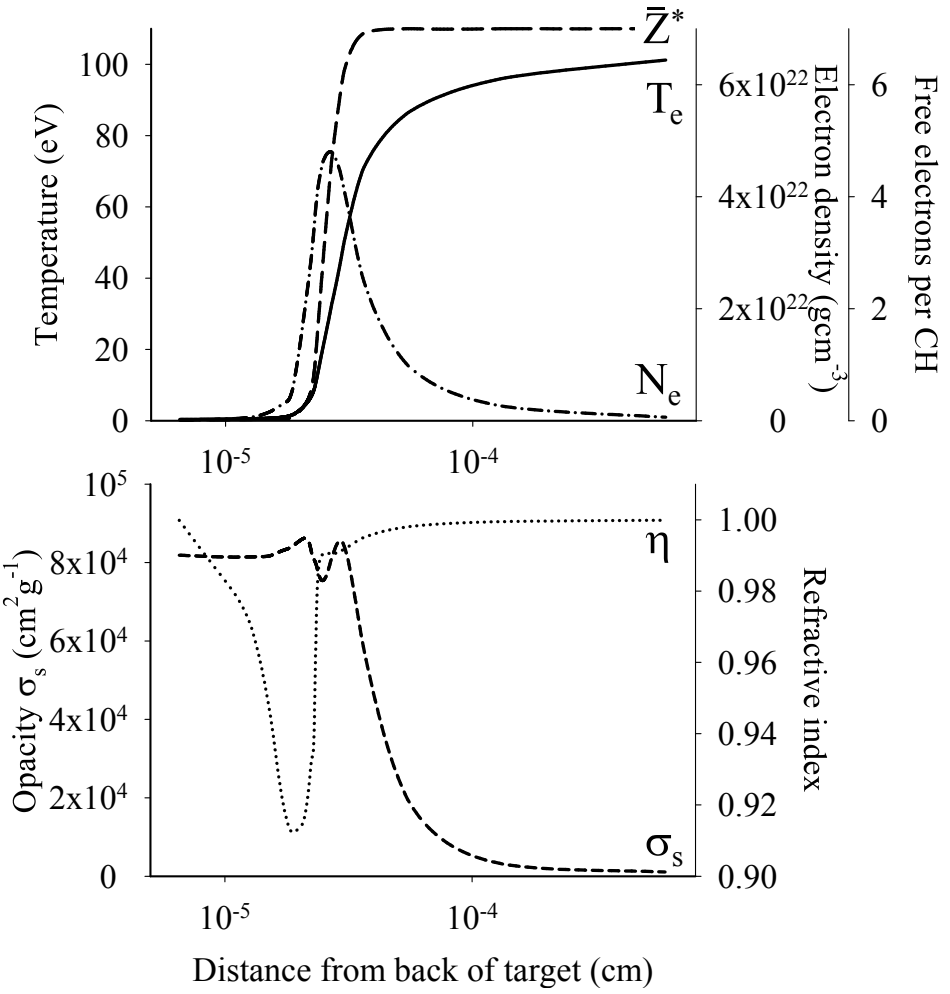

FIGURE 6.17: H2d simulated temperature (solid line), electron density (dot-dashed line) and free electrons per CH ion (long dashed line) profiles. Also shown are the opacity (as σ_s, short dashed line) and refractive index (dotted line) at the probe wavelength 21.2 nm. The data presented is for 150 ps before the peak of the heating beam at the centre of the target. The irradiating and EUV probe lasers are both incident on the front of the target.

At early time (figure 6.17) the peak in density and temperature gradient correspond to the same region, indicating laser absorption at the critical surface. The ionisation rises rapidly in this region. The low-temperature material at the back of the target is at the solid value of opacity [56], and has been shown to dominate the transmission of the EUV probe. The minimum refractive index occurs for ionisations between 0 and 1, i.e. un-ionised and singly ionised carbon.

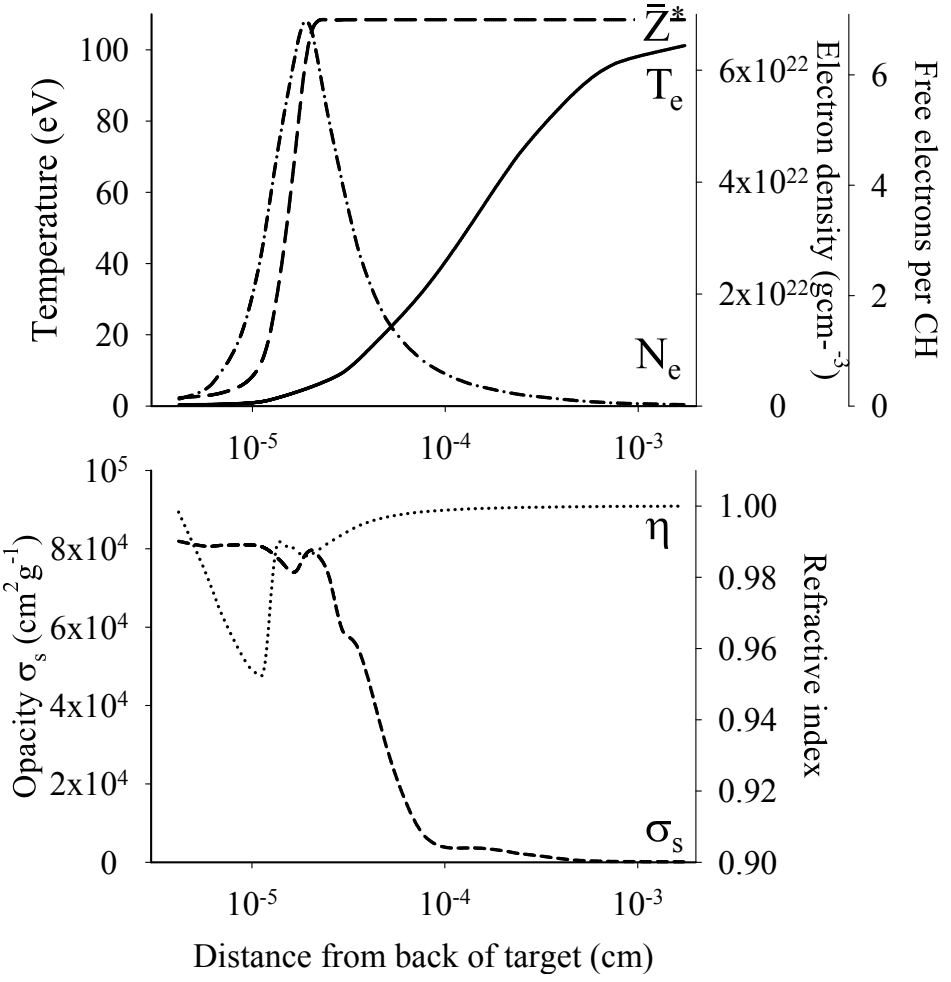

FIGURE 6.18: As figure 6.17, 0 ps from the peak of the heating beam. Shown are temperature (solid line), electron density (dot-dashed line), free electrons per CH ion (long dashed line), opacity (short dashed line) and refractive index (dotted line).

Figure 6.18 shows h2d simulated profiles at the peak of the heating pulse. The peak in density and rise in ionisation still occur in the same region, however the temperature gradient has reduced due to inverse bremsstrahlung in the expanding plasma. The opacity is lowest for the hot, rare plasma which is now fully ionised and so has no contribution to absorption from bound-bound or bound-free transitions. The refractive index takes on the plasma value η_{plasma} in this region. The dip in refractive index occurs for the cooler, denser plasma and corresponds

to a region of constant opacity. Different processes in the plasma dominate the measured phase shift and transmission data.

During post-processing of h2d simulated data, the refractive index is calculated for each zone. The phase shift, relative to vacuum, has been calculated using both the model of refractive index given by equation (6.9) and the traditional plasma refractive index of equation (2.11), and is compared in figure 6.19.

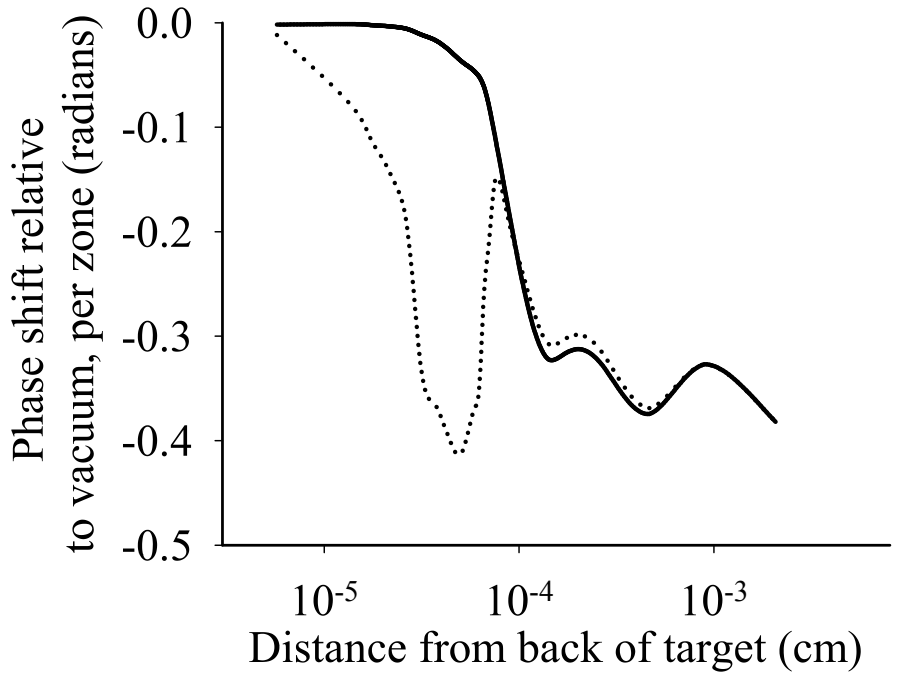

FIGURE 6.19: Comparison between modelled phase shifts within each zone taken from equation (6.9) (dotted line), where bound-free transitions are included, and using only the plasma refractive index from equation (2.11) (solid line). The data presented is for the peak of the heating beam at the centre of the target.

In the coronal region the plasma is fully ionised and is described well by the plasma refractive index. In the cooler, denser regions towards the back of the target a more rigorous approach must be taken to reproduce the experimentally observed phase shifts.

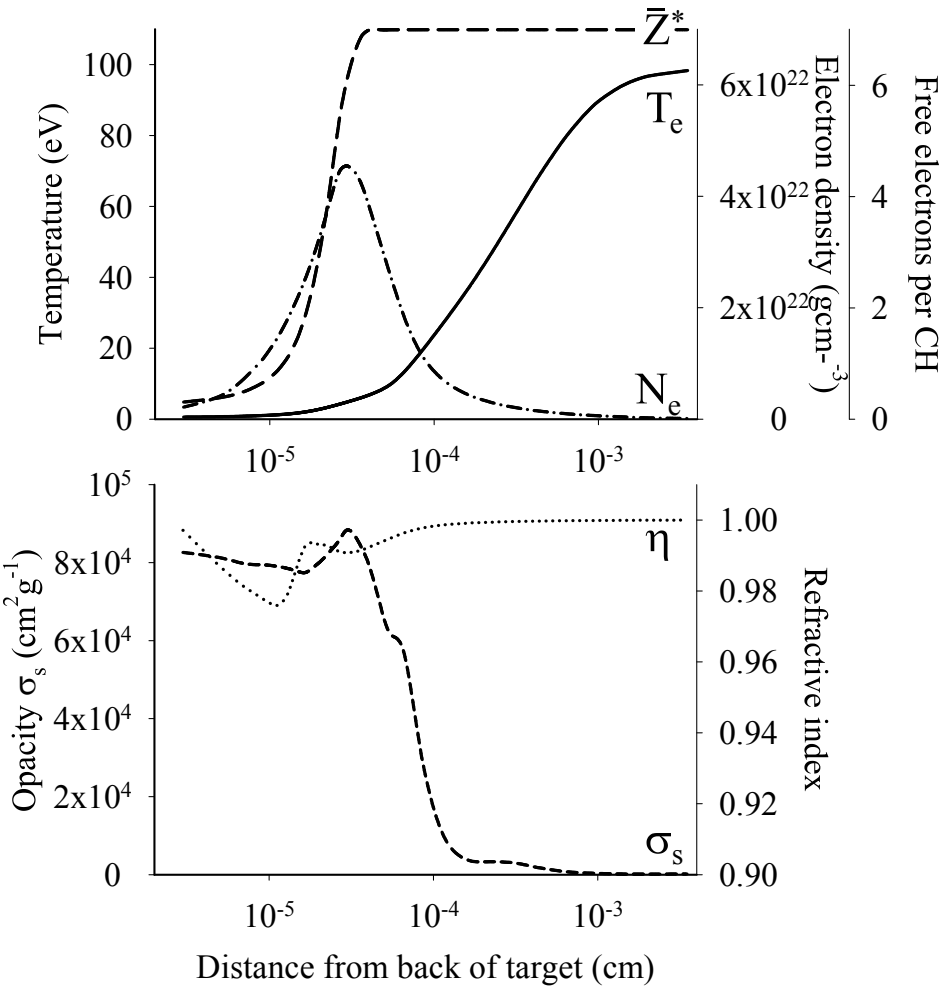

FIGURE 6.20: As figure 6.17, 150 ps from the peak of the heating beam. Shown are temperature (solid line), electron density (dot-dashed line), free electrons per CH ion (long dashed line), opacity (short dashed line) and refractive index (dotted line).

At later times (figure 6.20) past the peak of the heating pulse the plasma continues to expand and so the amount of C^+ material increases leading to a drop in the probe phase (figure 6.11). As explained in section 2.3 despite the increase in refractive index to above the solid value, the total phase shift can still be negative, as it also depends on the level of plasma expansion. 2D expansion and recombination of C^+ material can be expected to ultimately result in the refractive index approaching unity.

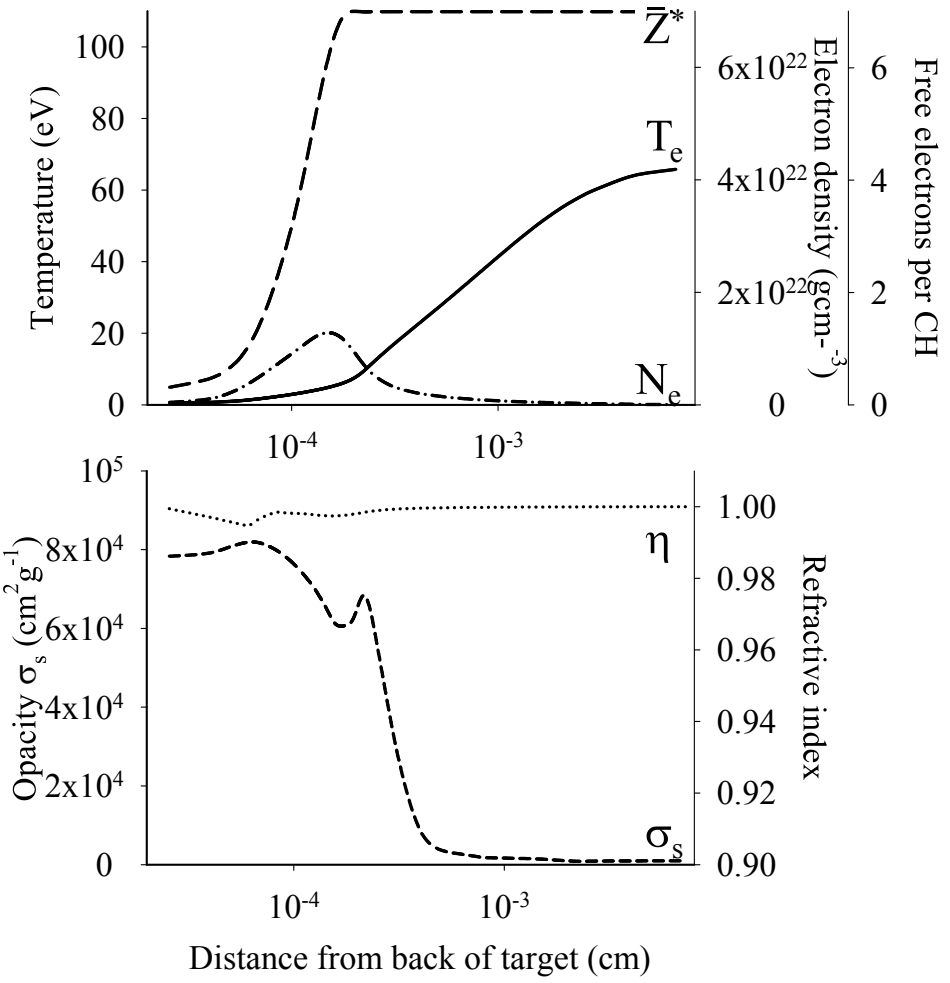

FIGURE 6.21: As figure 6.17, 400 ps from the peak of the heating beam. Shown are temperature (solid line), electron density (dot-dashed line), free electrons per CH ion (long dashed line), opacity (short dashed line) and refractive index (dotted line).

In figure 6.21 profiles for 400 ps after the peak of the heating pulse show significant expansion of plasma from the original 350 nm (3.5×10^{-5} cm) target thickness. By this point the intensity of the heating beam has dropped to less than 1% of the peak value (based on a Gaussian temporal profile). The high-temperature and low-density component in the expanding coronal plasma has maintained the full ionisation. Absorption at the critical surface no longer dominates the target evolution.

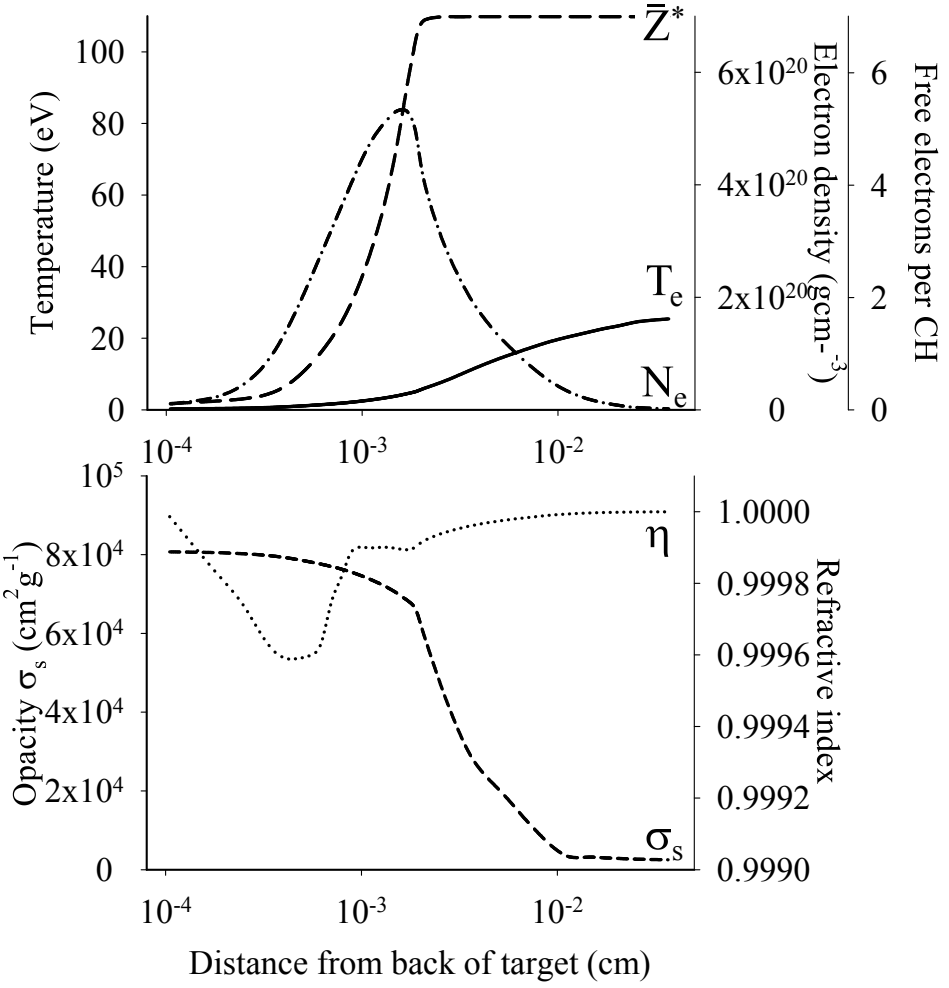

FIGURE 6.22: As figure 6.17, 2 ns from the peak of the heating beam. Shown are temperature (solid line), electron density (dot-dashed line), free electrons per CH ion (long dashed line), opacity (short dashed line) and refractive index (dotted line). Note the change in scale on the lower plot (electron density and refractive index).

Finally 2 ns after the peak of the heating beam (figure 6.22) the density and temperature have dropped significantly. Due to the drop in temperature, the opacity of the expanding plasma rises slightly, as the contribution from electron scattering decreases. The refractive index (shown on an expanded scale) still experiences a dip brought on by lowly ionised carbon, but as the density is so low the value is much closer to the vacuum value of 1. A slow increase in transmission has occurred as the plasma expands and, as the amount of lowly ionised material

reduces, the phase shift has also increased. These effects should then continue in time, however in experimental laser ablation studies slow shocks eventually lead to departure from ideal behaviour and target break-up.

6.5 Conclusion

EUV interferometry has been demonstrated for measurement of the ablation of solid target material (associated with an increase in probe beam transmission) and the presence of low degrees of ionisation (associated with refractive indices below the solid target and plasma values) in the region of warm dense plasma between the critical density and ablation surface in laser-plasma interactions. The critical density to ablation surface region determines much of the physics of laser-plasmas important in inertial fusion and other studies. EUV interferometry has been employed in the longitudinal direction (close to normal to the target surface) as a technique for measuring ablation and levels of ionisation in the difficult to diagnose critical to ablation surface region. Future work should apply this technique alongside higher heating pulse intensities, in order to measure the effect of hot electron production in laser ablation relevant to ICF pellet compression.

Chapter 7

Conclusions

The work of this thesis has shown how extreme ultraviolet (EUV) wavelength radiation can be used to diagnose laser ablated targets at densities too high for longer wavelength probes. As shown, the opacity generally decreases with increasing photon energy of the probing x-rays and the refractive index approaches unity. At EUV wavelengths the signature effects of high absorption and refractive index variation from unity enable accurate probing of ablation and material heating, with detail that is lost at higher photon energies.

The first two chapters presented the history and motivation behind experiments based on EUV backlighting. Methods for spatially resolving laser ablated plasmas were considered, with transmission measurements for determining laser ablation rates, material opacity and refractive index being the goal. The mechanisms of

inertial confinement fusion (ICF), this being of great interest for future power generation, have been summarised with emphasis on the need for continued studies of instability formation and hot electron production. Iron has been highlighted as a key element in solar opacity models and potentially ICF, for which greater experimental study is required to allow benchmarking of theoretical opacity codes.

Chapter 3 detailed the diagnostics used to further this work, including a double Lloyd's mirror for EUV interferometry together with the method of complex interferometry for analysis. The experimental methods used to probe an iron opacity target with a broadband EUV backlighter were introduced, where a flat field spectrometer was found to be effective for measuring transmission through the target.

In addition to experimental methods, two radiation hydrodynamic codes, POLLUX [49] and h2d [22], have been utilised. The physical models included in these codes were laid out together with the post processor developed to efficiently calculate simulated transmissions from the large volumes of code generated data, thus allowing direct comparison with experimentally measured EUV transmissions. The theoretical opacity codes, IMP [106] and LEDCOP [99, 107], described in chapter 2, were used to provide opacities for the transmission calculations.

A computational experiment, undertaken using the POLLUX code, studied the evolution of the Rayleigh-Taylor instability (RTI) under conditions relevant to ICF. The small changes in transmission that can be detected during EUV probing allow for a sensitive technique. By looking at the transmission and change in areal density it was seen that solid density, warm material dominates the absorption for longitudinal EUV radiography, therefore material opacity must be known and

taken into account. Shorter wavelength modulations of laser irradiated targets were seen to be smoothed by lateral transport, with this occurring significantly for modulation wavelengths less than ~ 50 μm.

H2d simulations of an iron opacity experiment were presented to establish the feasibility of using a single pulse to both heat and probe an iron layer, ultimately to provide benchmarks for solar opacity models. It was found that large temperature and density gradients would be expected under the experimental conditions, which would have to be reduced to provide a more uniform target for probing.

Simulations of laser heating of buried iron layers, tamped by plastic, also demonstrated the need for improved experimental design in reducing temperature and density gradients, even for thin (50 nm) iron layers. Increased tamping of the target material and improved laser intensity contrast between the main and amplified spontaneous emission-borne prepulse have been shown to reduce these gradients, by increasing confinement of the buried layer and preventing formation of a long scale length preplasma with which the main heating pulse will interact. By improving the intensity contrast, for example by insertion of a plasma mirror [87], the critical depth moves closer to the buried layer. Heating will occur more rapidly, within the hydrodynamic timescale for expansion (first few ps), allowing time for probing before the formation of large density gradients.

The simulated transmission through a heated iron opacity target was calculated at different wavelengths across the broadband EUV spectrum. It was shown how broad and narrowband EUV backlighters can be used to obtain benchmark data for opacity codes, where absorption features must be considered. Differences in

transmission calculated using the IMP and LEDCOP opacity codes were found, but for this work were within the experimental error.

The first demonstration of a viable EUV laser in 1985 [33], producing a coherent, bright source of EUV photons allowed interferometry at EUV wavelengths. It has been proposed in this thesis (chapter 6) as a diagnostic of the region of 'warm dense matter' between the critical and ablation surfaces in a laser ablated target. EUV inteferometry was demonstrated in a measurement of the ablation of solid target material, where the ablation rate of a CH plastic target under a 438 nm, 10^{12} Wcm^{-2} laser was found to be in agreement with previous studies. By probing with a bright, EUV wavelength source for interferometry in the longitudinal direction, the region of warm dense plasma between the critical density and ablation surface in a laser-plasma has been diagnosed, at densities two orders of magnitude higher than studied previously. A model for the refractive index of a CH plasma was proposed, based on Los Alamos Atomic Physics code absorption cross sections [161] and the Kramers-Kronig relation between absorption and dispersion of radiation in a plasma. The presence of low degrees of ionisation was concluded to be the origin of phase shifts not predicted by the plasma model of refractive index. The model put forward as part of this work was found to be in agreement with models by Nilsen et al. [116, 160] in the limit of a lower density carbon plasma. Extensions to this model would include increasing the number of bound-free transitions considered in calculation of the absorption cross sections, on which it is based.

The majority of the work of this thesis has considered lower intensity laser ablation

($10^{12} - 10^{14}$ Wcm^{-2}), applicable to the initial stages of direct-drive ICF. It will be the aim of future studies to apply the technique of longitudinal EUV interferometry alongside higher heating pulse intensities, in order to measure the effect of hot electron production in laser ablation relevant to ICF pellet compression. As the plasma temperature increases, so will the target self emission and backlighters will need to become brighter. It is also desirable to probe over shorter durations for interferometry and imaging, thereby removing image blur and capturing the plasma in a single state, within hydrodynamic timescales. In chapter 1 x-ray free electron lasers (FELs) were introduced as a means to achieve this, where the advantages of probing at EUV wavelengths are combined with the higher brightness and temporal resolution that have now been demonstrated [60].

Appendix A

POLLUX simulation input file

The input parameters for POLLUX simulation are specified as in the following sample file. POLLUX simulation results appear in chapter 5. The key components of the input file are noted.

```
ch 18rt
$ NEWRUN
y0=0.0, y1=100.0E-4, dy=1.E-4, $ The Eulerian grid is characterised in y − z
planar geometry
ty0=0.0, ty1=100.0E-4,

z0=-50.0e-4, z1=150.0e-4,
z0a=-50.0e-4, zab=0.0e-4, dza=1.0e-4, zbc=150.0e-4, dzb=1.0e-4,
tz0=0.0e-4, tza=10.0e-4, rhoa=1.11, $ The target thickness is defined within
```

the grid

```
pplfil='18rt.ppl',
fonfil='18rt.tx',
fonfmt=2,
idim=0, rhoamb=0.0001, f=12.0, z=6.0, $ The target material is chosen by
```

specifying the atomic mass and number, here $^{12}_{6}$C

```
windop=t, wndcel=1, wndrho=0.05,
totime=3.0e-9, tout=100.0e-12, dt=0.1e-12,
tinit=273.0, anomt=0.06, $ The electron flux limiter of 0.06 is specified
lason=t, power=5.e14, $ The laser is called, described by intensity, wavelength,
```

focal width and temporal pulse shape. The modulation is applied, given by a modulation wavelength and amplitude (a fraction of the total power)

```
amp=0.2, xamda=100.e-4,
freql=0.35,
xrdon=f,
pshapn=4,
pulseh(1)=0.07, pulset(1)=0.0,
pulseh(2)=1.0, pulset(2)=250.0,
pulseh(3)=1.0, pulset(3)=1000.0,
pulseh(4)=0.0, pulset(4)=1250.0,
sumdmp=50.0E-12, sumfmt=0,
trkpkp=t, topref=t, botref=t, dtmax=2.0e-12,
```

`stub='18rt', opfile='../optemp/chplk2.tfo',` $ The CH IMP opacity file is invoked

`probeg=9,` $ The probe energy group is chosen as 9, corresponding to a probe energy of 90 - 100 eV

$ `END`

Appendix B

H2d simulation input file

Following is an h2d simulation input file, the results of which are included in chapter 6. H2d simulation results are also included in chapter 5. The key, user specified, parts of the input file are noted.

```
Ablating plastic target.  0.35um.

mesh 1 1 31 31 100.e-4 0.149965 400.e-4 0.150000 $ The Lagrangian mesh is defined in r − z cylindrical geometry
ratio 1 1 1 31 1.0
spacing 1 1 31 31 1 0
region 2 2 31 31 1 1.11 2.57e-5 $ The target material is defined as solid density, room temperature carbon and hydrogen, in equal ratio.
material 1 6.  12.  .5
material 1 1.  1.  .5
```

`eos 35 1` $ The equation of state for parylene is called

`eos 1035 1`

`ioniz 1 4` $ LTE 'average atom' ionisation is selected

`group 1 40 0.01 10` $ The photon groups are defined

`source laser 0.438` $ The laser wavelength and Gaussian temporal profile is specified

`gauss 3.5e-10 2.3E+16 3.e-10`

`ray 0 0.123553 322.9028 0.019977832 1` $ By defining a series of rays a Gaussian spatial profile is constructed with each ray specified by an angle from the negative z axis and an $r - z$ coordinate along its path.

`ray 0 0.123324 322.8656 0.02017761 1`

`ray 0 0.123096 322.8284 0.020377388 1`

`ray 0 0.122869 322.7912 0.020577167 1`

`ray 0 0.122643 322.754 0.020776945 1`

`ray 0 0.122417 322.7168 0.020976723 1`

`ray 0 0.122192 322.6795 0.021176501 1`

`ray 0 0.121967 322.6423 0.02137628 1`

`ray 0 0.121743 322.6051 0.021576058 1`

`ray 0 0.12152 322.5679 0.021775836 1`

`ray 0 0.121297 322.5307 0.021975615 1`

`ray 0 0.121075 322.4935 0.022175393 1`

`ray 0 0.120854 322.4563 0.022375171 1`

```
ray 0 0.120633 322.419 0.02257495 1

ray 0 0.120413 322.3818 0.022774728 1

ray 0 0.120194 322.3446 0.022974506 1

ray 0 0.119975 322.3074 0.023174285 1

ray 0 0.119756 322.2702 0.023374063 1

ray 0 0.119539 322.233 0.023573841 1

ray 0 0.119322 322.1957 0.02377362 1

ray 0 0.119106 322.1585 0.023973398 1

ray 0 0.11889 322.1213 0.024173176 1

ray 0 0.118675 322.0841 0.024372955 1

ray 0 0.11846 322.0469 0.024572733 1

ray 0 0.118246 322.0097 0.024772511 1

ray 0 0.118033 321.9724 0.024972289 1

ray 0 0.117821 321.9352 0.025172068 1

ray 0 0.117608 321.898 0.025371846 1

ray 0 0.117397 321.8608 0.025571624 1

ray 0 0.117186 321.8236 0.025771403 1

ray 0 0.116976 321.7864 0.025971181 1

ray 0 0.116766 321.7491 0.026170959 1

ray 0 0.116557 321.7119 0.026370738 1

ray 0 0.116349 321.6747 0.026570516 1

ray 0 0.116141 321.6375 0.026770294 1

ray 0 0.115934 321.6003 0.026970073 1

ray 0 0.115728 321.5631 0.027169851 1
```

```
ray 0 0.115522 321.5259 0.027369629 1

ray 0 0.115316 321.4886 0.027569408 1

ray 0 0.115111 321.4514 0.027769186 1

ray 0 0.114907 321.4142 0.027968964 1

ray 0 0.114704 321.377 0.028168743 1

ray 0 0.114501 321.3398 0.028368521 1

ray 0 0.114298 321.3026 0.028568299 1

ray 0 0.114096 321.2653 0.028768077 1

ray 0 0.113895 321.2281 0.028967856 1

ray 0 0.113694 321.1909 0.029167634 1

ray 0 0.113494 321.1537 0.029367412 1

ray 0 0.113295 321.1165 0.029567191 1

ray 0 0.113096 321.0793 0.029766969 1

ray 0 0.112897 321.042 0.029966747 1
```

`pparray rho te dene deni zbar` $ The output is chosen to be mass density, electron temperature, electron number density, ion number density and average ionisation

```
parm lrstrt 1 $ The timing for simulation output is set

parm postdt 1.e-11

parm editdt 1.e-13

parm tstop 1.e-9

parm nstop 100000000
```

```
parm rpltdt 1.e-11

parm dtmin 1.e-25

parm dtmax 1.e-12

parm dt 1.e-13


parm lrdtrn 1 $ Radiation transport is initialised

parm irdkap 1

parm flxlem 0.03 $ The electron flux limiter of 0.03 is specified

parm temin 2.57e-5

parm xlram 1 $ The model of angle dependent resonance absorption at the crit-
```

ical density is chosen

```
parm xlrdsm 1

parm xlcutm 1.e-16
```

Appendix C

Publications

Papers published by L.M.R. Hobbs as L.M.R. Gartside.

1. L.M.R. Gartside, G.J. Tallents, A.K. Rossall, E. Wagenaars, M. Kalal, M. Kozlová, J. Nejdl, J. Polan, M. Sawicka and B. Rus. Extreme ultraviolet interferometry of laser plasma material between the critical and ablation surfaces. *HEDP*, 7, 91, 2011.

2. L.M.R. Gartside, G.J. Tallents, A.K. Rossall, M. Kalal, M. Kozlová, J. Nejdl, J. Polan, M. Sawicka and B. Rus. Extreme ultra-violet interferometry of warm dense matter in laser-plasmas. *Opt. Lett.*, 35, 3820, 2010.

3. L.M.R. Gartside, G.J. Tallents, J. Pasley, J. Gaffney and S.J. Rose. XUV probing as a diagnostic of Rayleigh-Taylor instability growth. *Springer Proc. Phys.*, 130, 469, 2008.

4. A.K. Rossall, L.M.R Gartside, S. Chaurasia, S. Tripathi, D.S. Munda, N.K. Gupta, L.J. Dhareshwar, J. Gaffney, S.J. Rose and G.J. Tallents. X-ray backlighter characterization for iron opacity measurements using laser-produced aluminium K-alpha emission. *J. Phys. B: At. Mol. Opt. Phys.*, 43, 155403, 2010.

5. E. Wagenaars, L.M.R. Gartside, A.K. Rossall, N. Booth, S. White, C.L.S. Lewis, M.M. Notley, R. Heathcote, G.J. Tallents. Laboratory measurements of hot iron opacities at EUV wavelengths. *Proc. of SPIE*, 74510G, 2009.

6. G.J. Tallents, N. Booth, M.H. Edwards, L.M.R. Gartside, H. Huang, A.K. Rossall, E. Wagenaars, D.S. Whittaker and Z. Zhai. X-ray lasers as probes of plasma parameters. *Springer Proc. Phys.*, 130, 331, 2008

7. G.J. Tallents, I. Al'miev, N. Booth, M.H. Edwards, L.M.R. Gartside, H.Huang, A.K. Rossall, D.S. Whittaker and Z. Zhai. Collisionally excited extreme ultra-violet lasers created by laser irradiation of plasmas. *IEEE LEOS ANN MTG 2009*, 108, 2009.

8. T. Mocek, B. Rus, M. Kozlová, J. Polan, P. Homer, K. Jakubczak, J. Nejdl, D. Snopek, M. Fajardo, J.R. Davies, A. Barszczak-Sardinha, G.J. Tallents, N. Booth, M.H. Edwards, L.M.R. Gartside, D.S. Whittaker, Z. Zhai, P. Mistry, G.J. Pert GJ, R.W. Lee, M.E. Foord, H. Chung and S.J. Moon. Applications of high energy X-ray lasers in plasma probing and warm dense matter generation. *IEEE LEOS ANN MTG 2009*, 313, 2009.

Abbreviations

AA	Average Atom
ASE	Amplified Spontaneous Emission
CCA	Close Coupling Approximation
CCD	Charged Coupled Device
CLF	Central Laser Facility
CPA	Chirped Pulse Amplification
DCA	Detailed Configuation Accounting
DT	Deuterium-Tritium
DTA	Detailed Term Accounting
EUV	Extreme UltraViolet
FEL	Free Electron Laser
FI	Fast Ignition
GRIP	GRazing Incidence Pumping
ICF	Inertial Confinement Fusion
IMP	Ionised Materials Package
LEDCOP	Light Element Detailed Configuration OPacity
LLNL	Lawrence Livermore National Laboratory

LTE	Local Thermodynamic Equilibrium
OP	Opacity Project
RAL	Rutherford Appleton Laboratory
RTI	Rayleigh-Taylor Instability
UTA	Unresolved Transitional Array

Symbols

α	Beam divergence (rad)	Ch. 3
β	Imaginary part of refractive index as - β	Ch. 2
β_a	Numerical coefficient (Rayleigh-Taylor Instability)	Ch. 2
γ	Instability growth rate (s^{-1})	Ch. 2
δ	Real part of refractive index as 1 - δ	Ch. 2
$\epsilon_{K\alpha}$	K_α emission (photons cm^3 s^{-1})	Ch. 5
η	Index of refraction	Ch. 1
η^*	Complex index of refraction	Ch. 2
θ	Incident angle of laser (rad)	Ch. 1
κ	Absorption coefficient (cm^{-1})	Ch. 1
λ	Wavelength (nm)	Ch. 1
ν	Frequency (s^{-1})	Ch. 1
$\Delta\nu$	Frequency bandwidth (s^{-1})	Ch. 1
ρ	Mass density (g cm^{-3})	Ch. 2
$\Delta\rho z$	Rms areal density	Ch. 5
σ	Absorption cross-section (cm^2)	Ch. 2
σ_s	Specific absorption cross-section (cm^2 g^{-1})	Ch. 2

τ	Rate of absorbtion/extincition	Ch. 2
ϕ	Mirror angle/grating angle (rad)	Ch. 3
χ	Spatial frequency axis in x direction	Ch. 3
χ_0	Spatial frequency in x direction (μm^{-1})	Ch. 3
ψ	Spatial frequency axis in y direction	Ch. 3
ψ_0	Spatial frequency in y direction (μm^{-1})	Ch. 3
ω	Angular frequency (rad s^{-1})	Ch. 1
Ω	Integrable variable in frequency (rad)	Ch. 2
Ω_m	Mirror spatial angle (rad)	Ch. 6
Ω_p	Pinhole spatial angle (rad)	Ch. 6
ε	Integrable variable in energy (eV^{-1})	Ch. 2
φ, $\Delta\varphi$	Phase shift, change in phase shift (rad)	Ch. 2
a	Source to mirror distance (mm)	Ch. 6
$a(x, y, t)$	Probe instantaneous amplitude	Ch. 3
a_0	Reference instantaneous amplitude	Ch. 3
$\bar{a}_0$	Average amplitude	Ch. 3
A_R	Shell aspect ratio	Ch. 2
$b(x, y)$	Background	Ch. 3
$b(x, y, t)$	Instantaneous background	Ch. 3
$\bar{b}_0$	Average background	Ch. 3
b_{mirror}	Mirror-image distance (mm)	Ch. 6
b_{pinhole}	Pinhole-image distance (mm)	Ch. 6
B	Background (middle) intensity	Ch. 3

B_ω	Planck black body distribution	Ch. 2
c	Speed of light (3×10^{10} cm s^{-1})	Ch. 2
dE	Change in internal energy	Ch. 2
dq	Heat transfer	Ch. 2
ds	Change in entropy	Ch. 2
d_m	Mirror diameter (mm)	Ch. 6
d_p	Pinhole diameter (mm)	Ch. 6
E	Energy (eV)	Ch. 2
$E_{K\alpha}$	K_α photon energy (keV)	Ch. 5
E_{Z^*}	Ionisation energy (eV)	Ch. 1
f	Mirror focal length (mm)	Ch. 6
$f(t)$	Probe temporal profile	Ch. 3
f_0	Fringe spatial frequency (μm^{-1})	Ch. 3
f_1	Real atomic scattering factor	Ch. 2
f_2	Imaginary atomic scattering factor	Ch. 2
g	Fluid acceleration (cm s^{-2})	Ch. 2
g_v	Electron velocity distribution function	Ch. 5
h	Planck's constant (4.1×10^{-15} eVs)	Ch. 1
$i(x, y, t)$	Intensity	Ch. 3
I	Laser intensity (W cm^{-2})	Ch. 1
I_0	Initial intensity (W cm^{-2})	Ch. 2
I_a	Absorbed intensity (W cm^{-2})	Ch. 6
I_m	Intensity after mirror (W cm^{-2})	Ch. 6

I_p	Intensity after pinhole (W cm^{-2})	Ch. 6
I_t	Intensity of target emission (W cm^{-2})	Ch. 6
k	Wavenumber (μm^{-1})	Ch. 2
$\mathbf{k}^*$	Propagating wavevector (μm^{-1})	Ch. 2
K	Electron collisional excitation rate (s^{-1})	Ch. 5
Δl	Smallest resolvable distance (μm)	Ch. 6
L	Length of medium or path length (cm)	Ch. 1
L_0	Target thickness (cm)	Ch. 2
m	Mass (g)	Ch. 2
$\dot{m}$	Mass ablation rate (g s^{-1} cm^{-2})	Ch. 2
m_e	Electron mass (g)	Ch. 4
M	Magnification	Ch. 6
n	Principle quantum number	Ch. 1
n_{fringe}	Number of fringe shifts	Ch. 1
N_{atoms}	Atomic density (cm^{-3})	Ch. 2
N_{crit}	Critical density (cm^{-3})	Ch. 1
N_e	Electron density (cm^{-3})	Ch. 1
N_i	Ion density (cm^{-3})	Ch. 4
Q_{max}	Heat flow	Ch. 4
p_a	Ablation pressure (Mbar)	Ch. 2
P	Pressure (Mbar)	Ch. 2
r	Zone or cell width, directional axis (cm)	Ch. 4
r_{min}	Minimum separation (cm)	Ch. 2

r_{e-i}	Electron-ion separation (cm)	Ch. 2
r_0	Classic electron radius (cm)	Ch. 2
R	Shell radius (mm)	Ch. 2
ΔR	Shell thickness (mm)	Ch. 2
R_0	Shell radius (mm)	Ch. 2
ΔR_0	Shell thickness (mm)	Ch. 2
t	Time (s)	Ch. 6
T	Transmission	Ch. 2
T_e	(Electron) temperature (eV)	Ch. 1
V	Specific volume ($cm^3\ g^{-1}$)	Ch. 2
$\bar{v}_0$	Average visibility	Ch. 3
$v(x, y)$	Visibility	Ch. 3
$v(x, y, t)$	Instantaneous visibility	Ch. 3
$v^*(x, y, t)$	Complex conjugate to instantaneous visibility	Ch. 3
v_a	Ablation velocity ($cm\ s^{-1}$)	Ch. 2
v_p	Phase velocity ($cm\ s^{-1}$)	Ch. 2
V	Visibility (lobe) intensity	Ch. 3
V^*	Complex conjugate to visibility intensity	Ch. 3
x	Directional axis	Ch. 3
y	Directional axis	Ch. 3
Δy	Fringe Separation (cm)	Ch. 3
z	Zone or cell thickness (cm), directional axis	Ch. 2
Z	Atomic number	Ch. 1

Z^*	Ionisation level	Ch. 1
$\bar{Z}^*$	Average number of free electrons per ion	Ch. 6

References

[1] G.J. Tallents. The physics of soft x-ray lasers pumped by electron collisions in laser plasmas. *J. Phys. D: Appl. Phys.*, 36:R259, 2003.

[2] C.L.S. Lewis and J. McGlinchey. Quasi-monochromatic projection radiography of dense laser driven spherical targets. *Opt. Commun.*, 53:179, 1985.

[3] O. Willi, T. Afshar-Rad, M. Desselberger, M. Dunne, J. Edwards, F. Khattak, and R. Taylor. Time resolved soft x-ray imaging with submicron spatial resolution. *Rev. Sci. Instrum.*, 63:4818, 1992.

[4] L.B. Da Silva, T.W. Barbee, Jr., R. Cauble, P. Celliers, D. Ciarlo, S. Libby, R.A. London, D. Matthews, S. Mrowka, J.C. Moreno, D. ress, J.E. Trebes, A.S. Wan, and F. Weber. Electron density measurements of a high density plasma using soft x-ray laser interferometry. *Phys. Rev. Lett*, 74:3991, 1995.

[5] M.H. Key, T.W. Barbee, Jr., L.B. Da Silva, S.G. Glendinning, D.H. Kalantar, S.J. Rose, and S.V. Weber. New plasma diagnostic possibilities from radiography with XUV lasers. *JQSRT*, 54:221, 1995.

[6] G.J. Pert. XUV lasers and applications of laser produced plasmas. *CLF Annual Report*, page 134, 1984.

[7] T.S. Perry, S.J. Davidson, F.J.D. Serduke, D.R. Bach, C.C. Smith, J.M. Foster, R.J. Doyas, R.A. Ward, C.A. Iglesias, F.J. Rogers, J. Abdallah Jr., R.E. Stewart, J.D. Kilkenny, and R.W. Lee. Opacity measurements in hot dense medium. *Phys. Rev. Lett.*, 67:27, 1991.

[8] L.B. Da Silva, B.J. MacGowan, D.R. Kania, B.A. Hammel, C.A. Back, E. Hsieh, R. Doyas, C.A. Igelsias, F.J. Rogers, and R.W. Lee. Absorption measurements demonstrating the importance of δn=0 transitions in the opacity of iron. *Phys. Rev. Lett.*, 69:438, 1992.

[9] P.T. Springer, D.J. Fields, B.G. Wilson, J.K. Nash, W.H. Goldstein, C.A. Iglesias, F.J. Rogers, J.K. Swenson, M.H. Chen, A. Bar-Shalom, and R.E. Stewart. Spectroscopic absorption measurements of an iron plasma. *Phys. Rev. Lett.*, 69, 1992.

[10] P.T. Springer, D.F. Fields, B.G. Wilson, J.K. Nash, W.H. Goldstein, C.A. Iglesias, F.J. Rogers, J.K. Swenson, M.H. Chen, A. Bar-Shalom, and R.E. Stewart. Spectroscopic measurements of Rosseland Mean opacity. *JQSRT*, 51:371, 1994.

[11] I.B. Földes, R. Sigel, C-H. Shi-Sheng, K. Eidmann, R.F. Schmalz, G.D. Tsakiris, and S. Witkowski. Simultaneous x-ray and optical shadowgraph of cavities heated by $\lambda = 0.44$ μm laser light. *Laser Part. Beams*, 6:123, 1988.

[12] H.G. Ahlstrom. Laser fusion experiments, facilities and diagnostics at Lawrence Livermore Laboratory. *Appl. Optics*, 20:1902, 1981.

[13] W.W. Hsing, C.W. Barnes, J.B. Beck, N.M. Hoffman, D. Galmiche, A. Richard, J. Edwards, P. Graham, S. Rothman, and B. Thomas. Rayleigh-Taylor Instability evolution in ablatively driven cylindrical implosions. *Phys. Plasmas*, 4:1832, 1997.

[14] J.E. Bailey, G.A. Chandler, R.C. Mancini, S.A. Slutz, G.A. Rochau, M. Bump, T.J. Buris-Mog, G. Cooper, G. Dunham, I. Golovkin, J.D. Kilkenny, P.W. Lake, R.J. Leeper, R. Lemke, J.J. MacFarlane, T.A. Mehlhorn, T.C. Moore, T.J. Nash, A. Nikroo, D.S. Nielsen, K.L. Peterson, C.L. Ruiz, D.G. Schroen, D. Steinman, and W. Varnum. Dynamic hohlraum radiation hydrodynamics. *Phys. Plasmas*, 13:056301, 2006.

[15] J.E. Bailey, G.A. Rochau, C.A. Iglesias, J. Abdallah Jr., J.J. MacFarlane, I. Golovkin, P. Wang, R.C. Mancini, P.W. Lake, T.C. Moore, M. Bump, O. Garcia, and S. Mazevet. Iron-plasma transmission measurements at temperatures above 150 ev. *Phys. Rev. Lett.*, 99:265002, 2007.

[16] M.D. Rosen. The science applications of the high-energy density plasmas created on the Nova laser. *Phys. Plasmas*, 3:1803, 1996.

[17] M.K. Matzen. Z pinches as intense x-ray sources for high energy density physics applications. *Phys. Plasmas*, 4:1519, 1997.

[18] S.V. Lebedev, D.J. Ampleford, S.N. Bland, S.C. Bott, J.P. Chittenden, J. Goyer, C. Jennings, M.G. Haines, G.N. Hall, D.A. Hammer, J.B.A. Palmer, S.A. Pikuz, T.A. Shelkovenko, and T. Christoudiass. Physics of

wire array Z-pinch implosions: experiments at Imperial College. *Plas. Phys. Control. Fusion*, 47:A91, 2005.

[19] J.M. Foster, D.J. Hoarty, C.C. Smith, P.A. Rosen, S.J. Davidson, S.J. Rose, T.S. Perry, and F.J.D. Serduke. L-shell absorption spectrum of an open M-shell germanium plasma: comparison of experimental data with a detailed configuration accounting calculation. *Phys. Rev. Lett.*, 67:3255, 1991.

[20] G. Winhart, K. Eidmann, C.A. Iglesias, A. Bar-Shalom, E. Minguez, A. Rickert, and S.J. Rose. XUV opacity measurements and comparison with models. *JQSRT*, 54:437, 1995.

[21] G. Winhart, K. Eidmann, C.A. Iglesias, and A. Bar-Shalom. Measurements of extreme UV opacities in hot dense Al, Fe and Ho. *Phys. Rev. Lett.*, 74: 3816, 1995.

[22] Jon Larsen, creator. Code h2d supplied by Cascade Applied Sciences, Larsen@casinc.com.

[23] P.B. Corkum. Plasma perspective on strong field multiphoton ionization. *Phys. Rev. Lett.*, 71:1994, 1993.

[24] B. Dromey, S. Kar, C. Bellei, D.C. Carroll, R.J. Clarke, J.S. Green, S. Kneip, K. Markey, S.R. Nagel, P.T. Simpson, L. Willingale, P. McKenna, D. Neely, Z. Najmudin, K. Krushelnick, P.A. Norreys, and M. Zepf. Bright multi-kev harmonic generation from relativistically oscillating plasma surfaces. *Phys. Rev. Lett.*, 99:085001, 2007.

[25] B. Dromey, M. Zepf, A. Gopal, K. Lancaster, M.S. Wei, K. Krushelnick, M. Tatarakis, N. Vakakis, S. Moustaizis, R. Kodama, M. Tampo, C. Stoeckl, R. Clarke, H. Habara, D. Neely, S. Karsch, and P. Norreys. High harmonic generation in the relativistic limit. *Nat. Phys. Lett.*, 2:456, 2006.

[26] M. Zepf, B. Dromey, M. Landreman, P. Foster, and S.M. Hooker. Bright quasi-phase-matched soft-x-ray harmonic radiation from argon ions. *Phys. Rev. Lett.*, 99:143901, 2007.

[27] H.-T Kim, V. Tosa, and C.-H Nam. Synchronized generation of bright high-order harmonics using self-guided and chirped femtosecond laser pulses. *J. Phys. B: At. Mol. Opt. Phys.*, 39:S265, 2006.

[28] B. Dromey, S.G. Rykovanov, D. Adams, R. H́orlein, Y. Nomura, D.C. Carroll, P.S. Foster, S. Kar, K. Markey, P. McKenna, D. Neely, M. Geissler, G.D. Tsakiris, and M. Zepf. Tunable enhancement of high harmonic emission from laser solid interactions. *Phys. Rev. Lett*, 102:225002, 2009.

[29] G.J. Tallents. *Optical Society of America. Handbook of Optics. Volume 5. Section 58.* McGraw-Hill, 2009.

[30] E. Wagenaars, D.S. Whittaker, and G.J. Tallents. A method to probe Rosseland and Planck mean opacities with high-order harmonics. *HEDP*, 7:17, 2011.

[31] R.C. Elton. *X-ray lasers.* Academic Press, 1990.

[32] P. Jaeglé. *Coherent sources of XUV radiation.* Springer, 2006.

[33] D.L. Matthews, P.L. Hagelstein, M.D. Rosen, M.J. Eckart, N.M. Ceglio, A.U. Hazi, H. Medecki, B.J. MacGowan, J.E. Trebes, B.L. Whitten, E.M. Campbell, C.W. Hatcher, A.M. Hawryluk, R.L. Kauffmann, L.D. Pleasance, G. Rambach, J.H. Scofield, G. Stone, and T.A. Weaver. Demonstration of a soft x-ray amplifier. *Phys. Rev. Lett.*, 54:110, 1985.

[34] C.L.S Lewis and O. Willi. XUV lasers and applications of laser produced plasmas. *CLF Annual Report*, page 84, 1985.

[35] T.N. Lee, E.A. McLean, and R.C. Elton. Soft x-ray lasing in neonlike germanium and copper plasmas. *Phys. Rev. Lett.*, 59:1185, 1987.

[36] A. Carillon, H.Z. Chen, P. Dhez, L. Dwivedi, J. Jacoby, P. Jaegle, G. Jamelot, J. Zhang, M.H. Key, A. Kidd, A. Klisnick, R. Kodama, J. Krishnan, C.L.S. Lewis, D. Neely, P. Norreys, D. O'Neill, G.J. Pert, S.A. Ramsden, J.P. Raucourt, G.J. Tallents, and J. Uhomoibhi. Saturated and near diffraction limited operation of an XUV laser at 23.6 nm. *Phys. Rev. Lett.*, 68:2917, 1992.

[37] H. Daido, Y. Kato, K. Murai, S. Ninomiya, R. Kodama, G. Yuan, Y. Oshikane, M. Takagi, and H. Takabe. Efficient soft x-ray lasing at 6 to 8 nm with nickel-like lanthanide ions. *Phys. Rev. Lett.*, 75:1074, 1995.

[38] J. Nilsen, B.J. MacGowan, L.B. Da Silva, and J.C. Moreno. Prepulse technique for producing low Z ne-like x-ray lasers. *Phys. Rev. A*, 48:4682, 1993.

[39] G.J. Pert. Optimizing the performance of nickel-like collisionally pumped x-ray lasers. II. Lasers for the wavelength range 50-100 angstrom. *Phys. Rev. A*, 75:023808, 2007.

[40] S. Kazamias, K. Cassou, D. Ros, F. Plé, G. Jamelot, A. Klisnick, O. Lundh, F. Lindau, A. Persson, C.G. Wahlström, S. de Rossi, D. Joyeux, B. Zielbauer, D. Ursescu, and T. Kühl. Characterization of a transient collisional Ni-like molybdenum soft-x-ray laser pumped in grazing incidence. *Phys. Rev. A*, 77:033812, 2008.

[41] R. Keenan, J. Dunn, P.K. Patel, D.F. Price, R.F. Smith, , and V.N. Shlyaptsev. High repetition rate grazing incidence pumped x-ray laser operating at 18.9 nm. *Phys. Rev. Lett.*, 94:103901, 2005.

[42] N. Booth. *Development of x-ray lasers and their application to plasma probing.* PhD thesis, University of York, 2008.

[43] D. Strickland and G. Mourou. Compression of amplified chirped optical pulses. *Opt. Commun.*, 56:219, 1985.

[44] B. Rus, T. Mocek, A.R. Präg, M Kozlová, G. Jamelot, A. Carillon, D. Ros, D. Joyeux, and D. Phalippou. Multimillijoule, highly coherent x-ray laser at 21 nm operating in deep saturation through double-pass amplification. *Phys. Rev. A*, 66:063806, 2002.

[45] R. Cauble, L.B. Da Silva, T.W. Barbee, Jr., P. Celliers, J.C. Moreno, and A.S. Wan. Micron resolution radiography of laser accelerated and x-ray heated foils with an x-ray laser. *Phys. Rev. Lett.*, 74:3816, 1996.

[46] D.H. Kalantar, T.W. Barbee, Jr., L.B. Da Silva, S.G. Glendinning, F. Weber, S.V. Weber, M.H. Key, and J.P. Knauer. X-ray laser radiography of perturbations due to imprint of laser speckle in 0.35 μm laser irradiation of a thin Si foil. *Rev. Sci. Instrum.*, 67:781, 1996.

[47] D.H. Kalantar, M.H. Key, L.B. Da Silva, S.G. Glendinning, B.A. Remington, J.E. Rothenberg, F. Weber S.V. Weber, N.S. Kim, D. Neely, E. Wolfrum, J. Zhang, J.S Wark, A. Demir, J. Lin, R. Smith, G.J. Tallents, C.L.S. Lewis, A. MacPhee, J. Warwick, and J.P. Knauer. Measurements of direct drive laser imprint in thin foils by radiography using an x-ray laser backlighter. *Phys. Plasmas*, 4:1985, 1997.

[48] E. Wolfrum, J. Wark, J. Zhang, D. Kalantar, M.H. Key, B.A. Remington, S.V. Weber, D. Neely, S. Rose, J. Warwick, A. MacPhee, C.L.S. Lewis, A. Demir, J. Lin, R. Smith, and G.J. Tallents. Measurement of single mode imprint in laser ablative drive of a thin Al foil by extreme ultraviolet laser radiography. *Phys. Plasmas*, 5:227, 1998.

[49] G.J. Pert. Algorithms for the self-consistent generation of magnetic fields in plasmas. *J. Comp. Phys.*, 43:111, 1981.

[50] M.H. Edwards, D.S. Whittaker, G.J. Tallents, P. Mistry, G.J. Pert, B. Rus, T. Mocek, M. Kozlová, A. Präg J. Polan, M. Stupka, and P. Homer. Laser-ablation rates measured using x-ray laser transmission. *Phys. Rev. Lett.*, 99: 195002, 2007.

[51] S.P. Regan, R. Epstein, V.N. Goncharov, I.V. Igumenshchev, D. Li, P.B. Radha, H. Sawada, W. Seka, T.R. Boehly, J.A. Delettrez, O.V. Gotchev, J.P. Knauer, J.A. Marozas, F.J. Marshall, R.L. McCrory, P.W. McKenty, D.D. Meyerhofer, T.C. Sangster, D. Shvarts, S. Skupsky, V.A. Smalyuk, B. Yaakobi, and R.C. Mancini. Laser absorption, mass ablation rate and shock heating in direct-drive inertial confinement fusion. *Phys. Plasmas*, 14: 056305, 2007.

[52] R.A. Burdt, S. Yuspeh, K.L. Sequoia, Y. Tao, M.S. Tillack, and F. Najmabadi. Experimental scaling law for mass ablation rate from a Sn plasma generated by a 1064 nm laser. *J. Appl. Phys.*, 106:033310, 2009.

[53] M.H. Edwards, D. Whittaker, P. Mistry, N. Booth, G.J. Pert, G.J. Tallents, B. Rus, T. Mocek, M. Koslová, C. McKenna, A. Delserieys, C.L.S. Lewis, M. Notley, and D. Neely. Opacity measurements of a hot iron plasma using an x-ray laser. *Phys. Rev. Lett.*, 97:035001, 2006.

[54] M.H Key, W.T. Toner, T.J. Goldsack, J.D. Kilkenny, S.A. Veats, P.F. Cunningham, and C.L.S Lewis. A study of ablation by laser irradiation of plane targets at wavelengths 1.05, 0.53 and 0.35 μm. *Phys. Fluids*, 26:2011, 1983.

[55] T.L. Goldsack, J.D. Kilkenny, and P.T. Rumsby. Determination of mass ablation rates and ablation pressures on spherical targets by ion emission. *J. Phys. D: Appl. Phys.*, 14:L47, 1981.

[56] B.L. Henke, E.M. Gullikson, and J.C. Davis. X-ray interactions: photoabsorption, scattering, transmission and reflection at E=50-30000ev, Z=1-92. *Atom. Data Nucl. Data*, 51:181, 1993.

[57] A.S. Wan, L.B. Da Silva, T.W. Barbee, Jr., R. Cauble, P. Celliers, S.B. Libby, R.A. London, J.C. Moreno, J.E. Trebes, and F. Weber. Application of x-ray laser interferometry to study high density laser produced plasmas. *J. Opt. Soc. Am. B*, 13:447, 1996.

[58] Ya.B. Zel'dovich and Yu.P. Raizer. *Physics of shock waves and high temperature hydrodynamic phenomena*. Dover Publications, 2002.

[59] R.F. Smith, J. Dunn, J. Nilson, V.N. Schlyaptsev, S. Moon, J. Filevich, J.J. Rocca, M.C. Marconi, J.R. Hunter, and T.W. Barbee. Picosecond x-ray laser interferometry of dense plasmas. *Phys. Rev. Lett.*, 89:065004, 2002.

[60] P. Emma, R. Akre, J. Arthur, R. Bionta, C. Bostedt, J. Bozek, A. Brachmann, P. Bucksbaum, R. Coffee, F.-J. Decker, Y. Ding, D. Dowell, S. Edstrom, A. Fisher, J. Frisch, S. Gilevich, J. Hastings, G. Hays, Ph. Hering, Z. Huang, R. Iverson, H. Loos, M. Messerschmidt, A. Miahnahri, S. Moeller, H.-D. Nuhn, G. Pile, D. Ratner, J. Rzepiela, D. Schultz, T. Smith, P. Stefan, H. Tompkins, J. Turner, J.Welch, W. White, J. Wu, G. Yocky, and J. Galayda. First lasing and operation of an angstrom-wavelength free-electron laser. *Nat. Photonics*, 4:641, 2010.

[61] B.W.J. McNeil and N.R. Thompson. X-ray free electron lasers. *Nat. Photonics*, 12:814, 2010.

[62] P. Schmäuser, M. Dohlus, and J. Rossbach. *Ultraviolet and soft x-ray free-electron lasers*. Springer Berlin / Heidelberg, 2009.

[63] K. Sokolowski-Tinten, J. Bialkowski, A. Cavalleri, D. von der Linde, A. Oparin, J. Meyer-ter-Vehn, and S.I. Anisimov. Transient states of matter during short pulse laser ablation. *Phys. Rev. Lett.*, 81:224, 1998.

[64] F. Dahmani. Experimental scaling laws for mass ablation rate, ablation pressure in planar laser-produced plasmas with laser intensity, laser wavelength and target atomic number. *J. Appl. Phys.*, 74:622, 1993.

[65] B.N. Chichkov, C. Momma, S. Nolte, and F. von Alvensleben A. Tünnermann. Femtosecond, picosecond and nanosecond laser ablation of solids. *Appl. Phys. A*, 63:109, 1996.

[66] M.S. Qaisar and G.J. Pert. Laser ablation of Mg, Cu, and Pb using infrared and ultraviolet low-fluence lasers. *J. Appl. Phys.*, 94:1468, 2003.

[67] S. Atzeni. Laser-plasma interaction and high-pressure generation for inertial fusion and basic science. *Plasma Phys. Control. Fus.*, 42:B143, 2000.

[68] A.L. Schawlow and C.H. Townes. *Phys. Rev.*, 112:1940, 1958.

[69] T.H. Maiman. Stimulated optical radiation in ruby. *Nature*, 187:493, 1960.

[70] R.E. Honig and J.R. Woolston. Laser induced emission of electrons, ions and neutral atoms from solid surfaces. *Appl. Phys. Lett.*, 2:138, 1963.

[71] S.A. Ramsden and W.E.R. Davies. Radiation scattered from the plasma produced by a focused ruby laser beam. *Phys. Rev. Lett.*, 13:227, 1964.

[72] S.E. Bodner, D.G. Colombant, J.H. Gardner, R.H. Lehmberg, S.P. Obenschain, L. Phillips A.J. Schmitt J.D. Sethian, R.L. McCrory, W. Seka, C.P. Verdon, J.P. Knauer, B.B. Afeyan, and H.T. Powell. Direct-drive laser fusion: Status and prospects. *Phys. Plasmas*, 5:1901, 1998.

[73] A.J. Schmitt, D.G. Colombant, A.L. Velikovich, S.T. Zalesak, J.H. Gardner, D.E. Fyfe, and N. Metzler. Large-scale high-resolution simulations of high gain direct-drive inertial confinement fusion targets. *Phys. Plasmas*, 11:2719, 2004.

[74] S. Atzeni and J. Meyer-ter-Vehn. *The physics of inertial fusion.* Oxford Science, 1998.

[75] S. Atzeni. Laser driven inertial fusion: the physical basis of current and recently proposed ignition experiments. *Plasma Phys. Control. Fusion*, 51: 124029, 2009.

[76] J. Lindl. Development of the indirect drive approach to inertial confinement fusion and the target physics basis for ignition and gain. *Phys. Plasmas*, 2: 3933, 1995.

[77] S. Atzeni, J.R. Davies, L. Hallo, J.J. Honrubia, P.H. Maire, M. Olazabal-Loumé, J.L. Feugeas, X. Ribeyre, A. Schiavi1, G. Schurtz, J. Breil, and Ph. Nicolaï. Studies on targets for inertial fusion ignition demonstration at the HiPER facility. *Nucl. Fusion*, 49:055008, 2009.

[78] M. Tabak, J. Hammer, M.E. Glinsky, W.L. Kruer, S.C. Wilks, J. Woodworth, E.M. Campbell, M.D. Perry, and R.J. Mason. Ignition and high gain ultrapowerful lasers. *Phys. Plasmas*, 1:1626, 1994.

[79] J. Nuckolls, L. Wood, A. Thiessen, and G. Zimmerman. Laser compression of matter to super high densities: thermonuclear (CTR) applications. *Nature*, 239:139, 1972.

[80] H.J. Kull. Theory of the Rayleigh-Taylor Instability. *Phys. Rep.*, 206:197, 1991.

[81] H. Takabe, K. Mima, L. Montierth, and R.L. Morse. Self-consistent growth rate of the Rayleigh-Taylor Instability in an ablatively accelerating plasma. *Phys. Fluids*, 28:3676, 1985.

[82] S. Atzeni, A. Schiavi, J.J. Honrubia, X. Ribeyre, G. Schurtz, Ph. Nicolaï, M. Olazabal-Loumé, C. Bellei, R.G. Evans, and J.R. Davies. Fast ignitor target studies for the HiPER project. *Phys. Plasmas*, 15:056311, 2008.

[83] R.J. Taylor, J.P. Dahlburg, A. Iwase, J.H. Gardner, D.E. Fyfe, and O. Willi. Measurement and simulation of laser imprinting and consequent Rayleigh-Taylor growth. *Phys. Rev. Lett*, 76:1643, 1996.

[84] D.H. Kalantar, L.B. Da Silva, S.G. Glendinning, B.A. Remington, F. Weber, M.H. Key, N.S. Kim, D. Neely, E. Wolfrum, J. Zhang, J.S Wark, A. Demir, J. Lin, R. Smith, G.J. Tallents, C.L.S. Lewis, A. MacPhee, J. Warwick, and J.P. Knauer. Extreme ultraviolet probing of laser imprint in a thin foil using an x-ray laser backlighter. *Rev. Sci. Instrum.*, 68:802, 1997.

[85] P.A. Norreys, R. Allott, R.J. Clarke, J. Collier, D. Neely, S.J. Rose, M. Zepf, M. Santala, A.R. Bell, K. Krushelnick, A.E. Dangor, N.C. Woolsey, R.G. Evans, H. Habara, T. Norimatsu, and R. Kodama. Experimental studies of the advanced fast ignitor scheme. *Phys. Plasmas*, 7:3721, 2000.

[86] S.D. Baton, M. Koenig, J. Fuchs, A. Benuzzi-Mounaix, P. Guillou, B. Loupias, T. Vinci, L. Gremillet, C. Rousseaux, M. Drouin, E. Lefebvre, F. Dorchies, C. Fourment, J.J. Santos, D. Batani, A. Morace, R. Redaelli, M. Nakatsutsumi, R. Kodama, A. Nishida, N. Ozaki, T. Norimatsu, Y. Aglitskiy, S. Atzeni, and A. Schiavi. Inhibition of fast electron energy deposition due to preplasma filling of cone-attached targets. *Phys. Plasmas*, 15:042706, 2008.

[87] H. Hora. Plasma mirror for high contrast picosecond laser pulses for fast ignition fusion. *J. Phys.: Conf. Ser.*, 112:022028, 2008.

[88] D.M. Gold. Direct measurement of prepulse suppresion by use of a plasma shutter. *Opt. Lett.*, 19:2006, 1994.

[89] J. Pasley and R. Stephens. Simulations investigating the effect of a deuterium-tritium-ice coating on the motion of the gold cone surface in a re entrant cone-guided fast ignition inertial confinement fusion capsule. *Phys. Plasmas*, 14:054501, 2007.

[90] J.N. Bahcall, S. Basu, M. Pinsonneault, and A.M. Serenelli. Helioseismological implications of recent solar abundance determinations. *Astrophys. J.*, 618:1049, 2005.

[91] N. Grevesse and A.J. Sauval. Standard solar composition. *Space Sci. Rev.*, 85:161, 1998.

[92] J.E. Bailey, G.A. Rochau, R.C. Mancini, C.A. Iglesias, J.J. MacFarlane, I.E. Golovkin, C. Blancard, Ph. Cosse, and G. Faussurier. Experimental investigation of opacity models for stellar interior, inertial fusion, and high energy density plasmas. *Pjys. Plasmas*, 16:058101, 2009.

[93] G.B. Rybicki and A.P. Lightman. *Radiative processes in astrophysics*. Wiley, 1979.

[94] D. Salzmann. *Atomic physics in hot plasmas*. Oxford University Press, 1998.

[95] D.S. Whittaker. *Radiative opacity of dense iron plasma*. PhD thesis, University of York, 2007.

[96] F.J.D. Serduke, E. Minguez, S.J. Davidson, and C.A. Iglesias. WorkOp-IV summary: lessons from iron opacities. *JQSRT*, 65:527, 2000.

[97] J.F. Chen and J.H. You. Diffusion approximation in the theory of radiative transfer. *Astrophys. Space Sci.*, 199:19, 1993.

[98] Prof. S.J. Rose. *Pulsed laser deposition of thin films*. private communication, 2011.

[99] N.H. Magee, J. Abdallah, Jr., R.E.H. Clark, J.S. Cohen, L.A. Collins, G. Csanak, C.J. Fontes, A. Gauger, J.J. Keady, D.P. Kilcrease, and A.L. Merts. Atomic structure calculations and new los alamos astrophysical opacities. *Astr. Soc. P.*, 78:51, 1995.

[100] F.R. Rogers and C.A. Iglesias. The OPAL opacity code: new results. *Astr. Soc. P.*, 78:31, 1994.

[101] The Opacity Project Team. *The Opacity Project Vol. 1.* Institute of Physics Publications, 1995.

[102] K.A. Berrington. Summary of the Opacity and IRON Projects. *Astro. Soc. P.*, 78:19, 1995.

[103] J.A. Gaffney and S.J. Rose. Opacity calculations on plasmas with open M and N shell configurations. *HEDP*, 5:216, 2009.

[104] A. Rickert. Review of the third international opacity workshop and code comparison study. *JQSRT*, 54:325, 1995.

[105] B.J.B. Crowley and J.W. Harris. Modelling of plasmas in an average-atom local density approximation: the CASSANDRA code. *JQSRT*, 71:257, 2001.

[106] S.J. Rose. Calculations of the radiative opacity of laser produced plasmas. *J. Phys. B: At. Mol. Opt. Phys.*, 25:1667, 1992.

[107] J.S. Cohen and N.H. Magee. Los alamos opacities on the world wide web. Los Alamos Report LA-UR-01-1257, Los Alamos National Laboratory, 2001.

[108] C.A. Iglesias and F.J. Rogers. Updated OPAL opacities. *Atrophys. J.*, 464: 943, 1996.

[109] F. Jin adn J. Zeng, T. Huang, Y. Ding, Z. Zheng, and J. Yuan. Radiative opacity of iron studied using a detailed level accounting model. *Astrophys. J.*, 693:597, 2009.

[110] G.J. Tallents, N. Booth, M.H. Edwards, L.M.R. Gartside, H. Huang, A.K. Rossall, E. Wagenaars, D.S. Whittaker, and Z. Zhai. X-ray lasers as probes of plasma parameters. *Springer Proc. Phys.*, 130:331, 2008.

[111] K. Widmann, T. Ao, M.E. Foord, D.F. Price, A.D. Ellis, P.T. Springer, and A. Ng. Single-state measurement of electrical conductivity of warm dense gold. *Phys. Rev. Lett.*, 92:125002, 2004.

[112] B. Barbrel, M. Koenig, A. Benuzzi-Mounaix, E. Brambrink, C.R.D. Brown, D.O. Gericke, B. Nagler, M. Rabec le Gloahec, D. Riley, C. Spindloe, S.M. Vinko, J. Vorberger, J. Wark, K. Wünsch, and G. Gregori. Measurement of short-range correlations in shock-compressed plastic by short-pulse x-ray scattering. *Phys. Rev. Lett.*, 102:165004, 2009.

[113] J.S. Toll. Causality and dispersion relation: logical foundations. *Phys. Rev.*, 104:1760, 1956.

[114] R. de L. Kronig. On the theory of the dispersion of x-rays. *J. Opt. Soc. Am.*, 12:547, 1926.

[115] T.P. Hughes. *Plasmas and laser light.* Adam Hilger, 1975.

[116] J. Nilsen, J.I. Castor, C.A. Iglesias, K.T. Cheng, J. Dunn, W.R. Johnson, J. Filevich, M.A. Purvis, J. Grava, and J.J. Rocca. Understanding the anomalous dispersion of doubly ionized carbon plasmas near 47 nm. *HEDP*, 4:107, 2008.

[117] E. Wagenaars, L.M.R. Gartside, A.K. Rossall, N. Booth, S. White, C.L.S. Lewis, M.M. Notley, R. Heathcote, and G.J. Tallents. Laboratory measurements of hot iron opacities at EUV wavelengths. *Proc. of SPIE*, 7451: 74510G, 2009.

[118] J. Kim and D.E. Kim. Characterisation of an imaging extreme ultraviolet flat field spectrometer and its application to extreme ultraviolet emission profile measurement. *Jpn. J. Appl. Phys.*, 39:6062, 2000.

[119] F. Strati. *Experimental and theoretical characterisation of short pulse x-ray lasers*. PhD thesis, University of York, 2001.

[120] M Kozlová, B. Rus, T. Mocek, J. Polan, M. Stupka, A. Präg, P. Homer, M. Hudeček, G. Jamelot, J.C. Lagron, K. Cassou, D. Ros, S. Kazamias, A. Klisnick, J.-J. Park, and C.-H. Nam. Double Lloyd's mirror - versatile instrument for XUV surface interferometry and interferometric microscopy. *Proc. of SPIE*, 5919:59190Q, 2005.

[121] E. Hecht. *Optics*. Addison Wesley, 1998.

[122] M. Osugi, K. Tanaka, N. Sakaya, K. Hamamoto, T. Watanabe, and H. Kinoshita. Resolution enhancement of extreme ultraviolet microscope using an extreme ultraviolet beam splitter. *Jpn. J. Appl. Phys.*, 47:4872, 2008.

[123] M. Kalal, B. Luther-Davies, and K.A. Nugent. Phase amplitude imaging: its application to fully automated analysis of magnetic filed measurements in laser produced plasmas. *Appl. Opt.*, 26:1674, 1987.

[124] M. Kalal and K.A. Nugent. Abel inversion using fast Fourier transforms. *Appl. Opt.*, 27:1956, 1988.

[125] K.A. Nugent. Interferogram analysis using an accurate fully automatic algorithm. *Appl. Opt.*, 24:3101, 1985.

[126] M. Kalal, O. Slezak, M. Martinkova, and Y.J. Rhee. Compact design of a Nomarski interferometer and its application in the diagnostics of Coulomb explosions of deuterium clusters. *J. Korean Phys. Soc.*, 56:287, 2010.

[127] M. Takeda, H. Ina, and S. Kobayashi. Fourier transform method of fringe pattern analysis for computer based topography and interferometry. *J. Opt. Soc. Am.*, 72:156, 1982.

[128] A. Al-Khateeb, L.A. Doyle, A.H. El-Astal, M.J. Lamb, C.L.S. Lewis, G.W. Martin, T. Morrow, G.J. Pert, D. Riley, I. Weaver, and T.P. Williamson. Numerical modelling of low-temperature laser-produced magnesium plasma. *Appl. Phys. A*, 69:S479, 1999.

[129] M.J. De, C. Henshaw, G.J. Pert, and D.L. Youngs. Non-linear Rayleigh-Taylor Instability in (spherical) laser accelerated targets. *Plas. Phys. Contr. Fus.*, 29:405, 1987.

[130] M. Desselberger, O. Willi, M. Savage, and M.J. Lamb. Measurement of the Rayleigh-Taylor Instability in targets driven by optically smoothed laser beams. *Phys. Rev. Lett.*, 65:2997, 1990.

[131] R.G. Watt, J. Duke, C.J. Fontes, P.L. Gobby, R.V. Hollis, R.A. Kopp, R. J. Mason, D.C. Wilson, C.P. Verdon, T.R. Boehly, J.P. Knauer, D.D. Meyerhofer, V. Smalyuk, R.P.J. Town, A. Iwase, and O. Willi. Laser imprint reduction using a low-density foam buffer as a thermal smoothing layer at 351-nm wavelength. *Phys. Rev. Lett.*, 81:4644, 1998.

[132] R.G. Evans and N.C. Woolsey. Non-uniformities in planar foil expansion. *CLF Annual report*, page 77, 1999/2000.

[133] A.R. Bell, R.G. Evans, and D.J. Nicholas. Electron energy transport in steep temperature gradients in laser produced plasmas. *Phys. Rev. Lett.*, 46:243, 1981.

[134] R.C. Malone, R.L. McCrory, and R.L. Morse. Indications of strongly flux limited electron thermal conduction in laser target experiments. *Phys. Rev. Lett.*, 34:721, 1975.

[135] J.F. Luciani, P. Mora, and J. Virmont. Nonlocal heat transport due to steep temperature gradients. *Phys. Rev. Lett.*, 51:1664, 1983.

[136] Y. Al-Hadithi, G.J. Tallents, J. Zhang, M.H. Key, P.A. Norreys, and R. Kodamal. Energy transport in plasmas produced by a high brightness krypton fluoride laser focused to a line. *Phys. Plasmas*, 1:1279, 1994.

[137] F. Dahmani and T. Kerdja. Laser intensity and wavelength dependence of mass ablation rate, ablation pressure and heat flux inhibition in laser produced plasmas. *Phys. Rev. A*, 44:2649, 1991.

[138] S. N. Chen, G. Gregori, P.K. Patel, H.-K. Chung, R. G. Evans, R. R. Freeman, E. Garcia Saizand S.H. Glenzer, S.B. Hansen, F.Y. Khattak, J.A. King, A.J. Mackinnon, M.M. Notley, J.R. Pasley, D. Riley, R.B. Stephens, R.L. Weber, S.C. Wilks, and F.N. Beg. Creation of hot dense matter in short-pulse laser-plasma interaction with tamped titanium foils. *Phys. Plasmas*, 14:102701, 2007.

[139] M.S. Tillack, K.L. Sequoia, and Y. Tao. Geometric effects on EUV emissions in spherical and planar targets. *Journal of Physics Conference Series*, 112: 042060, 2008.

[140] T. Yabuuchi, B.S. Paradkar, M.S. Wei, J.A. King, F.N. Bef, R.B. Stephens, N. Nakanii, M. Hatakeyama, H. Habara, K. Mima, K.A. Tanaka, and J.T. Larsen. Transport study of intense-laser-produced fast electrons in solid targets with a preplasma created by a long pulse laser. *Phys. Plasmas*, 17: 060704, 2010.

[141] S. Le Pape, A. Macphee, D. Hey, P. Patel, A. Mackinnon, M. Key, J. Pasley, M. Wei, S. Chen, T. Ma, F. Beg, N. Alexander, R. Stephens, D. Offerman, A. Link, L. Van-Woerkom, and R. Freeman. Density measurement of shock compressed foam using two-dimensional x-ray radiography. *Rev. Sci. Instrum.*, 79:106104, 2008.

[142] S.P. Lyon and J.D. Johnson. Los Alamos Report LA-UR-92-3407, Los Alamos National Laboratory, 2001.

[143] A.K. Rossall, L.M.R Gartside, S. Chaurasia, S. Tripathi, D.S. Munda, N.K. Gupta, L.J. Dhareshwar, J. Gaffney, S.J. Rose, and G.J. Tallents. X-ray backlighter characterization for iron opacity measurements using laser-produced aluminium K-alpha emission. *J. Phys. B: At. Mol. Opt. Phys.*, 43: 155403, 2010.

[144] S. Atzeni. The physical basis for numerical fluid simulations in laser fusion. *Plasma Phys. Control. Fus.*, 29:1535, 1987.

[145] Y. Abou-Ali, Q.L. Dong, A. Demir, R.E. King, G.J. Pert, and G.J. Tallents. Quantitative simulations of short pulse x-ray laser experiments. *J. Phys. B: At. Mol. Opt. Phys.*, 37:2855, 2004.

[146] F.N. Beg, A.R. Bell, A.E. Dangor, C.N. Danson, A.P. Fews, M. E. Glinsky, B.A. Hammel, P. Lee, P.A. Norreys, and M. Tatarakis. A study of picosecond laser-solid interactions up to 10^{19} W cm^{-2}. *Plasma Phys.*, 4:447, 1997.

[147] P. Köster, K. Akli, D. Batani, S. Baton, R.G. Evans, A. Giulietti, D. Giulietti, L.A. Gizzi, J.S. Green, M. Koenig, L. Labate, A. Morace, P. Norreys, F. Perez, J. Waugh, N. Woolsey, and K.L. Lancaster. Experimental investigation of fast electron transport through K_α imaging and spectroscopy in relativistic laser-solid interactions. *Plasma Phys. Control. Fusion*, 51:014007, 2009.

[148] S.J. Davidson, K. Nazir, S.J. Rose, R. Smith, and G.J. Tallents. Short-pulse laser opacity measurements. *JQSRT*, 65:151, 2000.

[149] G.J. Pert. The hybrid model and its applications for studying free expansion. *J. Fluid Mech.*, 131:401, 1983.

[150] Work carried out by I.R. Al'miev. postdoctoral researcher, University of York, 2009.

[151] J. Filevich, J.J. Rocca, M.C. Marconi, S.J. Moon, J. Nilsen, J.H. Scofield, J. Dunn, R.F. Smith, R. Keenan, J.R. Hunter, and V.N. Shlyaptsev. Observation of a multiply ionized plasma with index of refraction greater than one. *Phys. Rev. Lett.*, 94:035005, 2005.

[152] B. Rus, T. Mocek, A.R. Präg, M. Kozlová, G. Jamelot, A. Carillon, D. Ros, D. Joyeux, and D. Phalippou. Multimillijoule, highly coherent x-ray laser at 21 nm operating in deep saturation through double-pass amplification. *Phys. Rev. A*, 66:063806, 2002.

[153] A.R. Präg, T. Mocek, M. Kozlová, B. Rus, G. Jamelot, and D. Ros. Study of the stability of beam characteristics of the neon-like Zn x-ray laser using a half cavity. *Eur. Phys. J. D*, 22:31, 2003.

[154] J. Nejdl, T. Mocek, B. Rus, S. Sebban, and B. Wellegehausen. Innershell x-ray laser in sodium vapor: final steps towards experimental verfication. *Springer Proc. Phys.*, 130:557, 2008.

[155] M. Kozlová, B. Rus, T. Mocek, J. Polan, P. Homer, D. Snopek, K. Jakubczak, M. Fajardo, and A. Barszczak Sardinha. High resolution x-ray laser backlighting of plasmas. *Springer Proc. Phys.*, 130:417, 2008.

[156] G.J. Tallents, M.H. Key, P. Norreys, J. Jacoby, R. Kodama, H. Baldis, J. Dunn, and D. Brown. Energy transport in plasmas produced by a high brightness KrF Raman laser. *Opt. Commun.*, 89:410, 1992.

[157] B.H. Ripin, R. Decoste, S.P. Obenschain, S.E. Bodner, E.A. McLean, F.C. Young, R.R. Whitlock, C.M. Armstrong, J. Grun, J.A. Stamper, S.H. Gold, D.J. Nagel, R.H. Lehmberg, and J.M. McMahon. Laser plasma interaction and ablative acceleration of thin foils at $10^{12} - 10^{15}$ W cm^{-2}. *Phys. Fluids*, 23:1012, 1980.

[158] A. Ng, D. Pasini, P. Celliers, D. Parfeniuk, L. Da Silva, and J. Kwan. Ablation scaling in steady state ablation dominated by inverse bremsstrahlung absorption. *Appl. Phys. Lett.*, 45:1046, 1984.

[159] J. Filevich, J. Grava, M. Purvis, M.C. Marconi, J.J. Rocca, J. Nilson, J. Dunn, and W.R. Johnson. Prediction and observation of tin and silver plasmas with index of refraction greater than one in the soft x-ray range. *Phys. Rev. E.*, 74:016404, 2006.

[160] J. Nilsen, W.R. Johnson, C.A. Iglesias, and J.H. Scofield. Impact of anomalous dispersion on the interferometer measurements of plasmas. *JQSRT*, 99: 425, 2006.

[161] J. Archer, R.E.H. Clark, C.J. Fontes, and H. Zhang. Gipper user manual. Los Alamos Report LA-UR-00-5693, Los Alamos National Laboratory, 2000.

[162] A.Y. Potekin, G. Massacrier, and G. Chabrier. Equation of state for partially ionized carbon at high temperatures. *Phys. Rev. E*, 72:046402, 2005.

[163] Y. Morita, H. Nishimura, Y. Ochi, K. Fujita, M. Fukao, M. Suzuki, T. Kawamura, H. Daido, and H. Takabe. Model calculations and experiments on photoionized plasmas in relevant to laboratory astrophysics. *JQSRT*, 71: 519, 2001.

[164] H.-K Chung and R.W. Lee. Applications of NLTE population kinetics. *HEDP*, 5:1, 2009.

[165] J. Nilsen and J.H. Scofield. Wavelength of neon-like 3p $\rightarrow$ 3s x-ray laser transitions. *Phys. Scr.*, 49:588, 1994.